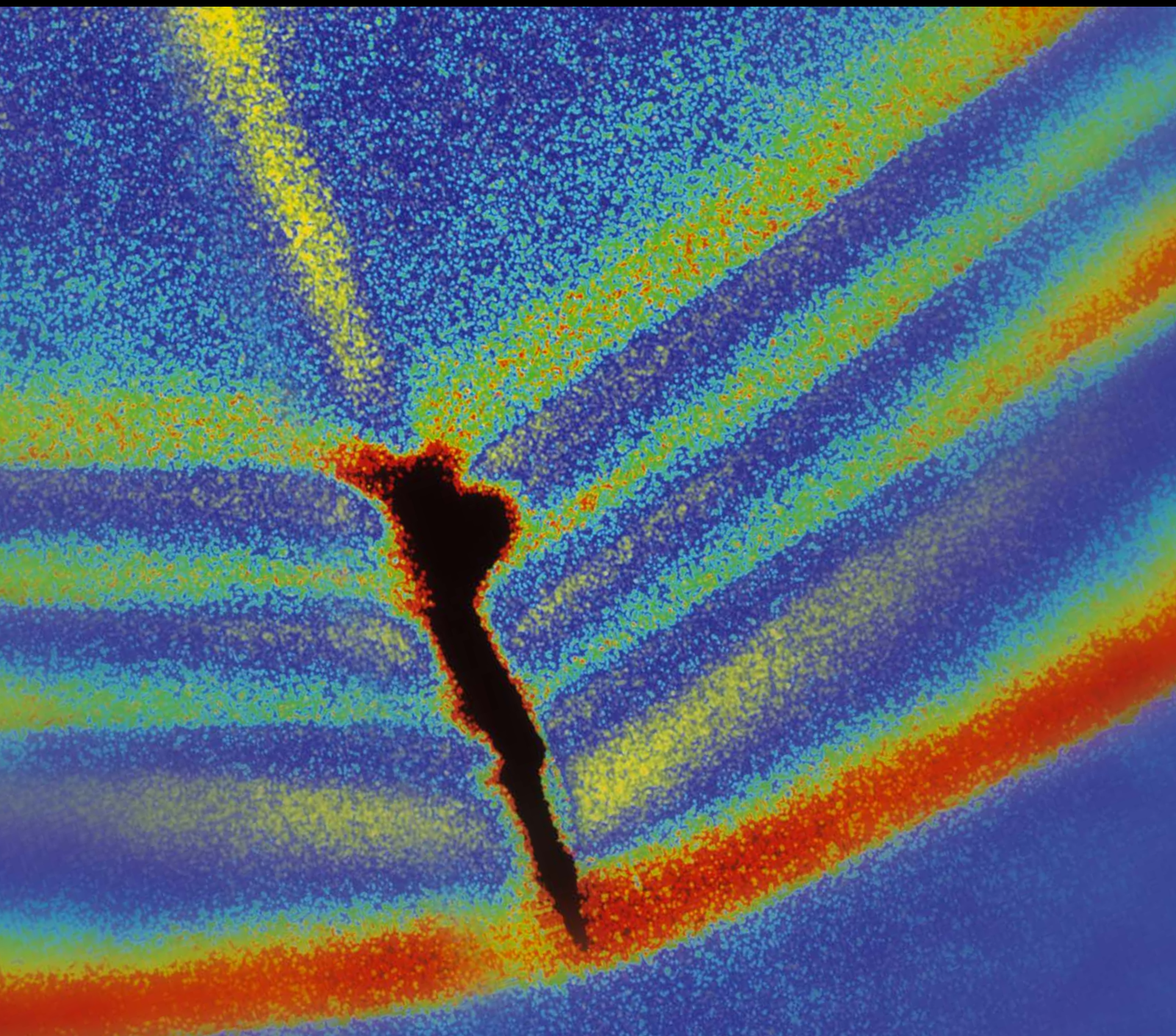


Shock and Vibration

# Waveform-Based Condition Assessments in Civil Engineering

Guest Editors: Sang-Youl Lee, Guillermo Rus, and Abdollah Shafieezadeh





---

# **Waveform-Based Condition Assessments in Civil Engineering**

Shock and Vibration

---

## **Waveform-Based Condition Assessments in Civil Engineering**

Guest Editors: Sang-Youl Lee, Guillermo Rus,  
and Abdollah Shafieezadeh



---

Copyright © 2016 Hindawi Publishing Corporation. All rights reserved.

This is a special issue published in "Shock and Vibration." All articles are open access articles distributed under the Creative Commons Attribution License, which permits unrestricted use, distribution, and reproduction in any medium, provided the original work is properly cited.

## Editor-in-Chief

Mehdi Ahmadian, Virginia Polytechnic Institute and State University, USA

## Editorial Board

Brij N. Agrawal, USA  
Marco Alfano, Italy  
Farbod Alijani, Canada  
Sumeet S. Aphale, UK  
Mariano Artés, Spain  
Hassan Askari, Canada  
Matteo Aureli, USA  
Ranjan Banerjee, UK  
Mahmoud Bayat, Iran  
José A. Becerra Villanueva, Spain  
Marco Belloli, Italy  
Subhamoy Bhattacharya, UK  
Ivo Caliò, Italy  
Antonio Carcaterra, Italy  
Dumitru I. Caruntu, USA  
Noel Challamel, France  
Athanasios Chasalevris, UK  
Ashwin Chinnayya, France  
Giorgio Dalpiaz, Italy  
Farhang Daneshmand, Canada  
Sergio De Rosa, Italy  
Dario Di Maio, UK  
Longjun Dong, China  
Lorenzo Dozio, Italy  
Mohamed El Badaoui, France  
Mohammad Elahinia, USA  
Fiorenzo A. Fazzolari, UK  
Francesco Franco, Italy

Pedro Galvín, Spain  
Alessandro Gasparetto, Italy  
Gianluca Gatti, Italy  
Anindya Ghoshal, USA  
Nere Gil-Negrete, Spain  
Hassan Haddadpour, Iran  
M.I. Herreros, Spain  
Hamid Hosseini, Japan  
Reza Jazar, Australia  
Sakdirat Kaewunruen, UK  
Yuri S. Karinski, Israel  
Jeong-Hoi Koo, USA  
Georges Kouroussis, Belgium  
Mickaël Lallart, France  
Kenneth J. Loh, USA  
Nuno M. Maia, Portugal  
Giuseppe C. Marano, Italy  
Laurent Mevel, France  
Emiliano Mucchi, Italy  
Tony Murmu, UK  
Sundararajan Natarajan, India  
Toshiaki Natsuki, Japan  
Miguel Neves, Portugal  
Coral Ortiz, Spain  
Aleksandar Pavic, UK  
Evgeny Petrov, UK  
Antonina Pirrotta, Italy  
Vitomir Racic, Italy

Carlo Rainieri, Italy  
Didier Rémond, France  
Francesco Ripamonti, Italy  
Salvatore Russo, Italy  
Edoardo Sabbioni, Italy  
Jerzy T. Sawicki, USA  
Onome E. Scott-Emuakpor, USA  
Vadim V. Silberschmidt, UK  
Kumar V. Singh, USA  
Isabelle Sochet, France  
Alba Sofi, Italy  
Jussi Sopanen, Finland  
Stefano Sorace, Italy  
Narakorn Srinil, UK  
Salvatore Strano, Italy  
Chao Tao, China  
Mario Terzo, Italy  
Tai Thai, Australia  
Carlo Trigona, Italy  
Federica Tubino, Italy  
Nerio Tullini, Italy  
Marcello Vanali, Italy  
Jörg Wallaschek, Germany  
Zaili L. Yang, UK  
Stana Živanović, UK  
Lei Zuo, USA

# Contents

---

**Waveform-Based Condition Assessments in Civil Engineering**

Sang-Youl Lee, Guillermo Rus, and Abdollah Shafieezadeh

Volume 2016, Article ID 3789358, 1 page

**An Influence of Gas Explosions on Dynamic Responses of a Single Degree of Freedom Model**

Ki-Yeob Kang, Kwang-Ho Choi, Jae Woong Choi, Yong Hee Ryu, and Jae-Myung Lee

Volume 2016, Article ID 9582702, 13 pages

**Crash-Induced Vibration and Safety Assessment of Breakaway-Type Post Structures Made of High Anticorrosion Steels**

Sang-Youl Lee

Volume 2016, Article ID 5010521, 11 pages

**Damage Detection of Structures for Ambient Loading Based on Cross Correlation Function Amplitude and SVM**

Lin-sheng Huo, Xu Li, Yeong-Bin Yang, and Hong-Nan Li

Volume 2016, Article ID 3989743, 12 pages

**An Experimental Study of Structural Identification of Bridges Using the Kinetic Energy Optimization Technique and the Direct Matrix Updating Method**

Gwanghee Heo and Joonryong Jeon

Volume 2016, Article ID 3287976, 13 pages

**Vibration Effects of Nonclassically Damped Building-Piping Systems Subjected to Extreme Loads**

YongHee Ryu, WooYoung Jung, and BuSeog Ju

Volume 2016, Article ID 6189326, 9 pages

**Structural Performance Assessment Based on Statistical and Wavelet Analysis of Acceleration Measurements of a Building during an Earthquake**

Mosbeh R. Kaloop, Jong Wan Hu, Mohamed A. Sayed, and Jiyounng Seong

Volume 2016, Article ID 8902727, 13 pages

## Editorial

# Waveform-Based Condition Assessments in Civil Engineering

**Sang-Youl Lee,<sup>1</sup> Guillermo Rus,<sup>2</sup> and Abdollah Shafieezadeh<sup>3</sup>**

<sup>1</sup>*Department of Civil Engineering, Andong National University, Andong-si, Gyeongsangbuk-do 760-749, Republic of Korea*

<sup>2</sup>*Department of Structural Mechanics, University of Granada, Politecnico of Fuentenueva, 18071 Granada, Spain*

<sup>3</sup>*Department of Civil, Environmental and Geodetic Engineering, Ohio State University, Columbus, OH 43210, USA*

Correspondence should be addressed to Sang-Youl Lee; [lsy@anu.ac.kr](mailto:lsy@anu.ac.kr)

Received 4 April 2016; Accepted 5 April 2016

Copyright © 2016 Sang-Youl Lee et al. This is an open access article distributed under the Creative Commons Attribution License, which permits unrestricted use, distribution, and reproduction in any medium, provided the original work is properly cited.

Deterioration of infrastructures under dynamic effects becomes a critical issue in regard to both safety and economic concerns. Deterioration itself is inevitable, but condition assessment technology and nondestructive evaluation techniques could provide solutions to ensure public safety by means of detecting damage before serious and expensive degradation consequences occur. The novelty of this issue is the use of dynamic effects and its response due to the anomalies in a structure under testing.

Waveform-based condition assessments for various structures are studied by a host of investigators using a variety of approaches. M. R. Kaloop et al. deal with structural performance assessment based on statistical and wavelet analysis of acceleration measurements of a building during an earthquake. Y. Ryu et al. present results of vibrations of classical and nonclassical damping for coupled primary-secondary systems including material nonlinearity. They use finite-element building-piping models derived from the open system for earthquake engineering simulation and carry out the Rayleigh equation to develop classical and nonclassical damping matrices for a 2-DOF coupled primary-secondary system. G. Heo and J. Jeon develop an SI (structural identification) technique using the KEOT (Kinetic Energy Optimization Technique) and the DMUM (Direct Matrix Updating Method) to decide on optimal location of sensors and to update FE model, respectively, which ultimately contributes to a composition of more effective SHM (Structural Health Monitoring).

Besides those, there are several interesting topics in the issue. L. Huo et al. propose an effective method for the damage detection of skeletal structures which combines

the cross correlation function amplitude (CCFA) with the support vector machine (SVM). S.-Y. Lee deals with car crash effects and passenger safety assessment of post structures with breakaway types using high performance steel materials. In order to disperse the impact force when a car crashes into a post, the post could be designed with a breakaway feature. In his study, new high anticorrosion steel is used for the development of advanced breakaways. K.-Y. Kang et al. present qualitative analyses of the dynamic response of structures subjected to various types of gas explosion loads.

By compiling these papers, we hope to enrich our readers and researchers with respect to various waveform-based condition assessments in civil engineering.

*Sang-Youl Lee  
Guillermo Rus  
Abdollah Shafieezadeh*

## Research Article

# An Influence of Gas Explosions on Dynamic Responses of a Single Degree of Freedom Model

Ki-Yeob Kang,<sup>1</sup> Kwang-Ho Choi,<sup>1</sup> Jae Woong Choi,<sup>2</sup> Yong Hee Ryu,<sup>2</sup> and Jae-Myung Lee<sup>1</sup>

<sup>1</sup>*Department of Naval Architecture and Ocean Engineering, Pusan National University, Jangjeon-Dong, Geumjeong-Gu, Busan 609-735, Republic of Korea*

<sup>2</sup>*Central Research Institute, Samsung Heavy Industries Co., Ltd., Seongnam 13486, Republic of Korea*

Correspondence should be addressed to Yong Hee Ryu; [yh32.ryu@samsung.com](mailto:yh32.ryu@samsung.com) and Jae-Myung Lee; [jaemlee@pusan.ac.kr](mailto:jaemlee@pusan.ac.kr)

Received 26 November 2015; Revised 11 February 2016; Accepted 11 February 2016

Academic Editor: Guillermo Rus

Copyright © 2016 Ki-Yeob Kang et al. This is an open access article distributed under the Creative Commons Attribution License, which permits unrestricted use, distribution, and reproduction in any medium, provided the original work is properly cited.

Explosion risk analysis (ERA) is widely used to derive the dimensioning of accidental loads for design purposes. Computational fluid dynamics (CFD) simulations contribute a key part of an ERA and predict possible blast consequences in a hazardous area. Explosion pressures can vary based on the model geometry, the explosion intensity, and explosion scenarios. Dynamic responses of structures under these explosion loads are dependent on a blast wave profile with respect to the magnitude of pressure, duration, and impulse in both positive and negative phases. Understanding the relationship between explosion load profiles and dynamic responses of the target area is important to mitigate the risk of explosion and perform structural design optimization. In the present study, the results of more than 3,000 CFD simulations were considered, and 1.6 million output files were analyzed using a visual basic for applications (VBA) tool developed to characterize representative loading shapes. Dynamic response of a structure was investigated in both time and frequency domains using the Fast Fourier Transform (FFT) algorithm. In addition, the effects of the residual wave and loading velocity were studied in this paper.

## 1. Introduction

An explosion is an extremely rapid release of energy, accompanied by high temperatures and an increased number of moles in the combustion products. The process initiates a fast volume expansion which in most cases results in pressure rise and high flow speeds. Objects in the vicinity of the ignition point are likely exposed to substantial pressure forces depending on their characteristics. As the process proceeds, pressure will propagate into the surroundings as blast wave, which is a layer of compressed air, propagating away from the original ignition point [1]. This blast wave is the main reason for structural damage in explosion accidents [2–4]. Thus, it is very important to predict the load profile by blast wave in order to prevent the explosion damage. However, a correct prediction for blast wave profiles is very difficult, and it is impossible to obtain an accurate pressure data set directly from explosion accidents. Explosion pressures from real accidents are not available because data measurement during the accident is not possible at all. The most practical way

to evaluate the explosion pressure is numerical calculation using methods such as computational fluid dynamics (CFD) analysis. Generally, blast wave profiles by CFD analysis are utilized for structural analysis and applied as a loading condition in a computational analysis such as finite element method. The shape of a blast wave profile depends on the characteristics of the structural model in the simulation of an explosion. Thus, the modeling technique for a target structure is very important in order to obtain accurate data [5]. These data can be used for investigation of the dynamic response of structures to blast loading. In structural analysis, single degree of freedom models (SDOF) can be used for many types of structures such as walls, slabs, tubes, and columns [6–8]. These models are evaluated using only one degree of freedom, so they can be inaccurate in terms of quantitative analysis of complex structural response. However, this may be useful tool in qualitative analysis that considers different blast load profiles. Hence, many researchers have carried out the blast analysis using the SDOF model for description of characteristics for structural response subjected to blast load profiles

TABLE 1: The scenarios for vapour cloud explosion.

Module positions	Grid	Ignition positions at elevation view	Cloud position within a module	Cloud size	Ignition position
(1) A	(1) 0.5 m	(1) Bottom	(1) Center	(1) 199 m <sup>3</sup>	(1) Center
(2) B	(2) 1.0 m	(2) Top	(2) Left	(2) 465 m <sup>3</sup>	(2) Same as cloud position
(3) C			(3) Right	(3) 899 m <sup>3</sup>	(3) Left
(4) D			(4) Bottom	(4) 1556 m <sup>3</sup>	(4) Right
(5) E			(5) Top	(5) 2479 m <sup>3</sup>	(5) Bottom
(6) F				(6) 3727 m <sup>3</sup>	(6) Top

[9–11]. Although there is a large amount of literature available on the characteristics of structural response to dynamic loads, the effect of a blast load profile on the response characteristics of an SDOF model has not been extensively studied. In terms of blast wave profiles, it can occur variously according to the magnitude of pressure, loading duration, loading rate at each domain, and so on. To reflect the diversity of blast load profiles, simplified linear load models are used. It is a triangular shape which is defined by the maximum pressure in each pressure phase and impulse of each phase. The explosion waves were generated by the simulation method using the FLACS, a flame acceleration simulator, and consideration with counting possible cases for each of the factors related to explosion response. In addition, monitoring tool was developed using VBA code in order to analyze the characteristics for explosion load history. The explosion load profiles were divided into two categories and positive pressure phase, negative pressure phase, respectively. The structural response analysis was performed with respect to both time and frequency domains reflecting the variation of load profiles.

## 2. Gas Explosion Analysis

**2.1. Blast Overpressure.** When a large scale explosion occurs, blast overpressure is a major hazard in offshore plants as well as other structures associated with combustible gas and flammable materials. Thus, it is essential design process to withstand the blast overpressure in a FPSO topside module. This pressure profile over time of gas explosion can be determined by the motion of blast wave, and it is divided into the phase of expansion and suction [12]. In expansion phase, the atmospheric pressure increases dramatically to a peak value, but it does not always increase linearly; it is often fluctuated. However, this effect may be ignored because fluctuation is dissipated quickly, so only the initial expansion or suction is important [13]. In this study, a range of explosion simulation was carried out in order to investigate for characteristics about blast overpressure at each condition.

**2.2. Simulation for Explosion of Vapour Cloud.** Dispersion and ventilation analyses are very important to control the risk of gas explosions in offshore installations. First, in case of ventilation, wind speed was estimated based on a linear correlation assumption between external wind speed and internal flow. By using the results of ventilation analysis, dispersion analysis was carried out in order to determine the spread of

released gas under various conditions based on a defined number of wind directions, speeds, ventilation, observations about equipment, and the geometry in the areas. The leak representation was also based on a preventative range of possible combinations of leak parameters and includes variations in directions relative to the wind directions, leaks impinging on objects, free field jets, and diffusive leaks. The leak locations were chosen to be close to specific equipment or in an area with several leak sources. Eight different leak rates such as 0.75 kg/s, 1.5 kg/s, 3.0 kg/s, 6 kg/s, 12 kg/s, 24 kg/s, 48 kg/s, and 96 kg/s are simulated for each leak location. Six release directions such as +/- X, +/- Y, and +/- Z and diffusive release condition are considered for specific leak locations. The vapour cloud explosion simulations were carried out considering the results from the ventilation and dispersion analysis. The purpose of the explosion analysis is to identify potential explosion loads in the areas of concern. A number of explosion simulations were carried by the FLACS software, which is one of the best validated tools for modeling flammable and toxic releases in the technical safety context in the oil and gas field [14, 15]. These simulations were considered to various gas cloud sizes, gas cloud locations, and ignition locations described in Table 1. The gas clouds were of homogeneous stoichiometric concentration, and two different types of monitors were used to record blast load profiles as shown in Figure 1. 1000-point monitors were uniformly distributed over the entire process area at a space of 3 meters, while  $3 \times 3$  (m<sup>2</sup>), local panel monitors were distributed on blast walls and decks.

**2.3. FLACS Model: FPSO Topside Platform.** A series of CFD analysis was performed using a full-scale FPSO topside model including detailed parts of pipes and equipments, and the time history data of the blast loads at monitor points and panels were obtained by the analyses. In CFD analyses, all fire and blast walls were assumed to be rigid and unyielding during the explosions; namely, the walls did not deform under the design explosion loads. The blast pressure might be somewhat overestimated because the blast wave could travel over the deformed structures with angle. Plated decks are assumed to be solid and unyielding, while grated decks are assumed to be 50% open and remain in place during the explosion. Figure 1 shows the geometrical floating production, storage, and offloading (FPSO) model used in this study for vapour cloud explosion simulation. The FPSO can be divided into two main areas under the influence of explosion. One is turret

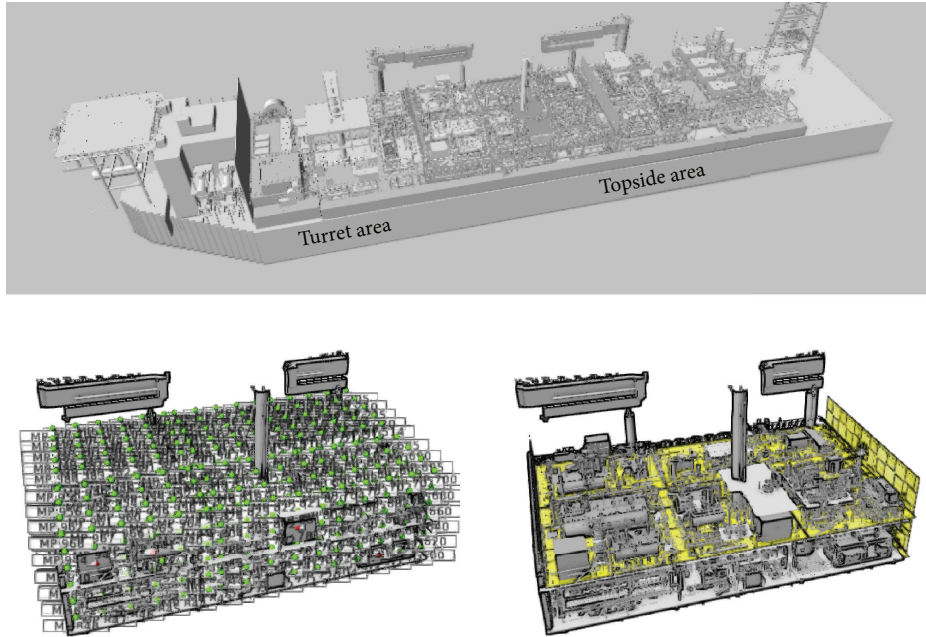


FIGURE 1: Separation of module and monitoring position.

area and the other is topside area. The turret is moored to the seabed with chains, wires, and anchors. In addition, it allows the FPSO to adopt the direction of the least resistance against wave, wind, and currents [16]. The topside area consists of a process system and a utility system. The process system has a variety of combustible substance and flammable materials so that the probability of explosion is much higher than utility system [17]. These main characteristics of FPSO were reflected in this model. Since the modeling details are the most critical factor affecting the overpressure response, the 3D models approved for construction were considered in this study including minor obstacles such as small piping, stairs, handrails, and instruments as well as all the equipment and structures on the topside of the FPSO for CFD simulations.

### 3. FLACS Output Data Analysis

**3.1. Development of Data Process Tool.** In present study, to measure the explosion pressure data, 1000-point monitors are uniformly distributed over the entire process area at a space of 3 meters from the process deck and blast walls. In addition, 206-panel monitors are distributed equally on blast walls and decks. Hence, many different kinds of explosion wave profiles were acquired, and then computational tool using VBA code was developed to monitor these enormous output data. Figure 2 shows the procedure for gas explosion data analysis using developed VBA code. First of all, CFD analysis performs considering the explosion simulation affecting parameters such as ignition position, cloud size and position, and data types. The next stage is to sort and process the FLACS output data considering the desired information of explosion load profiles. Generally, explosion design load is determined by two values in the peak pressure and each impulse which is the area under a transient wave profiles.

Thus, the VBA code provides the core functions which can bring the information values of output data, and it is able to compare these values according to scenarios and data types. The explosion load profiles were simplified to triangle shape which was generated by using the equivalent peak pressure and impulse. This is because of the time effective method in structural analysis. The developed VBA code can plot this simplified model considering each pressure wave parameter.

**3.2. Quantitative Analysis.** The intensity of overpressure is a core factor in the evaluation of an explosion wave profile. Overpressure in the process area (as shown in Figure 3) was measured through gas explosion simulations by using the CFD software, and all output data were analyzed using the developed VBA code. Figure 4 shows the maximum overpressures measured in the process area based on the gas cloud volumes of  $199 \text{ m}^3$ ,  $465 \text{ m}^3$ ,  $899 \text{ m}^3$ ,  $1556 \text{ m}^3$ ,  $2479 \text{ m}^3$ ,  $3727 \text{ m}^3$ , and  $5314 \text{ m}^3$ . To easily compare the intensity of overpressure, the average overpressures with respect to each gas cloud volume were normalized by the maximum overpressure, which is observed at a gas cloud volume of  $3,727 \text{ m}^3$  at the process-turret wall. Figure 4(a) shows the maximum overpressure at the two blast walls between the utility-process area and the process-turret area, and Figure 4(b) shows the difference of overpressure intensity of modules in the process area. Both figures indicate that the gas cloud volume size directly influences the intensity of overpressure, and overpressure toward the turret area is higher than that on the other side. This is because congestion in modules M410 and M430 is much higher than that of other modules (see Figure 3), indicating that fluid interaction on small- and medium-sized objects increases the intensity of explosion pressures. This relationship between the level of congestion

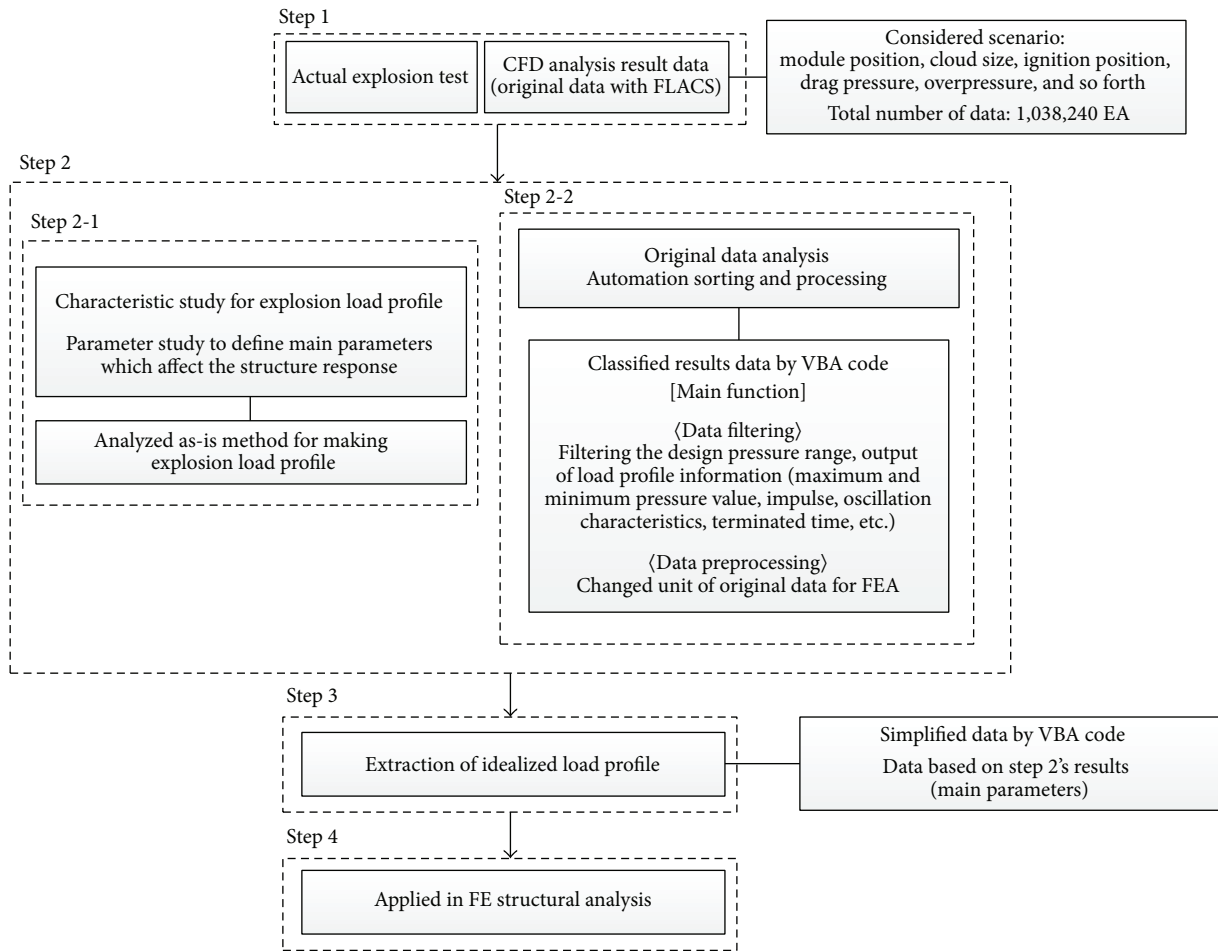


FIGURE 2: Algorithm for gas explosion data analysis using developed VBA code.

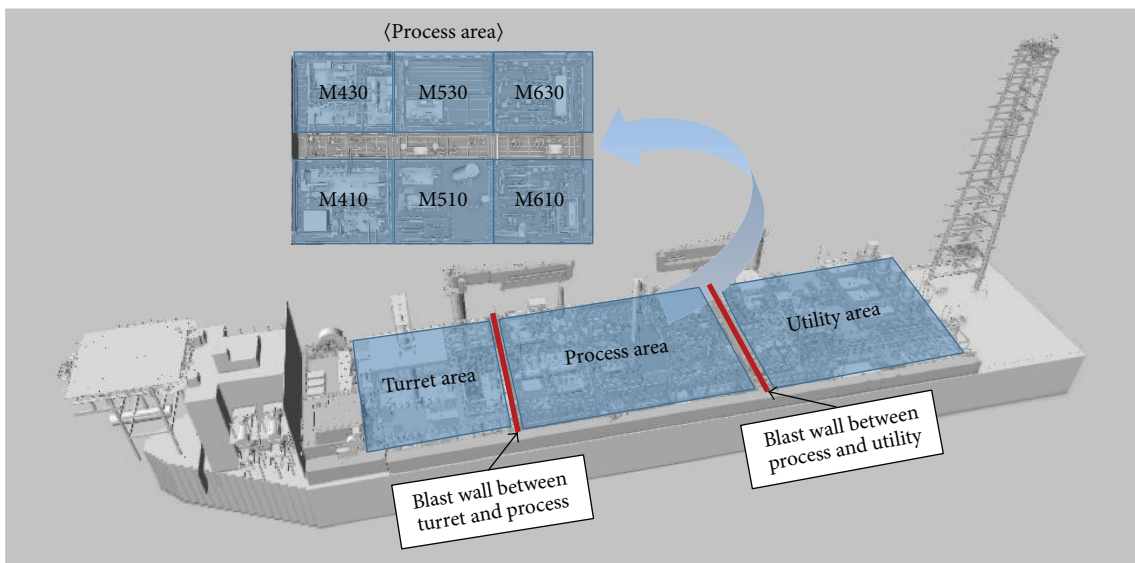


FIGURE 3: Layout of FPSO.

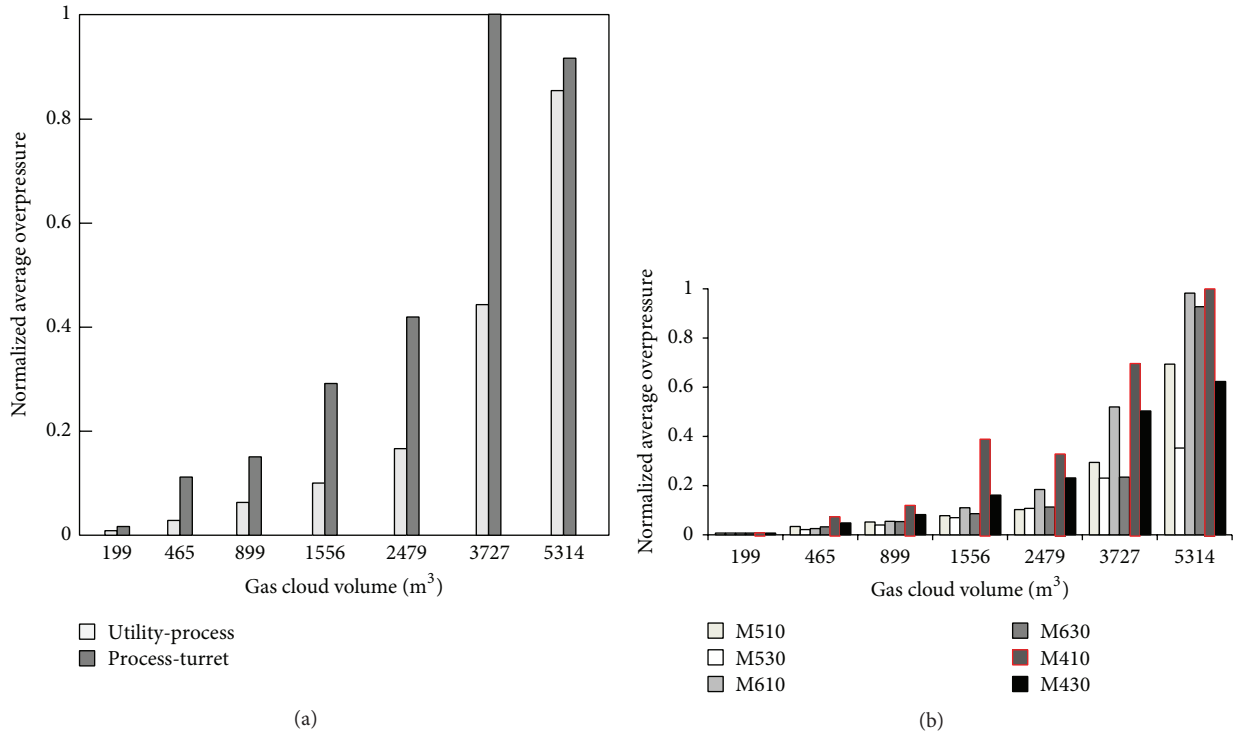


FIGURE 4: The difference of maximum overpressures according to the gas cloud volume in specific positions. (a) Comparison between utility-process and process-turret area. (b) Comparison at the modules.

and the intensity of overpressure was studied by Chille et al. [18]. They reported that the peak overpressure under a complex geometry condition was significantly higher than that under a simple geometry condition. Thus, to reduce structural damage due to blast pressure loads, it is important to retain sufficient space for the transportation of an explosion wave.

**3.3. The Relationship between Positive Pressure and Negative Pressure.** It is a controversial issue to include the negative phase in the pressure-time history in the blast analysis of structures. The negative pressure was often neglected by assuming that it may be insignificant to the dynamic response of structures in blast analysis and design [19, 20]. However, the negative pressure sometimes is quite significant and cannot be neglected. In addition, the interaction between the negative part of the blast wave and the response of the structure response is important. In this study, the relationship between the positive and negative peak pressures in an explosion load profile was investigated by analyzing explosion simulation results. The relationship between the positive and negative pressures in all explosion scenarios is illustrated for different data types in Figure 5. The quantitative distributions of the positive and negative pressures based on the normalized values are plotted in black and red dots, respectively. Although the negative pressure is lower than the positive pressure for most data, the magnitude of negative pressure is similar to that of the positive pressure in some cases. For the point-pressure (NP) data, the magnitude of the negative pressure is similar to that of the positive pressure for a relatively

small pressure range as shown in Figure 6(a). Figure 6(b) also shows the results of panel-pressure (NPP) data, and the value of negative pressure is higher compared to that in the point-pressure (NP) data. The formation of the negative phase in a pressure wave highly depends on the geometry condition. For example, the tunnel scenarios represent an extreme case to form the negative pressure. If the gas cloud is ignited in a tunnel with a closed end, there will be overpressure first. Once the pressure propagates to the opening, a high negative pressure will propagate back in. The offshore topside has a high level of congestion and confinement to build the negative pressure at some locations. A positive peak pressure of 0.02–0.07 MPa is normally considered as design explosion loads in offshore industries [21]. It should be noted that the negative phase in a pressure-time history model should be included for accurate blast analysis and structural assessment if the intensity of the negative pressure is considerably high (when defining the design blast pressure).

**3.4. Fast Fourier Transform Analysis.** To investigate the effect of pressure intensity at each phase, a Fast Fourier Transform (FFT) analysis was performed using the MATLAB software. The applied load was converted from the time domain to the frequency domain in order to perform a spectrum analysis by using the FFT method. A Fourier analysis is one of the useful solutions to determine a representative frequency domain from an arbitrary signal and provides information to understand the characteristics of the signal [22]. This method can analyze the frequency characteristics of a system by measuring the transformed response of the system based on

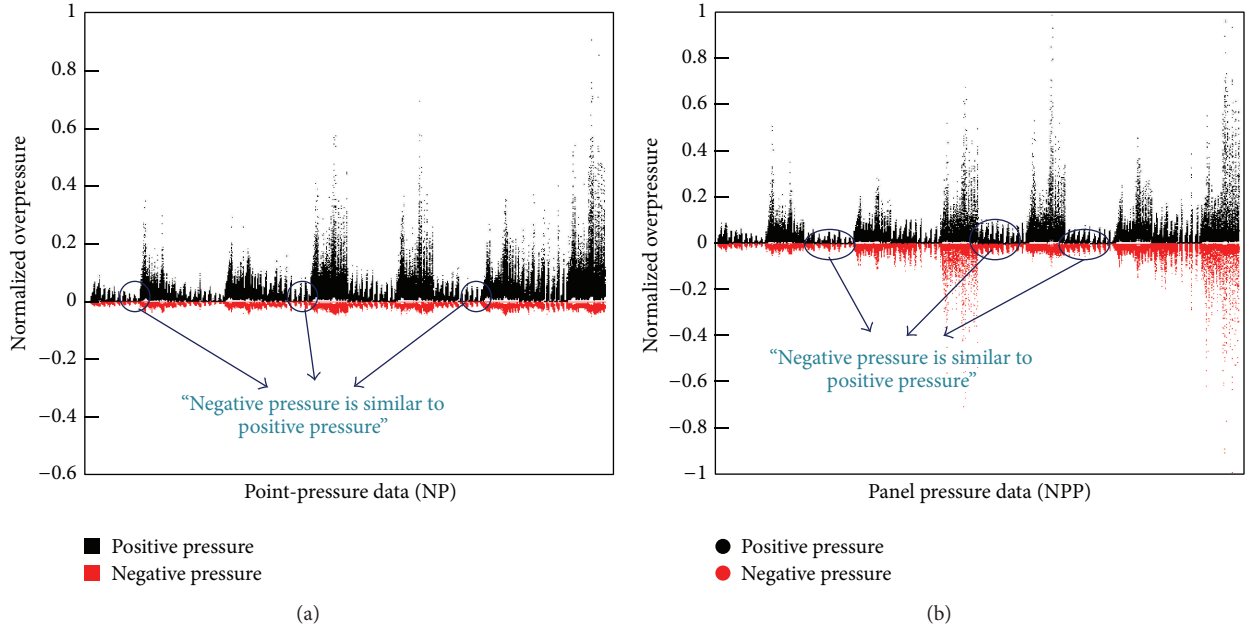


FIGURE 5: The comparison between positive and negative overpressure according to data types: (a) point pressure data type and (b) panel pressure data type.

the specific input function. The FFT analysis was performed to investigate the dynamic response of the SDOF model in the frequency domain, considering the variation of the positive and negative peaks in this study. The top graphs in Figures 6 and 7 indicate the input load profiles in the time domain, and the bottom graphs show their FFT results, the input load in the frequency domain, and the maximum displacements of the SDOF models regarding each frequency level. To clearly compare the magnitude of the maximum load in the same phase, the absolute values of the negative and positive loads were plotted, as shown by the black lines in each figure. Figures 6 and 7 present the FFT results for controlling the positive and negative maximum loads, respectively. The maximum displacement obtained by performing dynamic analyses, using the SDOF models, shows that not only the magnitude of the positive phase but also the magnitude of the negative phase affects the dynamic response of the system when the impulse of the negative phase is relatively large. It should be noted that the dominant area in the frequency domain (i.e.,  $\sim 6$  Hz) was observed at the end of the input load.

## 4. Dynamic Response Analysis

**4.1. SDOF Model.** The characteristics of the structural response subjected to blast load have been analyzed using a SDOF model that can be described by a single mass connected to a spring. This mass can only move along the spring elongation direction. Generally, SDOF models are often used to approximately understand the dynamic response mechanism for a complex structural system [23]. When the motion of SDOF models is related to explosion acceleration,  $\ddot{x}(t)$  is considered.

The equation for this motion can be described as follows:

$$m\ddot{x}(t) + c\dot{x}(t) + kx(t) = F[x(t)]. \quad (1)$$

Substitute  $w_n = \sqrt{k/m}$  and  $\zeta = c/2mw_n = c/c_{cr}$ .

Equation (1) can be rewritten as

$$\ddot{x}(t) + 2\zeta w_n \dot{x}(t) + w_n^2 x(t) = \frac{F[x(t)]}{m}, \quad (2)$$

$$c_{cr} = 2mw_n = 2\sqrt{km} = \frac{2k}{w_n}, \quad (3)$$

$$T_D = \frac{T_n}{\sqrt{1-\zeta^2}}, \quad (4)$$

where  $x(t)$  is the displacement of SDOF model and  $\dot{x}(t)$  and  $\ddot{x}(t)$  mean the mass velocity and mass acceleration by explosion loading. In addition,  $w_n$  is the natural frequency of the SDOF model and  $\zeta$  is the ratio of the damping of the model to the critical value ( $c_{cr}$ ). The damping constant  $c$  is a measure of the energy dissipated in one cycle of free vibration. Equation (4) shows the relationship between the natural period of the damped vibration and the natural period without damping. From this equation, it is inferred that the natural period ( $T_n$ ) and the natural period of damped vibration ( $T_D$ ) are almost the same if the damping ratio is small. It should be noted that the damping effect can be very small when studying the critical response of structures under the drastic increase/decrease of load in sudden time such as gas explosion load [13]. Hence, the characteristics of dynamic response by explosion loads were analyzed using the undamped single degree of freedom model in this study.

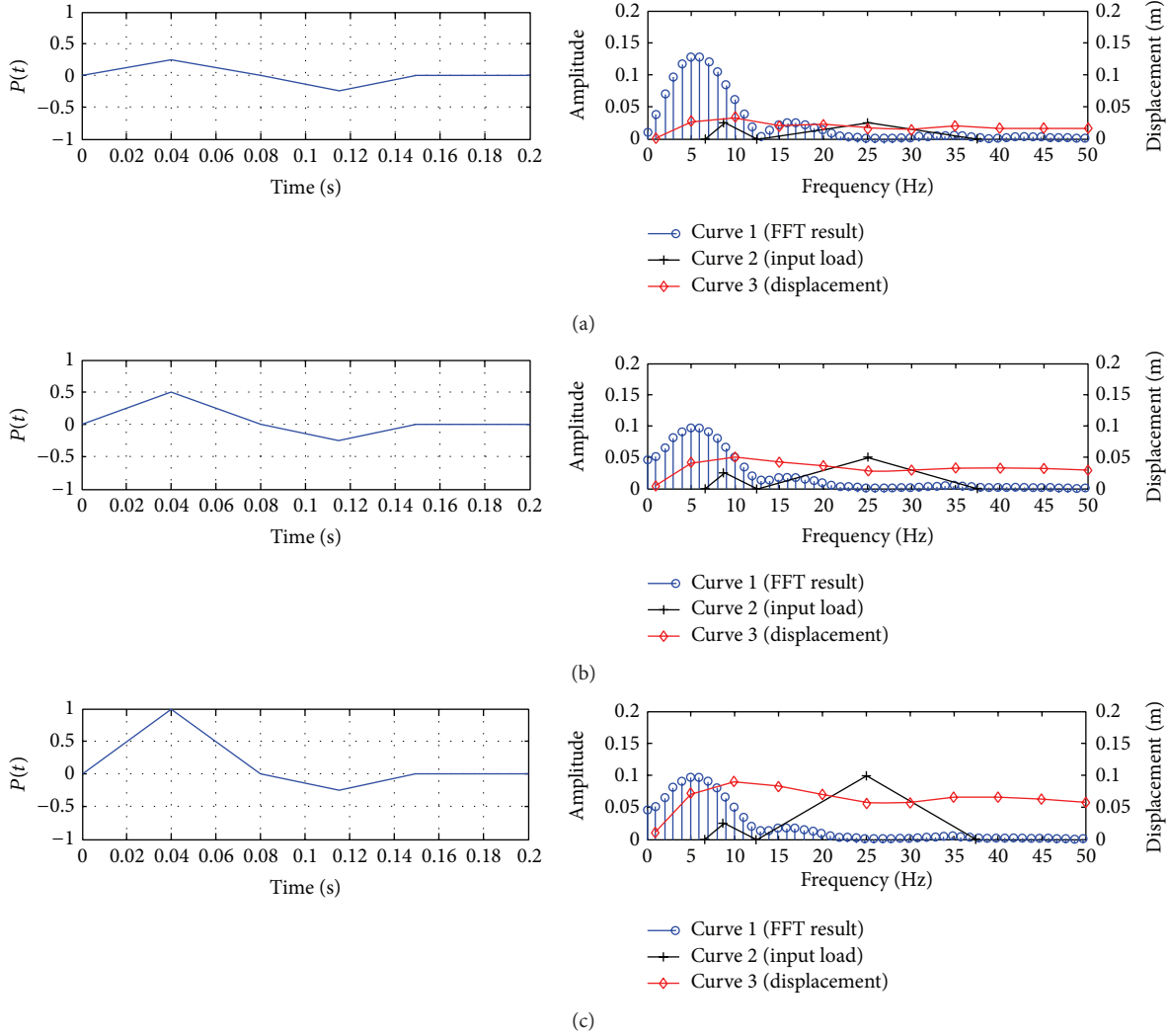


FIGURE 6: Fast Fourier Transform analysis considering the magnitude of maximum load in positive pressure phase. (a) Standard data. (b) Increasing the 2 times of positive maximum load. (c) Increasing the 4 times of positive maximum load.

TABLE 2: Detailed properties of SDOF.

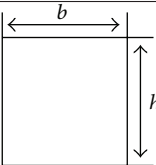
Cross section	Breadth (m)	Height (m)	Length (m)	Geometrical moment of inertia ( $m^4$ )	Elastic Modulus (MPa)	Density ( $kg/m^3$ )
	0.1	0.1	1	$8.33 \cdot 10^{-6}$	$2.07 \cdot 10^5$	7830

Figure 8 shows the composition of the SDOF model including boundary and loading conditions. As shown in this figure, node 1 was fixed, while the other one was accelerated by applying the blast loading conditions. Figure 9 shows the loading condition in this analysis. Pressure-time curve can be simplified to triangular impulse types; however, the impulse, which represents the integrated area under the pressure-time

curve, is equal. Table 2 shows detailed properties of single degree of freedom model.

4.2. *Residual Wave Effect.* The blast load profiles can be expressed in various forms. Sometimes, the cyclic types sequentially repeat the positive and negative pressure phases, and the maximum overpressure emerges after this cyclic section,

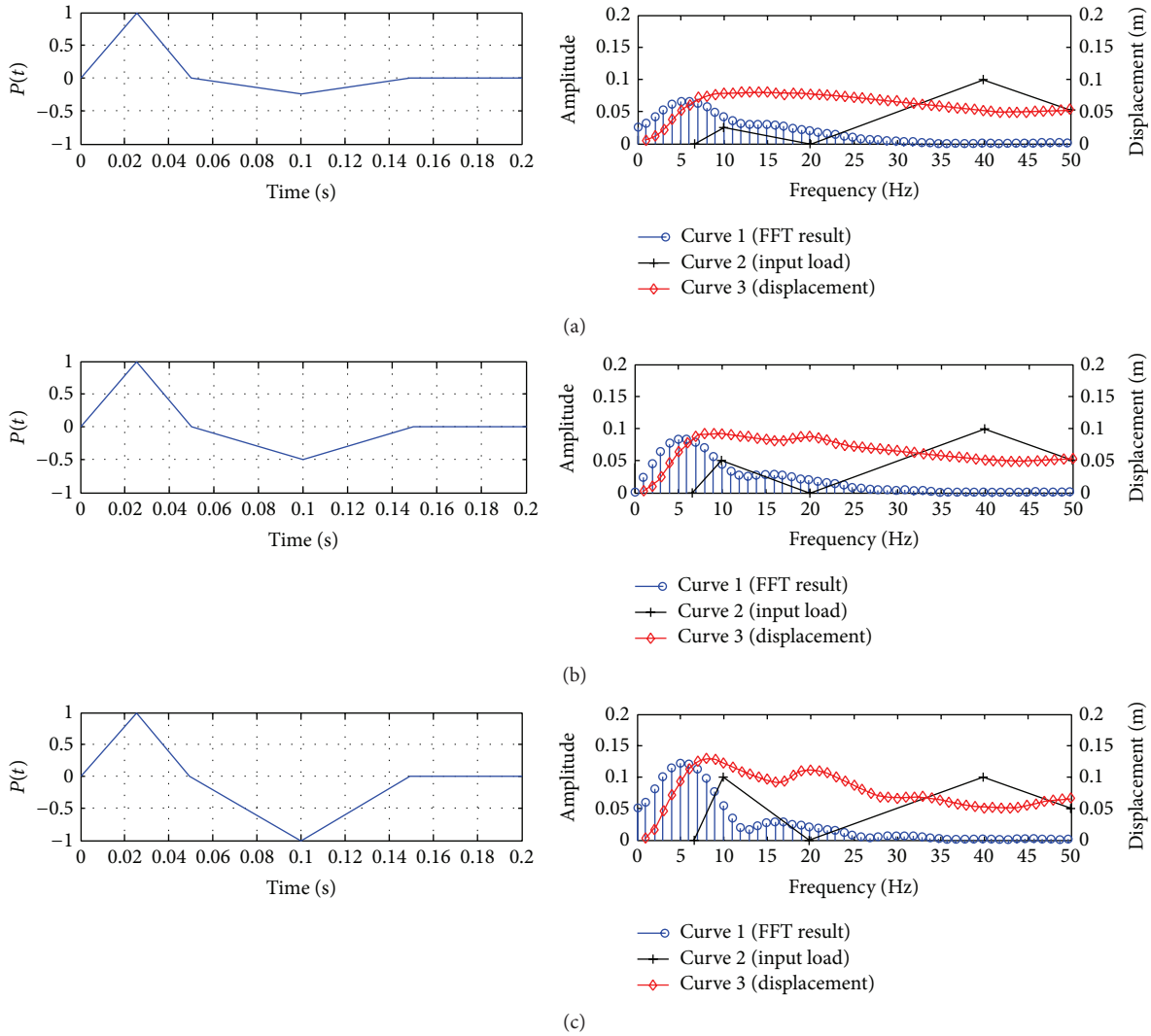


FIGURE 7: Fast Fourier Transform analysis considering the magnitude of maximum load in negative pressure phase. (a) Standard data. (b) Increasing the 2 times of negative maximum load. (c) Increasing the 4 times of negative maximum load.



FIGURE 8: Composition of single degree of freedom model.

as described in Figure 10. However, the maximum pressure value is generally indicated in the first section of the wave profile. Hence, it is very difficult to generalize the characteristics of the blast wave profile because of its arbitrary shape. An extensive analysis of FLACS output data revealed that the load shapes are similar to those shown in Figure 10(a) in a relatively less complex area which is far from the ignition position (more than 30 m). Industrial structures which requested blast resistant design are constructed based on maximum overpressure about 0.02 MPa. Generally, these blast load profiles have a main wave that is composed of relatively strong

two pressure phases compared to other waves. Consequently, the blast wave data specified in Figure 10(a) were almost of zero value. In other words, they are insignificant that they did not cause damage to structural system. Hence, target data of cyclic shape can be generalized as shown in Figure 10(b). As mentioned above, they have a main wave and residual waves. In this study, these residual waves' effect on structural dynamic response was investigated. To do this, the data that have three cycle pressure phases were selected as described in Figure 11(a). The peak pressures after the third cycle were very small, so these pressure phases were not considered

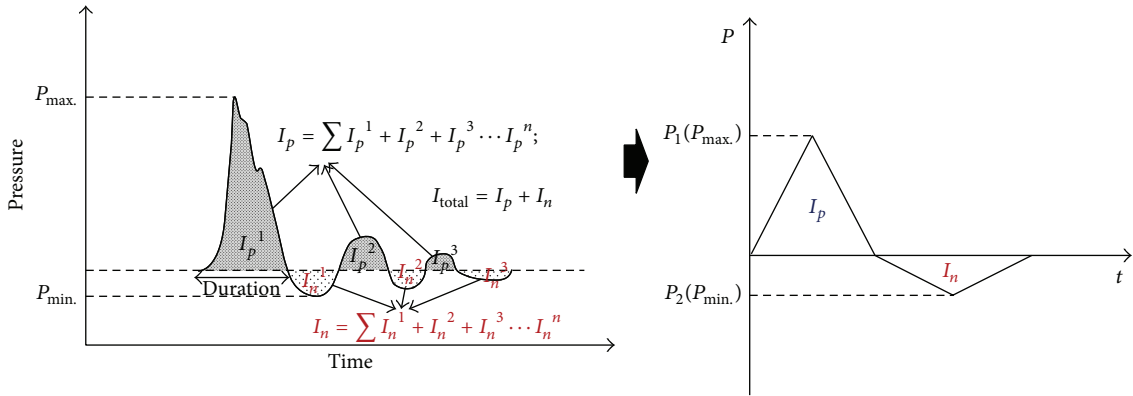


FIGURE 9: Loading condition of single degree of freedom.

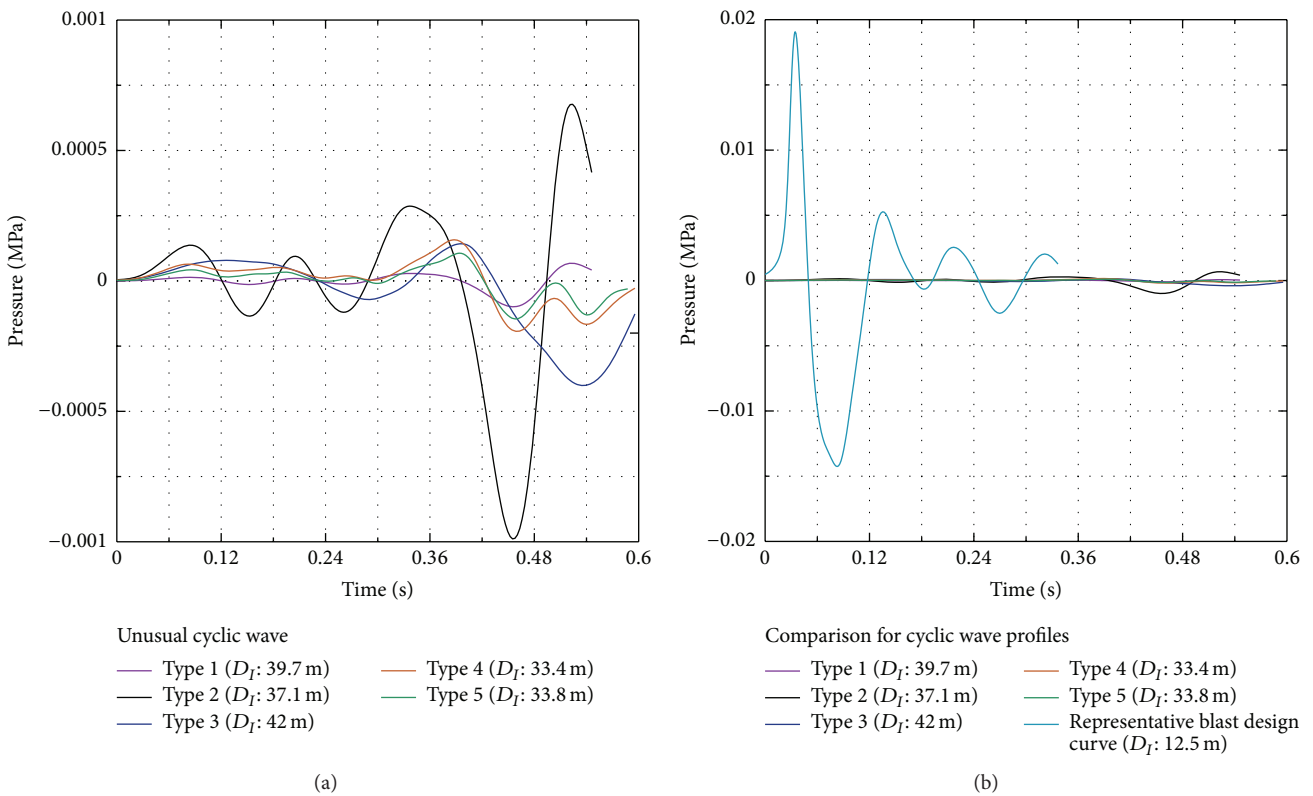


FIGURE 10: A variety of cyclic types in blast wave profiles. (a) In small pressure range. (b) Representative blast wave of cyclic type.

in residual wave effect analysis. Figure 11(b) shows the list of target data which are monitored by using the developed VBA code, and then the most severe two cases were selected based on the maximum pressure in pressure phases of second period. The values in Figure 12, 20%, and 30%, respectively, mean that the maximum pressures in second phase are 20% and 30% compared to maximum value in main phase. This loading condition was applied to investigate the residual effect on structural response. A series of analysis were carried out considering the number of cycles and duration according to cycles. Figure 12 shows the comparison results between

only applying the main wave and considering the other residual waves. The normalized displacement,  $Y_m/(P/k)$ , is shown against the normalized time  $(td/T_n)$  in the figure.  $P/k$  is the static deformation;  $T_d$  means the loading duration; and  $T_n$  is the natural period of the single degree of freedom model. Figure 12(a) indicates the displacement response of single degree of freedom (SDOF) model considering the loading condition which has the two cycles, and Figure 12(b) shows the results considering the three cycle waves according to maximum pressure values in second phase. The frequency and magnitude of the first cyclic wave are the most important

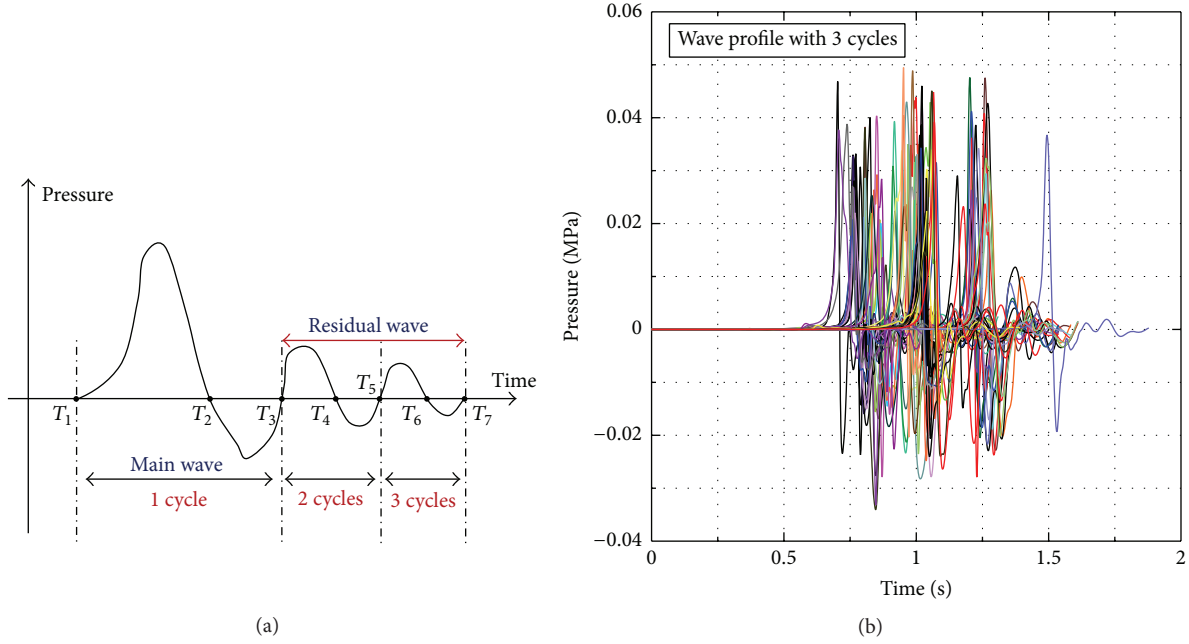


FIGURE 11: Residual/waves effect analysis. (a) The standard for the cyclic wave profiles. (b) Extraction of target data by VBA code.

factor of all the explosion wave profiles, and secondary and third residual waves may be neglected in qualitative analysis as long as the resonance effect is negligible.

**4.3. The Effect for Difference of Loading Rate.** The dynamic loads such as explosion wave show the very different load profiles according to explosion affecting parameters which mean source of explosion, geometrical characteristics of target structure, wind direction/speed, and so on. The peak overpressure and loading durations are most sensitive things related to these parameters. The time taken to reach the peak overpressure, especially, is very important. This is because the pressure by explosion wave is applied to structural body for an extremely short time. Thus, difference of explosion loading velocity can be a core element in structural damage and deformation [24]. In this study, a series of analysis have been performed to assess the effect of loading velocity on structural dynamic response. To do this, three types of triangular pulse loadings which have different loading velocity were applied to the single degree of freedom model. Figure 13(a) shows the results of peak displacement results considering the loading velocity of positive pressure phase, and Figure 13(b) means the same results according to the loading velocity of negative pressure phase. The  $y_m/y_{el}$  means the normalized maximum displacement, where  $y_m$  is the maximum displacement of SDOF model, and  $y_{el}$  means the static deformation at the yielding point due to applied loads. As shown in Figure 13, the loading velocity was affected by structural response, but it shows the different effect in each pressure phase. In case of positive pressure phase, loading velocity has a profound effect on response of SDOF model. Although it is less important considering relatively short loading compared to the natural period of structural system, it is influential in opposite case.

When the loading duration is longer than natural period, namely, the value of  $t_d/T_n$  is bigger than two, these loads generate the bigger displacement with faster loading velocity. However, the loading velocity in negative pressure phase has little impact on structural response as shown in Figure 13(b). As a result, it is obvious that the positive pressure phase has a bigger impact on structural member than negative pressure, and for the faster loading velocity, the bigger displacement occurred if  $t_d/T_n$  is bigger than two.

## 5. Results

In the present study, qualitative analyses of the dynamic response of structures subjected to various types of gas explosion loads were performed. Firstly, the extensive data analysis from CFD explosion simulations was carried out to investigate the characteristics of explosion load profiles. In this work, we evaluated various aspects of the profile parameters (i.e., the magnitude of overpressure, the relationship between positive pressure and negative pressure, and the shapes of explosion load profiles) using a monitoring tool that was developed using VBA code. Secondly, the characteristics of dynamic responses to considerable explosion load profiles were analyzed using a single degree of freedom model. The staple results from this research are summarized as follows:

- (i) The relationship between overpressure and congestion degree was found. Higher overpressures were produced by more congested areas than by less congested areas. The influence of the blast reflection can be minimized in less congested areas. Thus, it is important to retain proper clearance in hazardous facilities.
- (ii) Negative pressures must be considered in blast analyses to obtain accurate performance of the structure.

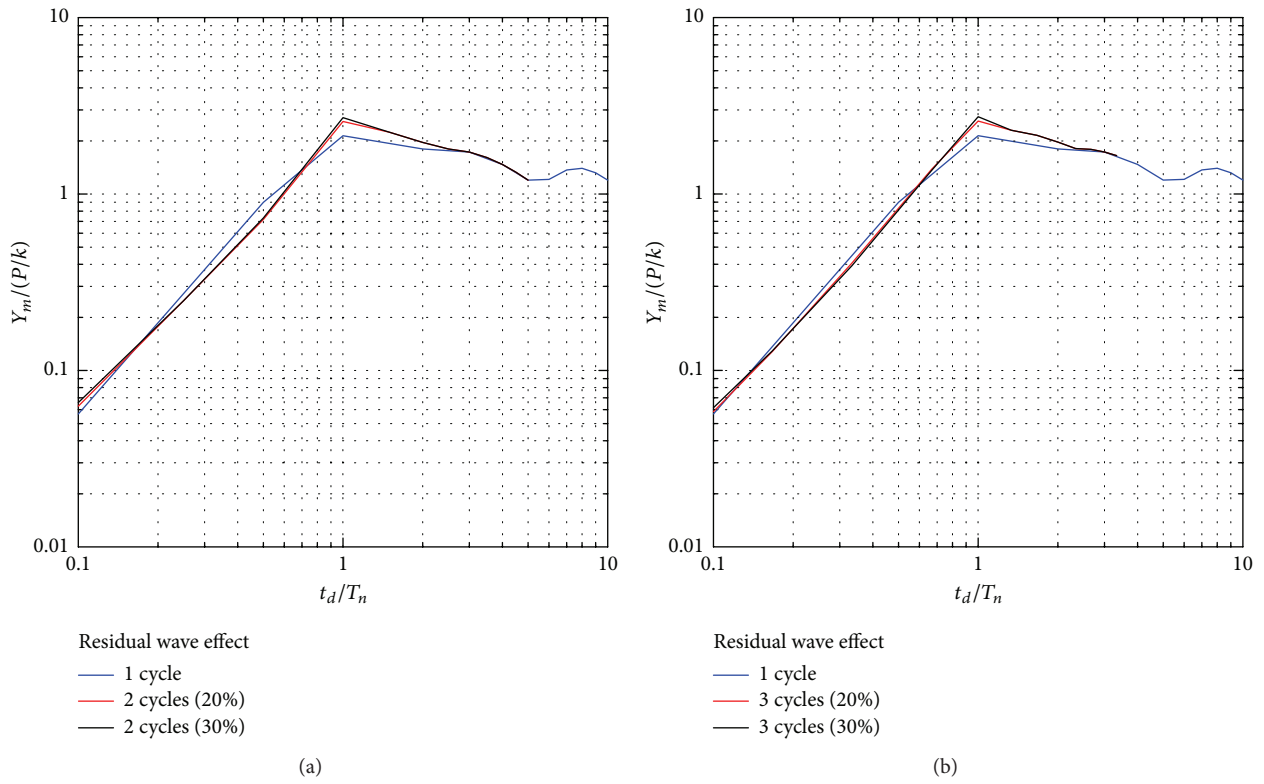


FIGURE 12: The results for maximum displacement response of single degree of freedom model according to the number of cycles: (a) 2 cycles; (b) 3 cycles.

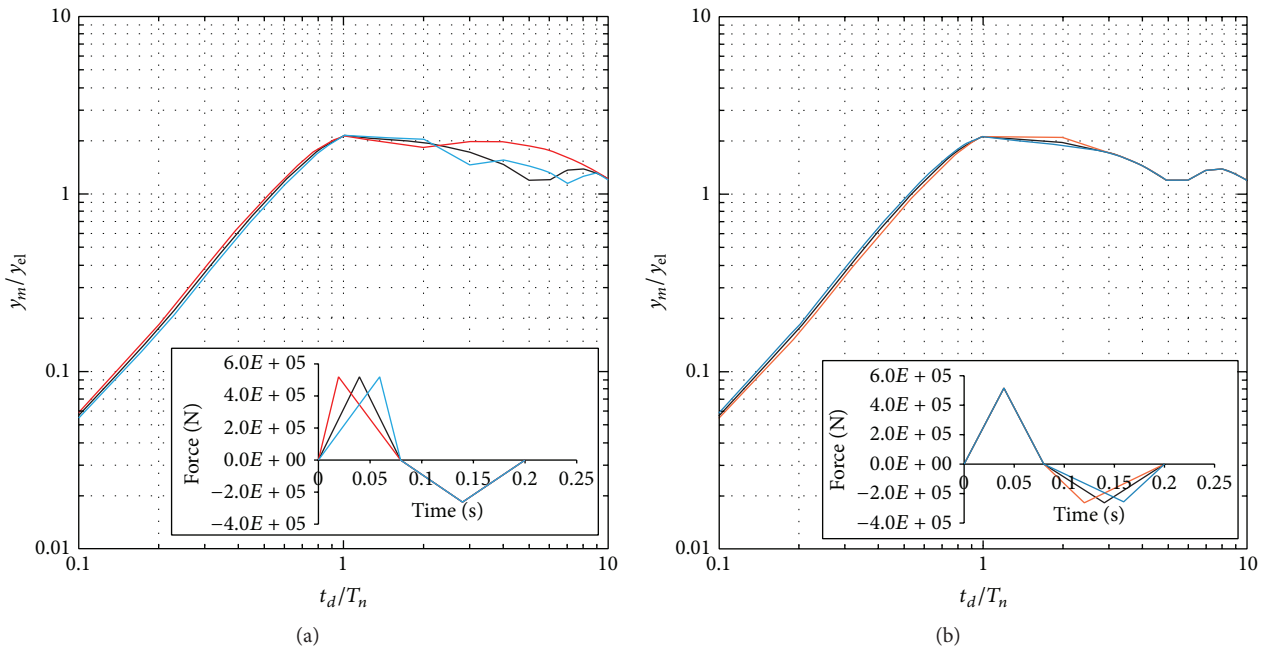


FIGURE 13: The analysis for the effect of loading rate (a) according to loading velocity of positive phase and (b) according to loading velocity of negative phase.

In some cases, the influence of including the negative phase can be considerable compared to using only positive pressure. The influence of negative pressure is close to that of positive pressure in the intensity range of 0.02–0.05 MPa and should be considered in the development of a load profile for offshore industries in this range.

- (iii) The Fast Fourier Transform (FFT) analysis was performed to characterize the dynamic response of the single degree of freedom (SDOF) model in the frequency domain corresponding to the intensity of explosion pressures in each phase. Through this analysis, it was found that the intensity of pressure in positive phase was a more dominant factor than in negative phase with respect to the dynamic response of the SDOF model.
- (iv) The residual wave effect on structural dynamic response was investigated. The frequency and magnitude of the first cyclic wave are the most important factor of all the explosion wave profiles. Secondary and third residual waves may be neglected in qualitative analysis as long as the resonance effect is negligible.
- (v) The loading velocity can be one of the main concerns on structural response, but the structure response due to the loading velocity differed in different phases. More deformation was caused by a higher loading velocity in the positive pressure phase, while the loading velocity did not affect the deformation level in the negative pressure phase.

## Competing Interests

The authors declare that they have no competing interests.

## Acknowledgments

This work was supported by the National Research Foundation of Korea (NRF) grant funded by the Korea government (MSIP) (no. 2015R1A2A1A15052688). This work was supported by the National Research Foundation of Korea (NRF) grant funded by the Korea government (MSIP) through GCRC-SOP (no. 2011-0030013).

## References

- [1] T. Ngo, P. Mendis, A. Gupta, and J. Ramsay, "Blast loading and blast effects on structures—an overview," *Electronic Journal of Structural Engineering*, vol. 7, pp. 76–91, 2007.
- [2] Y. Shi and M. G. Stewart, "Damage and risk assessment for reinforced concrete wall panels subjected to explosive blast loading," *International Journal of Impact Engineering*, vol. 85, pp. 5–19, 2015.
- [3] B. Yan, F. Liu, D. Song, and Z. Jiang, "Numerical study on damage mechanism of RC beams under close-in blast loading," *Engineering Failure Analysis*, vol. 51, pp. 9–19, 2015.
- [4] Q. Li, L. Qiao, G. Dasgupta, S. Ma, L. Wang, and J. Dong, "Blasting vibration safety criterion analysis with equivalent elastic boundary: based on accurate loading model," *Shock and Vibration*, vol. 2015, Article ID 604683, 10 pages, 2015.
- [5] K. Spranghers, I. Vasilakos, D. Lecompte, H. Sol, and J. Vanthomme, "Numerical simulation and experimental validation of the dynamic response of aluminum plates under free air explosions," *International Journal of Impact Engineering*, vol. 54, pp. 83–95, 2013.
- [6] C. M. Morison, "Dynamic response of walls and slabs by single-degree-of-freedom analysis—a critical review and revision," *International Journal of Impact Engineering*, vol. 32, no. 8, pp. 1214–1247, 2006.
- [7] Y. Qasrawi, P. J. Heffernan, and A. Fam, "Dynamic behaviour of concrete filled FRP tubes subjected to impact loading," *Engineering Structures*, vol. 100, pp. 212–225, 2015.
- [8] C. Bedon, C. Amadio, and A. Sinico, "Numerical and analytical investigation on the dynamic buckling behavior of glass columns under blast," *Engineering Structures*, vol. 79, pp. 322–340, 2014.
- [9] K. Fischer and I. Häring, "SDOF response model parameters from dynamic blast loading experiments," *Engineering Structures*, vol. 31, no. 8, pp. 1677–1686, 2009.
- [10] S. E. Rigby, A. Tyas, and T. Bennett, "Elastic-plastic response of plates subjected to cleared blast loads," *International Journal of Impact Engineering*, vol. 66, pp. 37–47, 2014.
- [11] L. Jun and H. Hong, "Development of a simplified numerical method for structural response analysis to blast load," *Procedia Engineering*, vol. 14, pp. 2558–2566, 2011.
- [12] T. Krauthammer and A. Altenberg, "Negative phase blast effects on glass panels," *International Journal of Impact Engineering*, vol. 24, no. 1, pp. 1–17, 2000.
- [13] A. K. Chopra, *Dynamic of Structures: Theory and Applications to Earthquake Engineering*, Pearson Education, 3rd edition, 2007.
- [14] O. R. Hansen and D. M. Johnson, "Improved far-field blast predictions from fast deflagrations, DDTs and detonations of vapour clouds using FLACS CFD," *Journal of Loss Prevention in the Process Industries*, vol. 35, pp. 293–306, 2015.
- [15] O. R. Hansen, F. Gavelli, M. Ichard, and S. G. Davis, "Validation of FLACS against experimental data sets from the model evaluation database for LNG vapour dispersion," *Journal of Loss Prevention in the Process Industries*, vol. 23, pp. 857–877, 2010.
- [16] M. H. Kim, B. J. Koo, R. M. Mercier, and E. G. Ward, "Vessel/mooring/riser coupled dynamic analysis of a turret-moored FPSO compared with OTRC experiment," *Ocean Engineering*, vol. 32, no. 14–15, pp. 1780–1802, 2005.
- [17] J.-H. Hwang, M.-I. Roh, and K.-Y. Lee, "Determination of the optimal operating conditions of the dual mixed refrigerant cycle for the LNG FPSO topside liquefaction process," *Computers and Chemical Engineering*, vol. 49, pp. 25–36, 2013.
- [18] F. Chille, J. R. Bakke, and K. V. Wingerden, "Use of CFD tools for prediction of explosion loads," in *Proceedings of the Handling Exceptions in Structural Engineering*, Roma, Italy, November 2008.
- [19] ISO, "Glass in building—explosion-resistant security glazing—test and classification for arena air-blast loading," ISO 16933:2007, International Organization for Standardization (ISO), London, UK, 2007.
- [20] UK Offshore Operators Association (UKOOA), *Fire and Explosion Guidance Part 1: Avoidance and Mitigation of Explosions*, UK Offshore Operators Association, London, UK, 2003.
- [21] British Standards Institution, "Petroleum and natural gas industries—fixed steel offshore structures," BS EN ISO 19902, 2005.

- [22] U. S. Lee, S. H. Kim, and J. Y. Cho, "Dynamic analysis of the linear discrete dynamic systems subjected to the initial conditions by using an FFT-based spectral analysis method," *Journal of Sound and Vibration*, vol. 288, no. 1-2, pp. 293–306, 2005.
- [23] A. S. Fallah and L. A. Louca, "Pressure-impulse diagrams for elastic-plastic-hardening and softening single-degree-of-freedom models subjected to blast loading," *International Journal of Impact Engineering*, vol. 34, no. 4, pp. 823–842, 2007.
- [24] X. Lin, Y. X. Zhang, and P. J. Hazell, "Modelling the response of reinforced concrete panels under blast loading," *Materials and Design*, vol. 56, pp. 620–628, 2014.

## Research Article

# Crash-Induced Vibration and Safety Assessment of Breakaway-Type Post Structures Made of High Anticorrosion Steels

**Sang-Youl Lee**

*Department of Civil Engineering, Andong National University, Andong-si, Gyeongsangbuk-do 760-749, Republic of Korea*

Correspondence should be addressed to Sang-Youl Lee; [lsy@anu.ac.kr](mailto:lsy@anu.ac.kr)

Received 24 November 2015; Accepted 23 February 2016

Academic Editor: Chao Tao

Copyright © 2016 Sang-Youl Lee. This is an open access article distributed under the Creative Commons Attribution License, which permits unrestricted use, distribution, and reproduction in any medium, provided the original work is properly cited.

This study deals with car crash effects and passenger safety assessment of post structures with breakaway types using high performance steel materials. To disperse the impact force when a car crashes into a post, the post could be designed with a breakaway feature. In this study, we used a new high anticorrosion steel for the development of advanced breakaways. Based on the improved Cowper-Symonds model, specific physical properties to the high anticorrosion steel were determined. In particular, the complex mechanism of breakaways was studied using various parameters. The parametric studies are focused on the various effects of car crash on the structural performance and passenger safety of breakaway-type posts. The combined effects of using different steel materials on the dynamic behaviors are also investigated.

## 1. Introduction

Street lights or signboard posts, which are standard roadside structures, are essential elements for the safe passage of vehicles and pedestrians. These facilities are designed to withstand wind loads because of their function as auxiliary roadside structures. However, in terms of automobile crashes, they are hazardous elements on the road.

In sites where there are no guard rails on the roadside, a crash into such a post will cause the vehicle to absorb much of the impact energy, significantly endangering the passengers of the cars. To avoid this problem, a recent study conducted in Korea assessed passenger safety for coupled, rounded posts. A variety of researches in the car crashes or impacts have been performed in the last two decades [1–7]. However, the kinetic examination on the breakaway of the posts subjected to car crashes has not been sufficiently investigated. Recently, techniques for considering strain rate effects are evolved. Choung et al. [8] studied dynamic hardening behaviors of various marine structural steels considering dependencies on strain rate and temperature. In general, the material data obtained from the real high-velocity tensile test can describe accurately the nonlinearity of dynamic behavior. However,

it requires high expenses and trial-and-error efforts for the complicated experimental setup. On the other hand, the dynamic approach based on Cowper-Symonds model [9] is free from such requirements and thus can yield more efficient results for high strain rate effects than those of the direct high-velocity tensile test [10]. This allows for convenient use of Cowper-Symonds model. Many Cowper-Symonds theories exist but they are mostly applicable to existing steel structures or rigid jointed posts at the present time.

In this study, we perform a simulation with high anticorrosion breakaway posts capable of absorbing impacts and calculated the breakage stress to assess passenger safety. Passenger safety was assessed by calculating the THIV (Theoretical Head Impact Velocity) and PHD (Post-Impact Head Deceleration) [11]. This process compares normal steel materials (SS400) and high anticorrosion steel materials (SM490). In order to endow specific physical properties to these materials, we used an improved version of the Cowper-Symonds model. The final goal of this study is to assess passenger safety in a car impacting the post. For passenger safety assessment, the THIV requirement is 33 km/h or lower, while the PHD requirement is 20 or less to ensure safety of the passenger. For this reason, we use a coupled breakaway

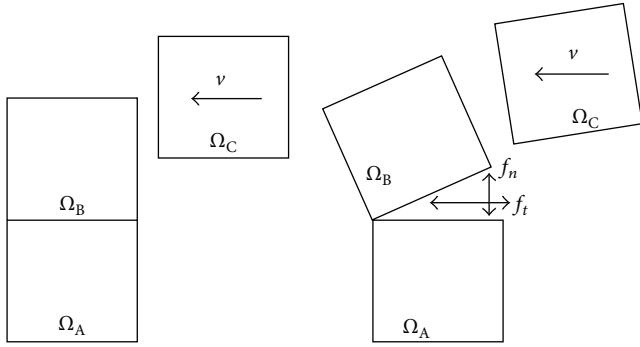


FIGURE 1: Detachment of the blocks due to impact.

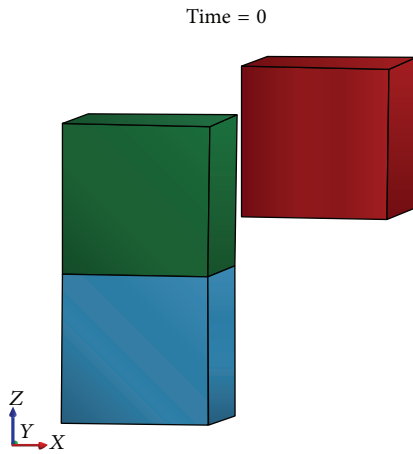


FIGURE 2: Block impact under full contact conditions (0.0 sec).

post modeling to assess the risks to which passengers are exposed. The focus is on car crash-induced vibration effects for different material properties of breakaway posts. To obtain the results coupled with complicated high strain rate effects, this study uses the modified Cowper-Symonds formulation.

## 2. Theoretical Formulation

For completeness, the mechanical behaviors and the relevant formulas in the finite element crash analysis using LS-DYNA are reviewed below [10, 12]. If two blocks, namely,  $\Omega_A$  and  $\Omega_B$ , collide with block element  $\Omega_C$  at a velocity of  $v$ , the process is as shown in Figure 1. Assuming that blocks  $\Omega_A$  and  $\Omega_B$  are completely attached without any gaps, the force at the interface generated in the finite elements after the crash into block  $\Omega_C$  can be divided into the vertical force  $f_n$  and the shearing force  $f_t$ . In normal crash interpretations, the vertical force is higher than the shearing force. Especially when one considers an impact breakaway, the vertical force created inside the finite element occurs at the interface due to the momentum of the post.

To represent the mechanical concepts, we use LS-DYNA and the TIEDBREAK\_NODES\_ONLY option to simulate the distribution of the force on the surface of block  $\Omega_A$  in a full contact (Figures 2–4). The bottom of block  $\Omega_A$  is fixed,

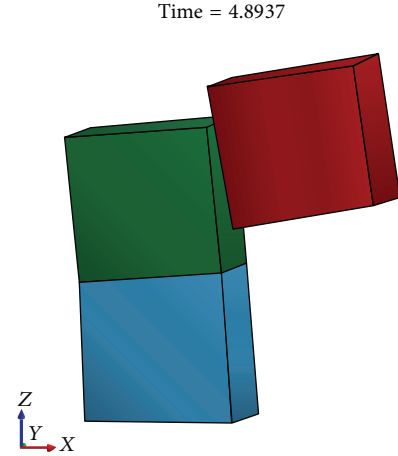


FIGURE 3: Block impact under full contact conditions (4.8 sec).

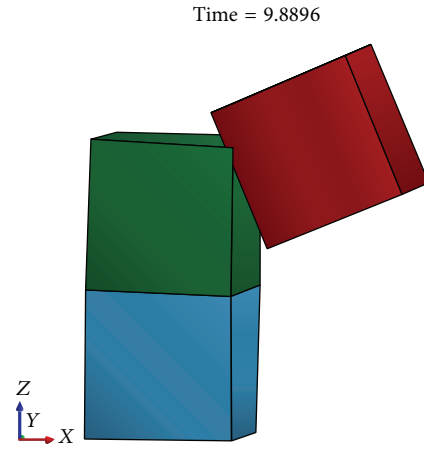


FIGURE 4: Block impact under full contact conditions (9.8 sec).

and blocks  $\Omega_A$  and  $\Omega_B$  are assumed to be in complete contact. Block  $\Omega_C$  proceeds in the  $x$ -direction at 0.1 m/s to crash into block  $\Omega_B$ . Figure 5 shows distributions of the vertical and shearing force in block element  $\Omega_A$ . In this simulation, simple block models are used and the point of impact is lower than the center of gravity. This is due to the shearing force to become higher. Concerning the post, it is the vertical force that affects the breakaway most significantly. Therefore, in this study the influence from the shearing force is ignored. The maximum vertical force is 2.1 N at 3.83 seconds, and the impact breakaway under the following conditions is applied. For this reason, among the LS-DYNA input TIEDBREAK\_NODES\_ONLY options NFLF (normal failure force) is 1.0 N, while SFLF (shear failure force) is  $1.0 \times 10^6$  N. Consider

$$f_n < f_n - \max = 2.1 \text{ N (Maximum normal force)}. \quad (1)$$

Figures 6-7 show the behavior of the blocks after the impact when the vertical force breakaway conditions are applied as set forth above. Figure 8 shows the distribution of the shearing stress in the block  $\Omega_A$  element. All vertical forces are within the range of 1.0 N. This provides us with a clue that

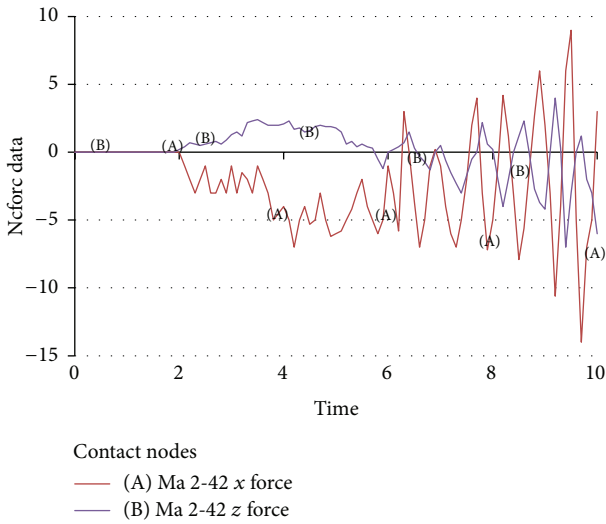


FIGURE 5: Distributions of the vertical and shearing force in block element  $\Omega_A$  (z-axis: vertical force, x-axis: shearing force).

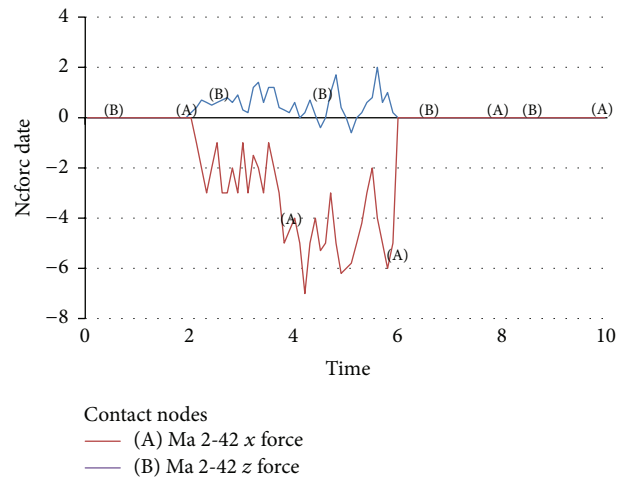


FIGURE 8: Distributions of the vertical and shearing force in block element  $\Omega_A$  in consideration of the breakaway conditions (z-axis: vertical force, x-axis: shearing force).

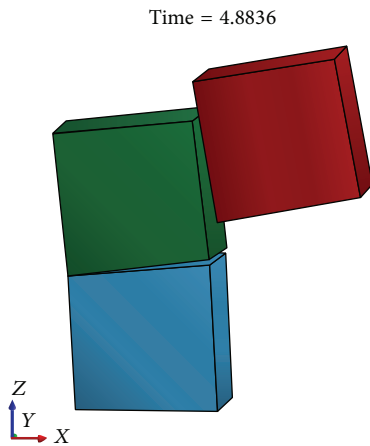


FIGURE 6: Block impact under breakaway conditions in (1) (4.8 sec).

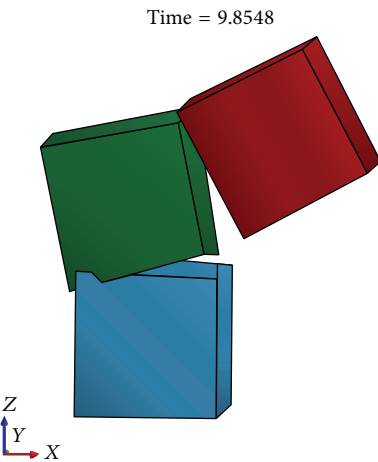


FIGURE 7: Block impact under the breakaway conditions in (1) (9.8 sec).

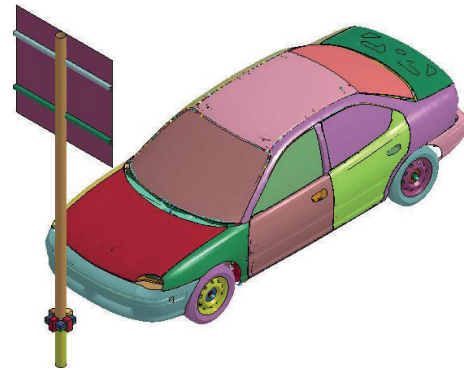


FIGURE 9: Breakaway-type post model using shell and solid elements.

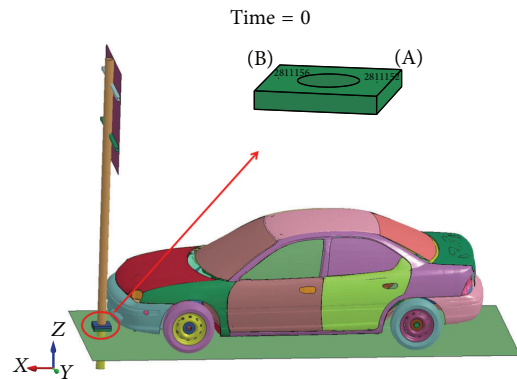


FIGURE 10: Measuring points of the failure force at the base of the post.

the maximum vertical force is calculated under full contact when the blocks are detached. A failure force of smaller value causes the detachment of the elements.

### 3. Finite Element Crash Model

The breakaway post is deformed when a car crashes into it. It is designed to break away when the threshold stress value

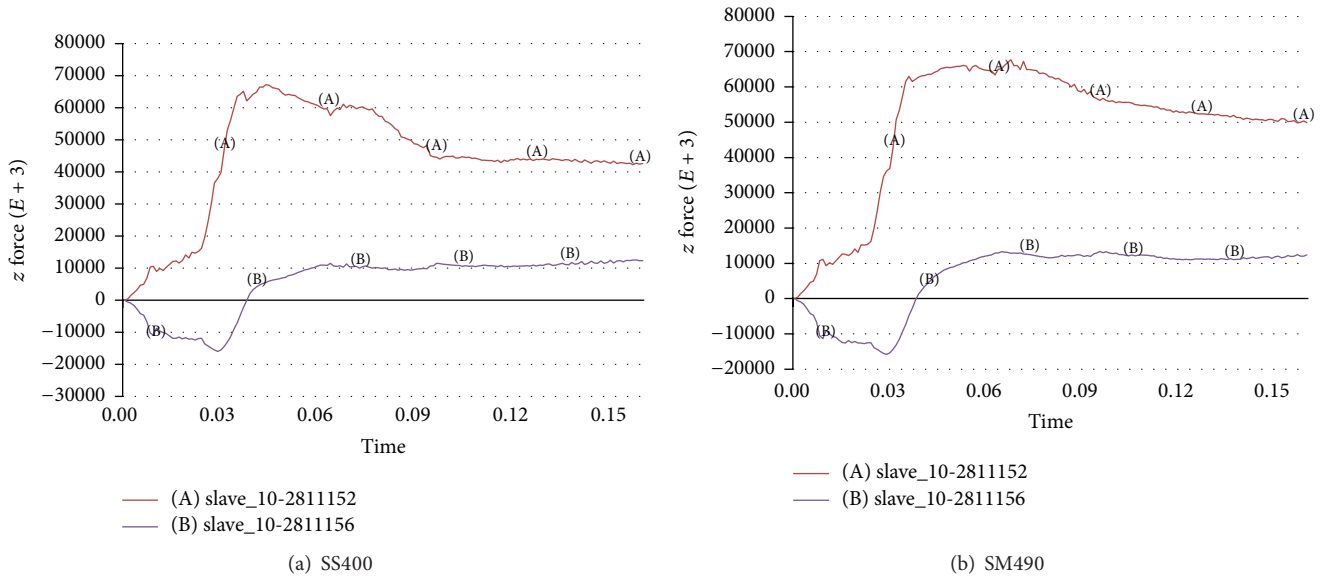


FIGURE 11: Induced vertical forces in the  $z$ -axis at the point of failure force measurement for the full contact condition.

is exceeded during impact. The finite element formulation described earlier is now implemented to compare the results of our technique with those obtained for different material properties and also to study the influences of breakaway on the crash analysis of post structures. In the finite element crash model, the height of the post used for this study is 3,200 mm for the upper post and 500 mm for the lower post, totaling 3,700 mm. The lower post is buried under the ground and modeled to be coupled but with freedom in six directions as shown in Figure 9 [13]. It is also assumed that there is a signboard that is 1,250 mm  $\times$  1,200 mm and completely attached to the post. The upper and lower posts are modeled to break away once the threshold failure force is reached. The steel pipe post modeled has a diameter of 101.6 mm and a wall thickness of 4.0 mm using a shell element. The same parameters are given to the signboard, which is modeled as a shell element with 4.0 mm wall thickness. On the other hand, the four facing clips and two slip bases are built in solid elements.

Since the purpose of this study is to compare the safety of passengers with posts built with SS400 and those built with SM490, each of these materials is applied to the post and the results are compared. The material model is based on the Cowper-Symonds equation, with a view to consider the dynamic effect of the vehicle.

In this study, a Dodge Neon is chosen for the passenger vehicle model as provided by NCAC [14], the National Crash Analysis Center of the United States. The physical properties of most of the elements in the vehicle are yield stress of 400 MPa and elastic modulus of 210,000 MPa. The impact interactions between the post and vehicle are limited by the contact options in the LS-DYNA software. In the simulation in this study, the following crash conditions options are also used:

- (i) `Automatic_single_surface`: it removes the domain overlapping effect when there is a crash to enhance

the accuracy of the results. This option was applied only to the vehicle model.

- (ii) `Automatic_surface_to_surface`: it endows the contact conditions between the post and vehicle and the post and auxiliary elements.
- (iii) `Tied_surface_to_surface_failure`: it endows the contact conditions between the detached posts. This option requires the maximum vertical stress and shearing stress at the time of the breakaway. This is endowed by  $f_{t-max}$ , which is calculated in advance.

The crash simulation in LS-DYNA begins basically with the explicit time interpretation. In case of the explicit analysis, there is a problem that the user has to define an arbitrary time span. For example, narrower spans produce lower accuracy results. In this simulation, we use the automatic time increment option supported by LS-DYNA, because the contact conditions are very complicated. In the numerical test, a total of eighteen cases are simulated. Of these, nine have the posts built with SS400, while the rest had the posts built with SM490. We assumed the wall thickness of the posts to be the same to determine the conditions of breakaway by material.

## 4. Numerical Examples

**4.1. Case I: Full Contacted Posts.** Before analyzing breakaway-type posts, we perform crash analyses of the posts under full contact conditions. As mentioned earlier, it is necessary to identify the failure force at the point of breakage under full contact conditions to determine the breakaway load. This is done by the analysis of the full contact case. As shown in Figure 10, the failure force is measured in two positions at the base of the post (A node: 2,811,152 nodes, B node: 2,811,156 nodes).

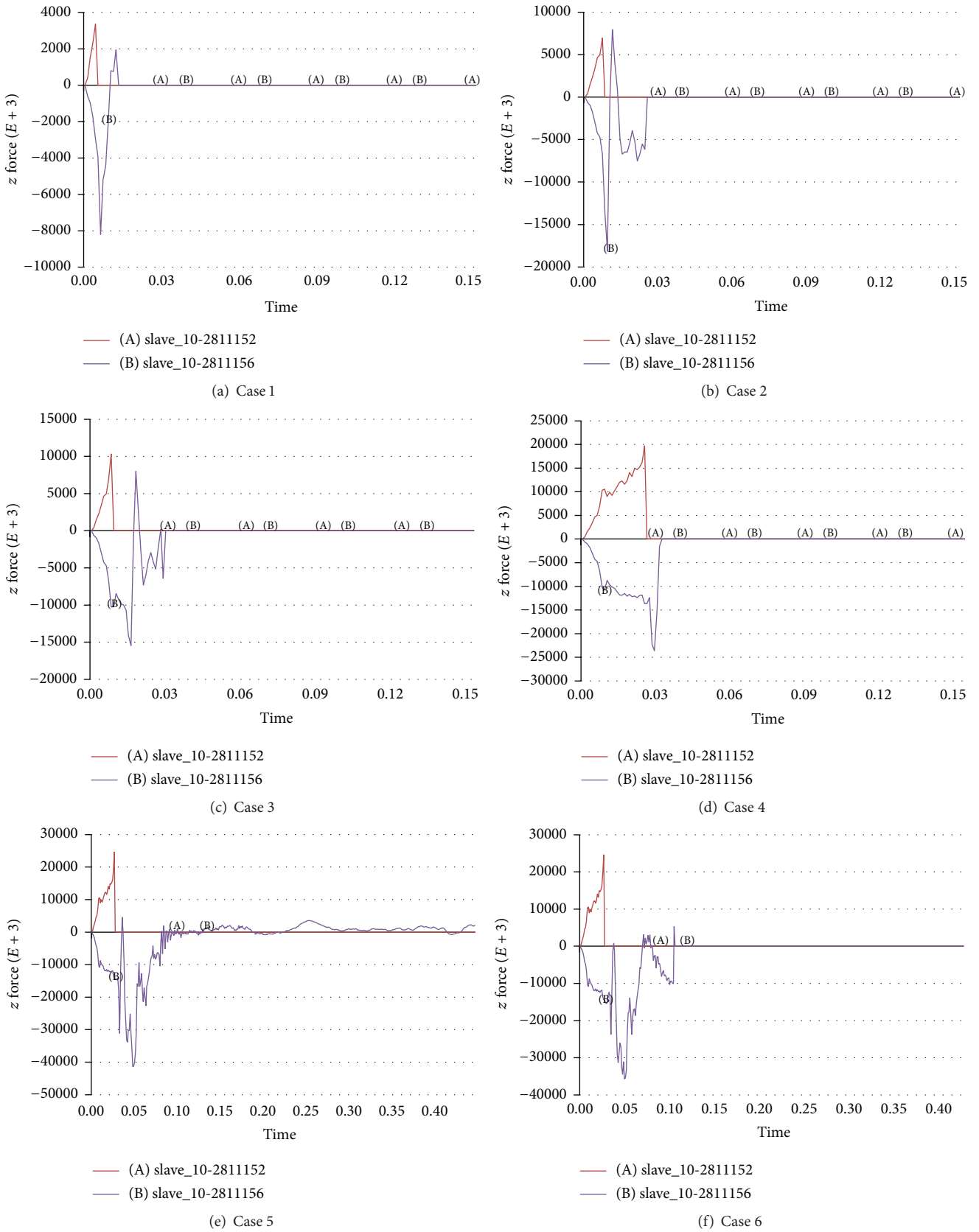


FIGURE 12: Continued.

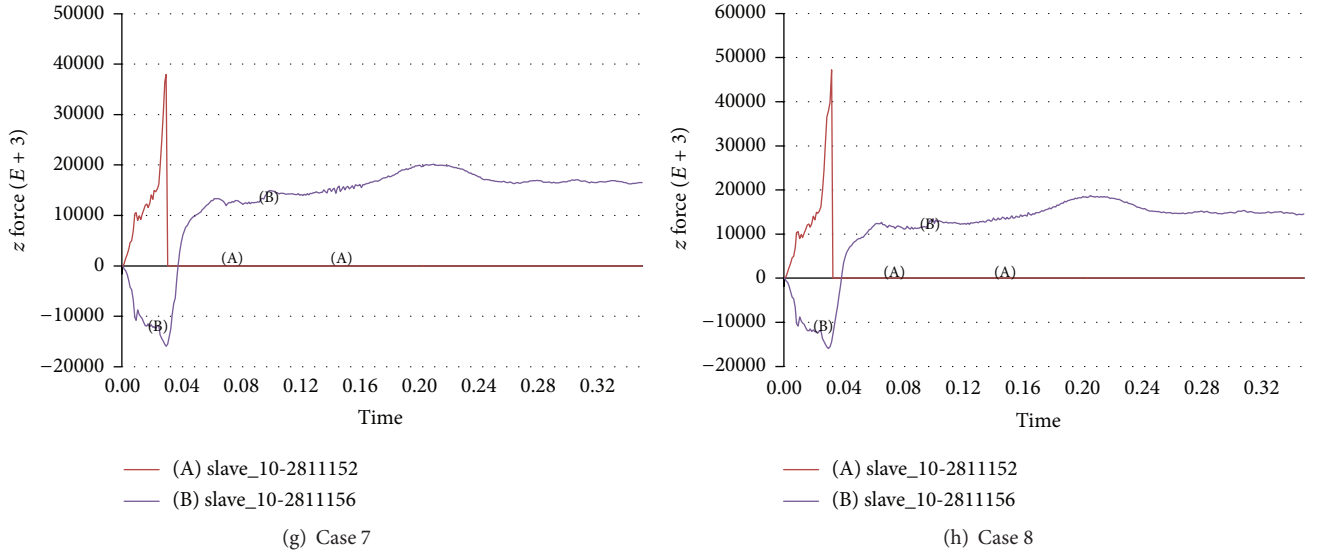


FIGURE 12: Induced vertical forces in the  $z$ -axis at the point of failure force measurement (cases 1~8).

TABLE 1: Analysis cases by different breakaway conditions ( $f_{t-max}$  (N)).

	Case 1	Case 2	Case 3	Case 4	Case 5	Case 6	Case 7	Case 8
SS400	5,000	10,000	15,000	20,000	25,000	30,000	40,000	50,000
SM490	Case 9	Case 10	Case 11	Case 12	Case 13	Case 14	Case 15	Case 16
	5,000	10,000	15,000	20,000	25,000	30,000	40,000	50,000

Figure 11 shows the  $z$ -axis vertical forces obtained at the two nodes when the posts built with SS400 and SM490 are in full contact. The vertical force over time is higher with the B node compared to the A node. In the cases with SS400, the value rose up to 67,200 N, while the values in the SM490 scenario rose up to 677,000 N. With the maximum vertical forces of these graphs as the starting point, we performed simulations for the failure forces presented in Table 1.

**4.2. Case II: Breakaway-Type Posts.** The interpretations of each case in accordance with the breakaway conditions in (1) are shown in Table 1. Table 1 shows the different contact conditions between the detached posts. The contact conditions are defined to the maximum vertical forces at the time of the breakaway. Each force is determined from results for the full contact as shown in Figure 11.

Figures 12(a)–12(h) show the induced vertical forces at the A and B nodes for SS400. Based on the failure conditions of each case, the induced vertical forces are shown to be within the failure force range. As the failure force increased, breakaway at A node occurred as expected, while the B node showed an increase from the compression force to the tensile force. Such a phenomenon can be observed in cases 7 and 8. The results of the simulation indicate that the posts are still upright after the crash. That is, the breakage at A node happens from case 7 on, but at B node, the breakage never occurs.

Figures 13(a)–13(h) show induced vertical forces at A and B nodes for SM490. While the graph shows a similar tendency with that of the SS400 material, the overall vertical force is higher. However, from case 14, there is a vertical force generated at the B node that prevents the post from breaking away. This indicates a failure force condition of 30,000 N, which is lower than the failure force condition of case 7 for SS400, which was 40,000 N. We may conclude from these results that this is because of the increased physical strength of the post due to using a material of higher strength, causing more tensile force to the breakaway base of the post. In summary, the threshold of breakaway for SM490 is lower than that of SS400.

Figures 14-15 show the deformed shapes of the breakaway-type post and car against the crash for different cases. As expected, it can be observed from figures that posts made of SM490 are not breakaway or less deformed when compared to SS490 for the same failure condition because of the increased stiffness.

**4.3. Case III: Passenger Safety Performance Assessment.** Figures 16-17 show induced THIV and PHD for measuring the vehicles acceleration in  $x$ -,  $y$ -, and  $z$ -axis as well as the rotational velocity [15]. Assessments of the THIV and PHD are performed based on the passenger safety performance assessment items [11]. In the case of THIV, passenger safety could be guaranteed when the speed is 33 km/h.

The passenger car models were built based on the models provided by NCAC. We followed the guidelines (SB2 and

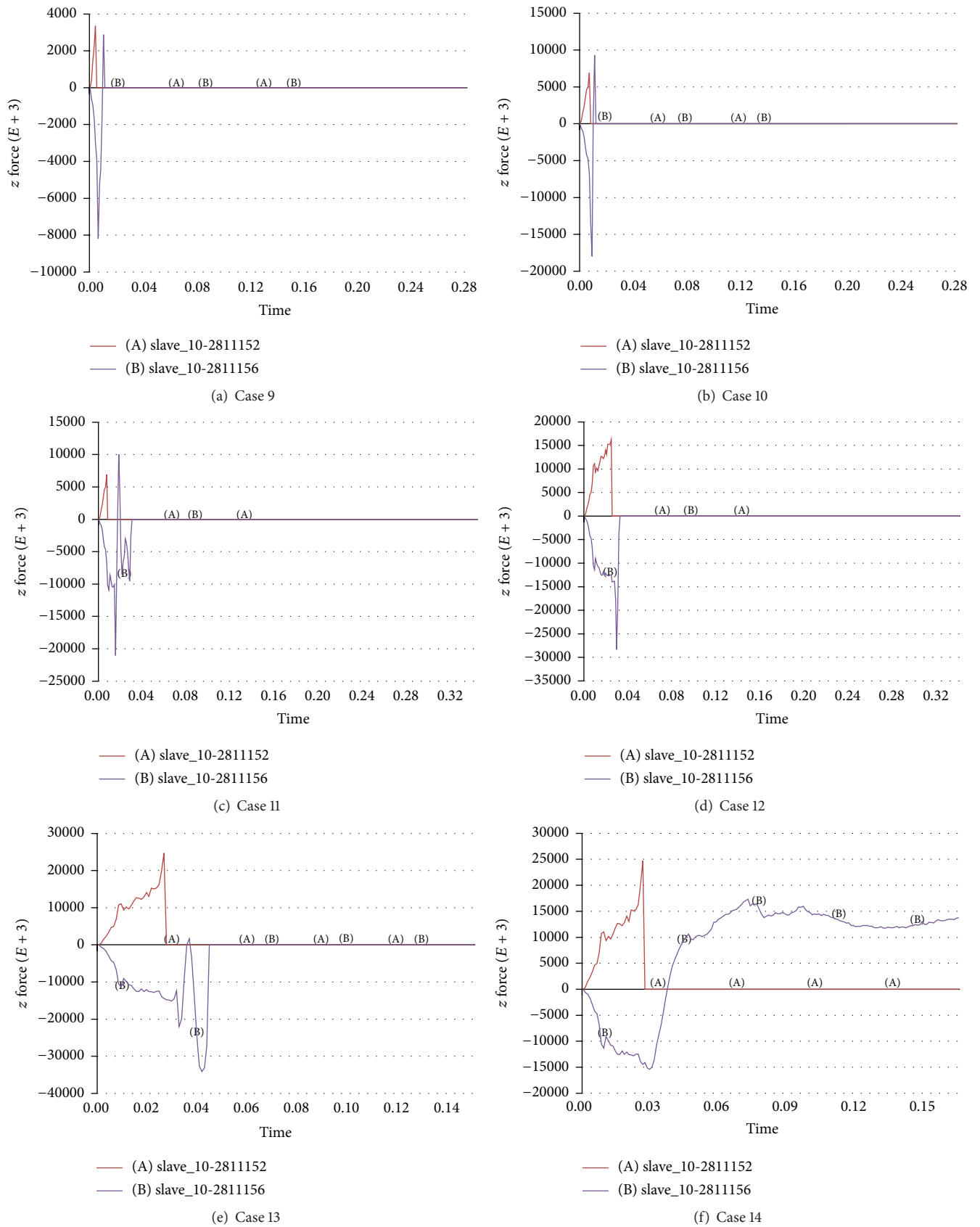


FIGURE 13: Continued.

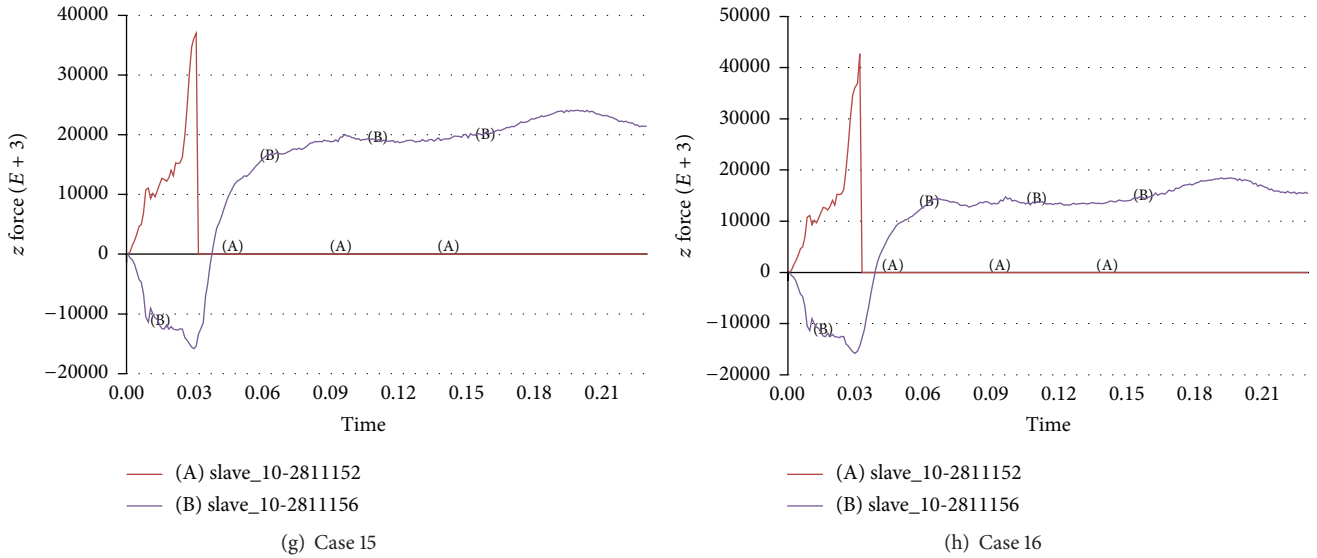


FIGURE 13: Induced vertical forces in the z-axis at the point of failure force measurement (cases 9~16, SM490).

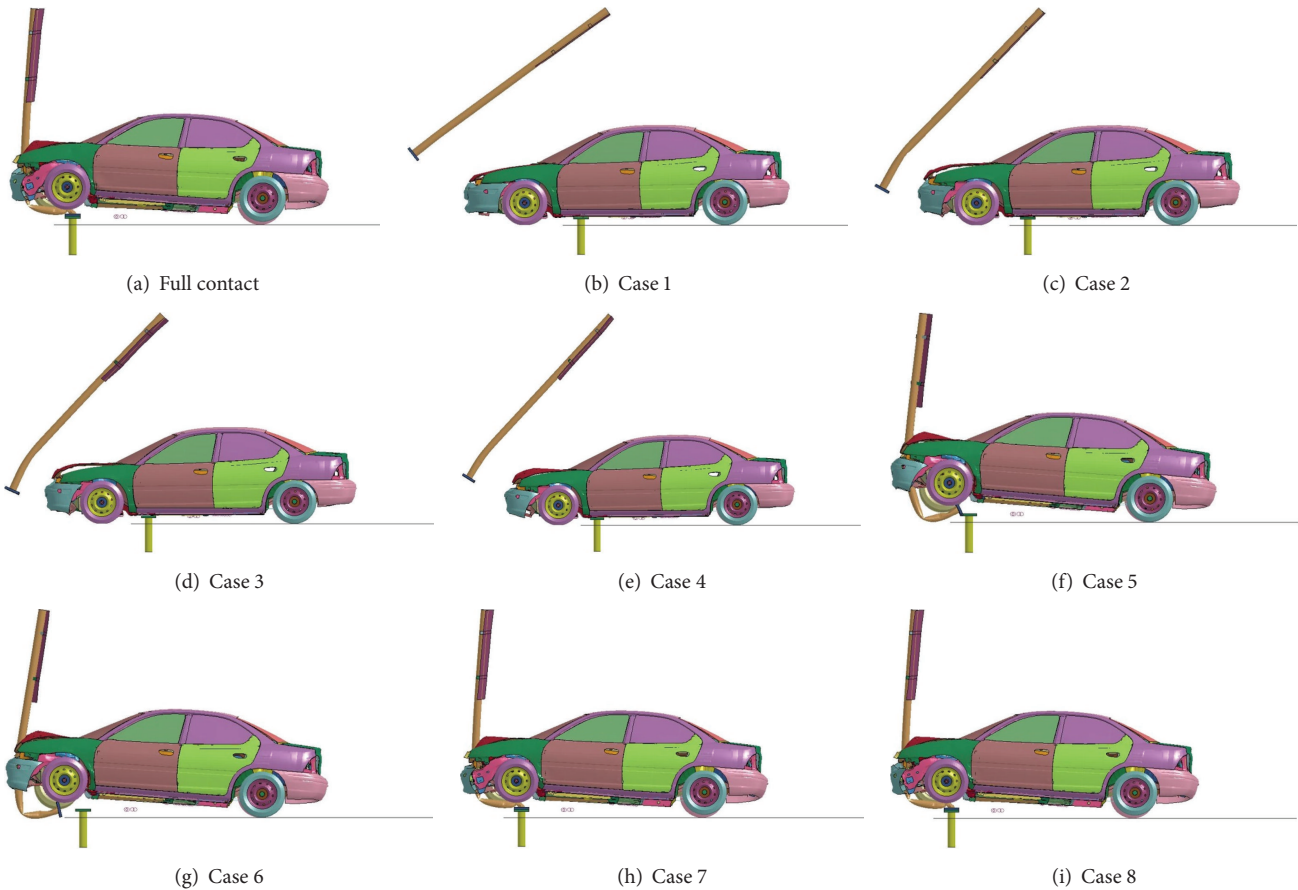


FIGURE 14: Deformed shapes for different cases (SS400).

SB4 grades) to test the rails in Korea as per the Guideline to Perform Crash Tests for Road Side Barriers [16]. In the SB2 and SB4 grade regulation, the mass of impact vehicle is 900 kg and impact speed is 80 km/h. In this study, the requirement is

satisfied for both SS400 and SM490, within the failure force range of 40,000 N. However, in the case of PHD, the SS400 satisfied the requirement under 50,000 N, while SM490 does so under 40,000 N. If we relate this to the breakage results

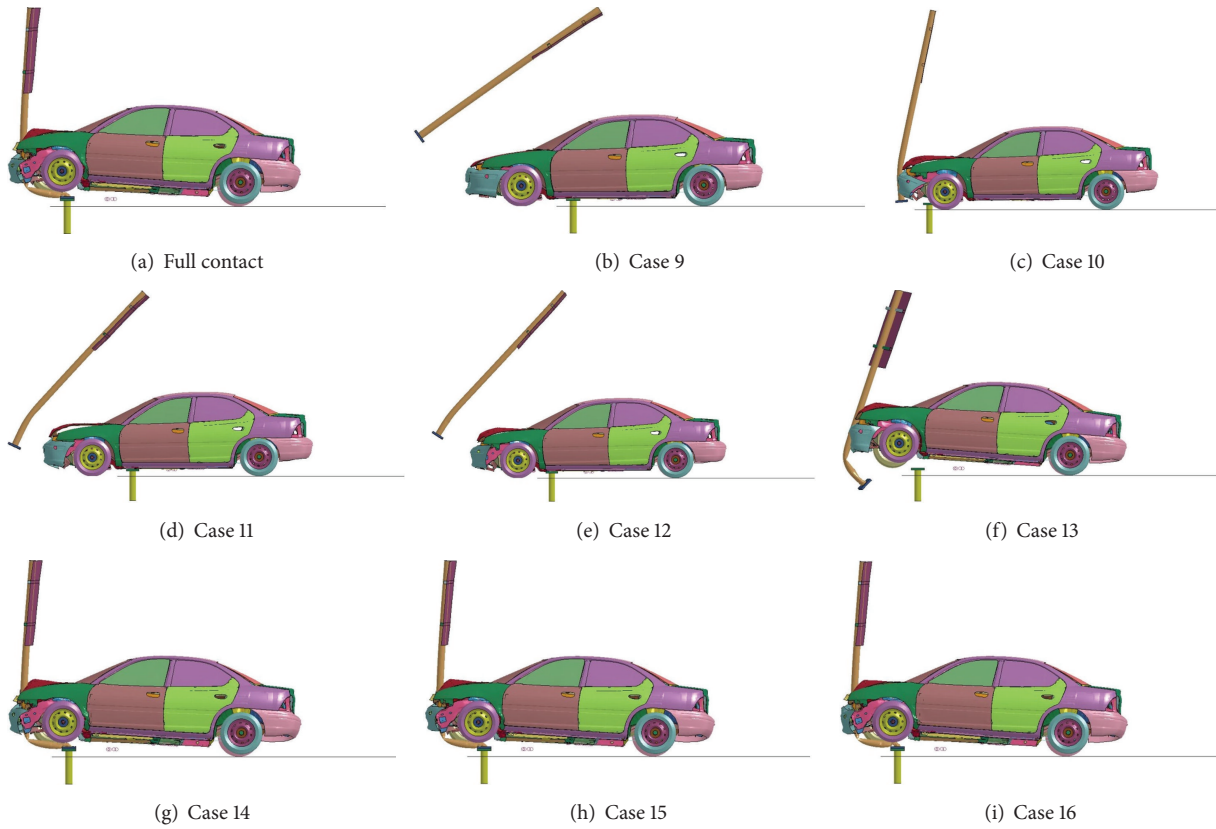


FIGURE 15: Deformed shapes for different cases (SM490).

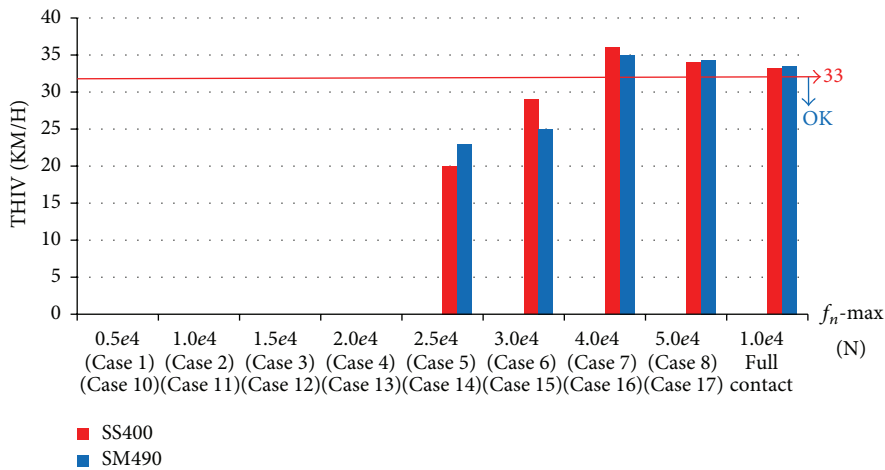


FIGURE 16: THIV for different cases.

discussed earlier, the SS400 is believed to have satisfied the THIV requirement after the breakaway, while SM490 satisfied the THIV requirement in case 14, where the breakaway did not occur. The same is true with the PHD. In other words, the condition that both THIV and PHD should be satisfied for SS400 and SM490 is that the failure force is lower than 40,000 N.

### 5. Conclusion

In this study, we performed the assessment of passenger safety for posts and signboards that are standard roadside installations. To disperse the impact force when a car crashes into a post, the post is designed with a breakaway feature. The simulation is performed with two different materials: normal

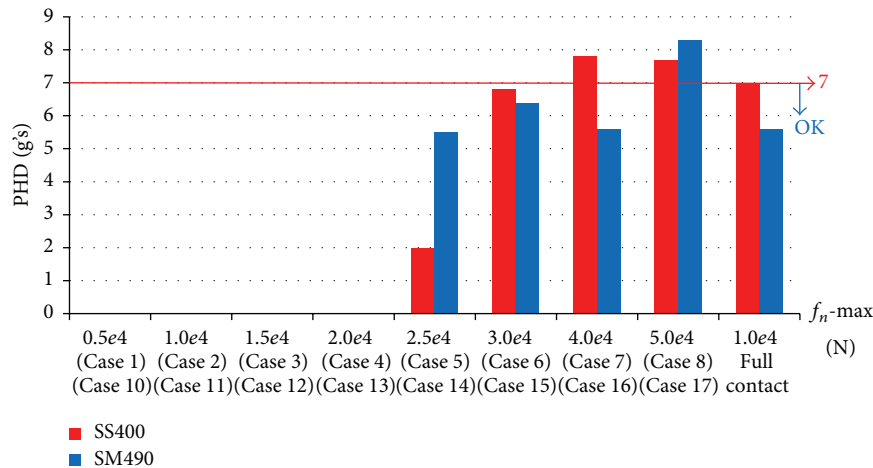


FIGURE 17: PHD for different cases.

steel (SS400) and high anticorrosion material (SM490.) We determined that previous studies did not provide sufficient explanations of the mechanism of breakaways. Therefore, this study is performed to clarify the conditions of post breakaway. The simulation was carried out using LS-DYNA and the TIEBREAK\_NODES\_ONLY option, which considers the failure force between the nodes at the post base. We assumed a full contact condition between the posts and calculated the vertical force over time after the impact under this initial condition. Then, with the maximum vertical force as the basis, eighteen cases are considered. The results show that the SS400 material has a higher breakaway requirement compared to that of SM490. Then this suggests that such difference is related to the physical properties of the steel material used for the post.

The assessment results of the passenger safety for THIV and PHD show that the requirement is satisfied under 40,000 N for both the SS400 and SM490 materials. However, in the case of SM490, while the post was not detached, both the THIV and PHD represent satisfactory results. In this study, we consider momentum to be a dominant factor for the failure and considered the vertical forces only. However, future studies that consider the shearing force as well could contribute to the enhancement of the results of the safety assessment. It will be also necessary to extend the concept from further studies for the wind resistance.

## Competing Interests

The author declares that there is no conflict of interests regarding the publication of this paper.

## Acknowledgments

This work was supported by the National Research Foundation of Korea (NRF) grant funded by the Korea government (MSIP) (no. 2015RIA2A2A01005637).

## References

- [1] G. R. Johnson and W. H. Cook, "Fracture characteristics of three metals subjected to various strains, strain rates, temperatures and pressures," *Engineering Fracture Mechanics*, vol. 21, no. 1, pp. 31–48, 1985.
- [2] M. G. Ko, K. D. Kim, K. J. Kim, J. G. Sung, and D. G. Yun, "Study on the hazardousness of a rigidly connected circular post and crash worthiness of a circular post with release mechanism for head-on impacts using impact simulation," *Journal of the Korean Society of Road Engineers*, vol. 12, no. 4, pp. 197–202, 2010.
- [3] W. Pawlus, K. G. Robbersmyr, and H. R. Karimi, "Mathematical modeling and parameters estimation of a car crash using data-based regressive model approach," *Applied Mathematical Modelling*, vol. 35, no. 10, pp. 5091–5107, 2011.
- [4] G.-D. Kim and S.-Y. Lee, "Finite element crash analysis of support structures made of various composite materials," *Journal of Korean Society for Advanced Composite Structures*, vol. 6, no. 1, pp. 45–50, 2015.
- [5] C. Liu, X. Song, and J. Wang, "Simulation analysis of car front collision based on LS-DYNA and hyper works," *Journal of Transportation Technologies*, vol. 4, pp. 337–342, 2014.
- [6] Y. Zhou, F. Lan, and J. Chen, "Crashworthiness research on S-shaped front rails made of steelaluminum hybrid materials," *Thin-Walled Structures*, vol. 49, no. 2, pp. 291–297, 2011.
- [7] Y. Zhang, G. Sun, G. Li, Z. Luo, and Q. Li, "Optimization of foam-filled bitubal structures for crashworthiness criteria," *Materials and Design*, vol. 38, pp. 99–109, 2012.
- [8] J. Choung, W. Nam, and J.-Y. Lee, "Dynamic hardening behaviors of various marine structural steels considering dependencies on strain rate and temperature," *Marine Structures*, vol. 32, pp. 49–67, 2013.
- [9] G. Cowper and P. Symonds, "Strain hardening and strain rate effects in the loading of cantilever beams," Brown University Applied Mathematics Report 28, 1957.
- [10] M. A. Crisfield, *Nonlinear Finite Element Analysis of Solids and Structures*, John Wiley & Sons, 1997.
- [11] AASHTO, *Manual for Assessing Safety Hardware*, AASHTO, 2009.

- [12] ANSYS Corp, *ANSYS(LS-DYNA) User's Manual*, ANSYS Corp, 2012.
- [13] J. E. Bowels, *Foundation Analysis and Design*, McGraw-Hill, New York, NY, USA, 2nd edition, 1977.
- [14] National Crash Analysis Center (NCAC), 2000, <http://www.ncac.gwu.edu/ncac/>.
- [15] Test Risk Assessment Program (TRAP) Version 2.0 User's Manual, 1999.
- [16] Ministry of Land, Infrastructure and Transport (MLIT), *Guideline to Perform Crash Tests for Road Side Barriers*, 2012 (Korean).

## Research Article

# Damage Detection of Structures for Ambient Loading Based on Cross Correlation Function Amplitude and SVM

Lin-sheng Huo,<sup>1</sup> Xu Li,<sup>1</sup> Yeong-Bin Yang,<sup>2</sup> and Hong-Nan Li<sup>1</sup>

<sup>1</sup>Key Laboratory of Coastal and Offshore Engineering, Dalian University of Technology, Dalian 116024, China

<sup>2</sup>Department of Civil Engineering, National Taiwan University, Taipei, Taiwan

Correspondence should be addressed to Lin-sheng Huo; [lshuo@dlut.edu.cn](mailto:lshuo@dlut.edu.cn)

Received 17 November 2015; Accepted 1 March 2016

Academic Editor: Abdollah Shafieezadeh

Copyright © 2016 Lin-sheng Huo et al. This is an open access article distributed under the Creative Commons Attribution License, which permits unrestricted use, distribution, and reproduction in any medium, provided the original work is properly cited.

An effective method for the damage detection of skeletal structures which combines the cross correlation function amplitude (CCFA) with the support vector machine (SVM) is presented in this paper. The proposed method consists of two stages. Firstly, the data features are extracted from the CCFA, which, calculated from dynamic responses and as a representation of the modal shapes of the structure, changes when damage occurs on the structure. The data features are then input into the SVM with the one-against-one (OAO) algorithm to classify the damage status of the structure. The simulation data of IASC-ASCE benchmark model and a vibration experiment of truss structure are adopted to verify the feasibility of proposed method. The results show that the proposed method is suitable for the damage identification of skeletal structures with the limited sensors subjected to ambient excitation. As the CCFA based data features are sensitive to damage, the proposed method demonstrates its reliability in the diagnosis of structures with damage, especially for those with minor damage. In addition, the proposed method shows better noise robustness and is more suitable for noisy environments.

## 1. Introduction

Structural damage detection is crucial in reducing catastrophic failures and prolonging the service life of structures. One of the most popular global structural damage detection techniques is the vibration-based damage detection technique, which has received considerable attention in recent years. The vibration-based damage detection methods can be classified as the model-based damage detection method (MBDDM) and non-model-based damage detection method (NMBDDM) [1, 2]. For the model-based method, the structural model is a function of the physical properties of the structure (mass, damping, and stiffness); hence model updating techniques are needed to improve the precision of the parameters describing the structure. As most model updating techniques are complicated and their precisions are limited for complex structures, the non-model-based method, which can avoid the drawbacks of the model-based method, is considered as a better choice in general. It can be easily implemented in online Structural Health Monitoring (SHM) systems for its simple computing process.

For the NMBDDM, a precise analytical model of the structure is not required, and the damage features can be extracted from the modal parameters or dynamic responses [2]. As a huge amount of damage information can be extracted from the modal parameters, some damage features can be detected based on the changes of natural frequencies or mode shapes [3]. However, modal parameters such as the mode shapes cannot be identified precisely for complex structures, which may reduce the accuracy of the NMBDDM. Therefore, some scholars have proposed the extraction of damage features directly from the dynamic response in time domain, frequency domain, or time-frequency domain. In their researches, statistical analysis technologies including the outlier analysis [4] and independent component analysis (ICA) [5] and signal process technologies including the wavelet transform technology (WPT) [6, 7] and Hilbert Huang transform (HHT) [8, 9] have been adopted to extract damage features from the dynamic response.

Almost all of the NMBDDM mentioned above can be used only to identify the presence of damage. Yang and

coworkers [2, 10–12] proposed a type of NMBDDM, which can be used to detect and locate damage with the correlation and relative difference between the cross correlative function amplitude vectors obtained from the intact and damaged structures. However, this method seems to have its limitation. Firstly, it is valid only for the case under steady random excitation within the specific frequency spectrum. Further, it requires the number of sensors nearly equal to that of the detectable damage locations of the structure, which means that the method may be impractical due to the high cost of the installation sensors.

It is known that the damage information provided by the damage features of the NMBDDM is generally insufficient and the locations and degree of damage are incapable of identification in full [1, 2]. Some scholars have introduced the intelligence algorithms to the NMBDDM methods, such as the artificial neural network (ANN) [13, 14] for their excellent pattern recognition capability. In this connection, the damage features are used as input data, and the intelligence algorithms are introduced as the analysis tools for matching the damage patterns, detecting the damage locations, and estimating the degree of severity.

The support vector machine (SVM) is another computational method based on the statistical learning theory, of which the classification ability can be applied in damage diagnosis of structures. Compared with ANN, the SVM can be used to achieve the same global optimal solution for a smaller number of samples for its better generalization [15]. The process of damage diagnosis utilizing the SVM consists of two steps: (1) features extraction from the measured dynamic responses and (2) patterns classification based on the input vectors composed of features. The SVM allows us to recognize and classify the structural damage patterns in a way as accurate as possible. The accuracy of the SVM lies mainly in the kernel function and the damage features. Improving the kernel function such as the wavelet packet kernel function [16, 17] can help improve the generalization ability. The selecting of damage features should be such proper as to contain the characteristics of the structure as fully as possible. The desired damage features are sensitive to the damage and independent variables that may not be easily interfered by external factors such as excitation and noise. Previously, the data features have been extracted from the structural modal parameters [18–20], independent component analysis (ICA) [21], envelope spectrum [22, 23], wavelet packet transform (WPT) energy spectrum [24, 25], and other statistical information [26]. Most of these data features have been proposed for the monitoring of mechanical devices, and few of them can be applied to the damage diagnosis of large and complex civil engineering structures.

The objective herein is to propose a new method that integrates the cross correlation function amplitude (CCFA) with the support vector machine (SVM) for the damage identification of skeletal structures. The proposed method can be used to locate damage and identify damage patterns with the limited number of sensors. This paper is organized as follows. Firstly, the cross correlation function amplitude and support vector machine are introduced in Sections 2 and 3, respectively. In Section 4, the damage detection method

for civil engineering structures based on the CCFA and SVM is illustrated in detail. In addition, the simulation data of IASC-ASCE benchmark simulation model and a vibration experiment of truss structure are used to illustrate the feasibility of proposed method in Sections 5 and 6.

## 2. Cross Correlation Function Amplitude (CCFA)

The cross correlation function  $R_{x,y}(T)$  of two stationary stochastic processes  $x(t)$  and  $y(t)$  with a time lag  $T$  is defined as

$$R_{x,y}(T) = E[x(t)y(t+T)], \quad (1)$$

where  $E[\cdot]$  is the expectation of the stochastic variable.

The equation of motion for  $N$  degree-of-freedom (DOF) structure with classical damping is

$$\mathbf{M}\ddot{\mathbf{X}}(t) + \mathbf{C}\dot{\mathbf{X}}(t) + \mathbf{K}\mathbf{X}(t) = \mathbf{F}(t), \quad (2)$$

where  $\mathbf{X}(t)$  is the  $N$ -dimensional displacement vector,  $\mathbf{F}(t)$  is the excitation vector, and  $\mathbf{M}$ ,  $\mathbf{C}$ , and  $\mathbf{K}$  denote, respectively, the mass, damping, and stiffness matrices of the structure with the dimension of  $N \times N$ . The displacement response can be decomposed into the  $N$  modal coordinates as

$$\mathbf{X}(t) = \sum_{n=1}^N \Phi^n Y^n(t) \quad (3)$$

in which  $\Phi^n$  is the  $n$ th modal vector and  $Y^n(t)$  is the corresponding modal coordinate. The  $n$ th modal response can be separately written as

$$\mathbf{X}^n(t) = \Phi^n Y^n(t). \quad (4)$$

By Duhamel's integral, the  $n$ th modal response at point  $i$  due to excitation  $f_k(t)$  at point  $k$  is

$$X_i^n(t) = \phi_i^n \phi_k^n \int_{-\infty}^t f_k(\tau) g^n(t-\tau) d\tau, \quad (5)$$

where

$$g^n(t-\tau) = \frac{\sin \omega_{Dn}(t-\tau) \exp[-\xi_n \omega_n(t-\tau)]}{m_n \omega_{Dn}}; \quad (6)$$

$m_n$ ,  $\xi_n$ , and  $\omega_n$  are the modal mass, modal damping ratio, and natural frequency of the  $n$ th mode, respectively; and  $\omega_{Dn} = \omega_n \sqrt{1 - \xi_n^2}$  is the damped natural frequency of the  $n$ th mode. For ambient loading, the exciting points are numerous, and  $X_i^n(t)$  is the accumulation of responses caused by each exciting point as follows:

$$X_i^n(t) = \phi_i^n \int_{-\infty}^t \sum \phi_k^n f_k(\tau) g^n(t-\tau) d\tau. \quad (7)$$

Based on the natural excitation technique (NExT) [27], the cross correlation function between the  $n$ th modal responses at the  $i$ th and  $j$ th points can be written as

$$R_{x_i, x_j}^n(T) = \phi_i^n \phi_j^n \int_{-\infty}^t \int_{-\infty}^{t+T} g^n(t-\tau) g^n(t+T-\sigma) \cdot \sum \sum \phi_k^n \phi_k^n E\{f_k(\tau) f_k(\sigma)\} d\sigma d\tau. \quad (8)$$

If the ambient vibration source is a white noise random process, then

$$E \{f_k(\tau) f_k(\sigma)\} = \alpha_k \delta(\tau - \sigma), \quad (9)$$

where  $2\alpha_k$  is a constant representing the one-side autospectral density of the white noise and  $\delta(t)$  is the Dirac delta function. Substituting (7) and (9) into (8), one can express the cross correlation function of the  $n$ th modal displacement responses at the  $i$ th and  $j$ th point as follows:

$$R_{x_i, x_j}^n(T) = \frac{\phi_i^n G_j^n}{m_n \omega_{Dn}} \exp(-\xi_n \omega_n T) \sin(\omega_{Dn} T + \varphi_n), \quad (10)$$

where  $G_j^n$  is the coefficient depending on  $n$ th modal parameters, exciting points, and measured response at point  $j$  and  $\varphi_n$  is a phase dependent on the  $n$ th modal parameters. Since the structural responses under the white noise excitation are stationary stochastic processes, the cross correlation function of the  $n$ th modal velocity responses at the  $i$ th and  $j$ th points can be written as

$$\begin{aligned} R_{\dot{x}_i, \dot{x}_j}^n(T) &= -R_{x_i, x_j}^n{}'(T) = \frac{\phi_i^n G_j^n}{m_n \omega_{Dn}} \exp(-\xi_n \omega_n T) \\ &\cdot \left[ (\omega_{Dn}^2 - \xi_n^2 \omega_n^2) \sin(\omega_{Dn} T + \varphi_n) \right. \\ &\left. + 2\xi_n \omega_n \omega_{Dn} \cos(\omega_{Dn} T + \varphi_n) \right]. \end{aligned} \quad (11)$$

Also, the cross correlation function of the  $n$ th modal acceleration responses at the  $i$ th and  $j$ th points can be expressed as

$$\begin{aligned} R_{\ddot{x}_i, \ddot{x}_j}^n(T) &= R_{x_i, x_j}^n{}''(T) = \frac{\phi_i^n G_j^n}{m_n \omega_{Dn}} \exp(-\xi_n \omega_n T) \\ &\cdot \left[ (\omega_n^4 - 6\xi_n^2 \omega_n^2 \omega_{Dn}^2 + \omega_{Dn}^4) \sin(\omega_{Dn} T + \varphi_n) \right. \\ &\left. + (4\xi_n \omega_n \omega_{Dn}^3 + 4\xi_n^3 \omega_n^3 \omega_{Dn}) \cos(\omega_{Dn} T + \varphi_n) \right]. \end{aligned} \quad (12)$$

Consequently, the cross correlation function amplitudes (CCFAs) of the  $n$ th modal displacement, velocity, and acceleration responses are

$$\begin{aligned} \max [R_{i,j}^n(T)] &= \frac{G_j^n}{m_n \omega_{Dn}} \\ &\cdot \frac{a(a\omega_{Dn} - b\xi_n \omega_n) + b(a\xi_n \omega_n + b\omega_{Dn})}{\sqrt{(a\omega_{Dn} - b\xi_n \omega_n)^2 + (a\xi_n \omega_n + b\omega_{Dn})^2}} \\ &\cdot \exp(-\xi_n \omega_n T^*) \phi_i^n, \end{aligned} \quad (13)$$

where

$$T^* = \arcsin \frac{a(a\omega_{Dn} - b\xi_n \omega_n)}{\sqrt{(a\omega_{Dn} - b\xi_n \omega_n)^2 + (a\xi_n \omega_n + b\omega_{Dn})^2}}. \quad (14)$$

The values of  $a$  and  $b$  have been listed in Table 1.

TABLE 1: Values of  $a$  and  $b$  for the CCFA of  $n$ th modal displacement, velocity, and acceleration responses.

$R_{i,j}^n(T)$	$a$	$b$
$R_{x_i, x_j}^n(T)$	1	0
$R_{\dot{x}_i, \dot{x}_j}^n(T)$	$\omega_{Dn}^2 - \xi_n^2 \omega_n^2$	$2\xi_n \omega_n \omega_{Dn}$
$R_{\ddot{x}_i, \ddot{x}_j}^n(T)$	$\omega_n^4 - 6\xi_n^2 \omega_n^2 \omega_{Dn}^2 + \omega_{Dn}^4$	$4\xi_n \omega_n \omega_{Dn}^3 + 4\xi_n^3 \omega_n^3 \omega_{Dn}$

Define intermediate variable  $\kappa^*(\xi_n, \omega_n)$  as

$$\begin{aligned} \kappa^*(\xi_n, \omega_n) &= \frac{a(a\omega_{Dn} - b\xi_n \omega_n) + b(a\xi_n \omega_n + b\omega_{Dn})}{\sqrt{(a\omega_{Dn} - b\xi_n \omega_n)^2 + (a\xi_n \omega_n + b\omega_{Dn})^2}} \\ &\cdot \exp(-\xi_n \omega_n T^*). \end{aligned} \quad (15)$$

The point  $j$  is taken as a reference point, and the CCFA of the  $n$ th modal signals between point  $j$  and other points are calculated with their CCFA listed as a vector,

$$\begin{aligned} \mathbf{V}_{\text{CCFA}} &= [\max(R_{1,j}^n) \quad \max(R_{2,j}^n) \quad \cdots \quad \max(R_{N,j}^n)] \\ &= \frac{G_j^n \kappa^*(\xi_n, \omega_n)}{m_n \omega_{Dn}} [\phi_1 \quad \phi_2 \quad \cdots \quad \phi_N]. \end{aligned} \quad (16)$$

$\mathbf{V}_{\text{CCFA}}$ , which can be calculated from the displacement, velocity, or acceleration response, is closely related to the  $n$ th modal shape. When damage occurs, the modal shape close to the damaged location will be changed, and the damage feature  $\mathbf{D}_{\text{CCFA}}$  is defined as the difference in  $\mathbf{V}_{\text{CCFA}}$  between the intact and current conditions as

$$\mathbf{D}_{\text{CCFA}} = \mathbf{V}_{\text{CCFA}}^{\text{intact}} - \mathbf{V}_{\text{CCFA}}^{\text{current}}, \quad (17)$$

where the superscripts ‘‘intact’’ and ‘‘current’’ stand for  $\mathbf{V}_{\text{CCFA}}$  at the intact and current conditions, respectively.

### 3. Support Vector Machine (SVM)

The support vector machine is a recently developed statistical learning algorithm based on the structural risk minimization (SRM) principle. The basic SVM deals with binary classification problems. The main idea of the SVM is to transform the data to a higher dimensional features space and to find the optimal hyperplane in the space that maximizes the margin between the two classes as shown in Figure 1. Consider a set of training data  $\{(x_i, y_i), i = 1, 2, \dots, l\}$ ,  $x_i$  is the vector of input variables, and  $y_i$  is the target vector corresponding to  $\{-1, 1\}$  in binary classification problem.

For the case of linear data, the separating hyperplane can be defined by

$$f(x) = \mathbf{w}^T \mathbf{x} + b = 0, \quad (18)$$

where  $f(x)$  is the separating hyperplane and the vectors  $\mathbf{w}$  and  $b$  are the weight factors defining the position of the separating hyperplane. The decision function is given by (19),

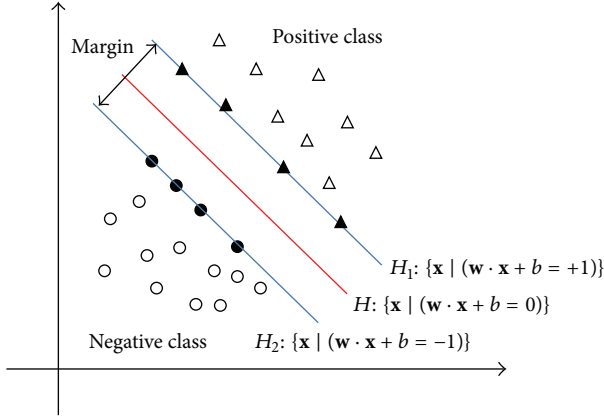


FIGURE 1: The diagram of SVM.

with which the input data are classified into either positive or negative class

$$\tilde{f}(x) = \text{sign}[f(x)]. \quad (19)$$

Taking into account the noise with slack variables  $\zeta_i$  and the error penalty  $C$ , the optimal hyperplane separating the data can be obtained by minimizing  $\|\mathbf{w}\|$ , leading to the following constrained optimization problem:

$$\begin{aligned} \min_{\omega, b, \zeta_i} \quad & \frac{1}{2} \mathbf{w}^T \mathbf{w} + C \sum_{i=1}^l \zeta_i \\ \text{subject to} \quad & y_i (\mathbf{w}^T \cdot x_i + b) \geq 1 - \zeta_i \\ & \zeta_i \geq 0, \quad i = 1, \dots, l. \end{aligned} \quad (20)$$

Introducing the Lagrangian multiplier  $\alpha_i \geq 0$ , the above problem can be transformed to the following form:

$$\begin{aligned} \text{maximize} \quad & L(\mathbf{w}, b, \alpha) = \sum_{i=1}^l \alpha_i - \frac{1}{2} \sum_{i,j=0}^l \alpha_i \alpha_j y_i y_j x_i \cdot x_j \\ \text{subject to} \quad & \alpha_i \geq 0, \\ & i = 1, \dots, M, \\ & \sum_{i=1}^M \alpha_i y_i = 0. \end{aligned} \quad (21)$$

The linear SVM algorithm derived above can be easily extended to the nonlinear regression analysis by kernel methods. Using the nonlinear vector function  $\Psi(\mathbf{x}) = (\psi_1(x), \dots, \psi_M(x))$  to map the  $n$ -dimensional input vector  $\mathbf{x}$  onto the  $l$ -dimensional features space, the linear decision function in dual form is given by

$$\tilde{f}(x) = \text{sign} \left( \sum_{i,j=1}^M \alpha_i y_i (\Psi^T(x_i) \cdot \Psi(x_j)) + b \right). \quad (22)$$

The kernel function  $K(x_i, x_j) = (\Psi^T(x_i) \cdot \Psi(x_j))$  is applied to simplifying of the calculation, by which, the learning in the

TABLE 2: The commonly used kernel functions.

Linear	$K(x_i, x_j) = x_i \cdot x_j$
Polynomial	$K(x_i, x_j) = (x_i \cdot x_j + c)^d$
Radial Basis Function (RBF)	$K(x_i, x_j) = \exp(-\gamma \ x_i - x_j\ ^2)$
Sigmoidal kernel function (SKF)	$K(x_i, x_j) = \tanh(\gamma \ x_i - x_j\ ^2)$

features space does not require explicit evaluation of  $\Psi$  and the decision function will be

$$\tilde{f}(x) = \text{sign} \left( \sum_{i,j=1}^M \alpha_i y_i K(x_i, x_j) + b \right). \quad (23)$$

Any function that satisfies Mercer's theorem can be used as a kernel function. The selection of kernel function is important to SVM, because the kernel function decides the future spaces that the samples will be mapped into. The commonly used kernel functions include the linear, polynomial, Gaussian Radial Basis Function (RBF), and sigmoidal kernel function (SKF), as listed in Table 2.

The fundamental capability of the SVM discussed above deals with binary classification. In practice, however, the method can be extended to solve multiclassification problems as well. One typical multiclassification method is called the one-against-one (OAO) algorithm [15, 28]. This method uses  $k(k-1)/2$  binary classifiers to identify  $k$  classes. Each training data piece is divided into two classes. For training data from the  $i$ th and the  $j$ th classes, the binary classification problem is shown as (24). If  $x$  is in the  $i$ th class, then the vote for the  $i$ th class is added by one; otherwise,  $j$ th is increased by one. When classifying test data, all of the SVMs perform classification and the test data is identified as the class with the largest number of votes. The schematic diagram of OAO algorithm is shown in Figure 2. Consider

$$\text{minimize} \quad \frac{1}{2} \|\mathbf{w}^{ij}\|^2 + C \sum_t \zeta_t^{ij} (\mathbf{w}^{ij})^T, \quad (24)$$

$$\text{subject to} \quad (\mathbf{w}^{ij})^T \phi(x_t) + b^{ij} \leq 1 - \zeta_t^{ij} \quad \text{if } y_t = i,$$

$$(\mathbf{w}^{ij})^T \phi(x_t) + b^{ij} \leq -1 + \zeta_t^{ij} \quad \text{if } y_t = j, \quad (25)$$

$$\zeta_t^{ij} \geq 0, \quad j = 1, \dots, L.$$

#### 4. Damage Detection Based on CCFA and SVM

In this paper,  $\mathbf{D}_{\text{CCFA}}$  is taken as the damage features for the input data vector, and the damage pattern can be classified by the multiclass SVM. There are two main advantages with the proposed data features. First, as revealed by (16),  $\mathbf{V}_{\text{CCFA}}$  is a stable variable closely related to the structural modal shapes. Therefore, the accuracy of the method can hardly be interfered by external factors such as ambient excitation. In addition, because the relative change in the structural modal shape is sensitive to the damage, the difference of  $\mathbf{V}_{\text{CCFA}}$  between the intact and current conditions is sensitive to minor damage with small stiffness changes.

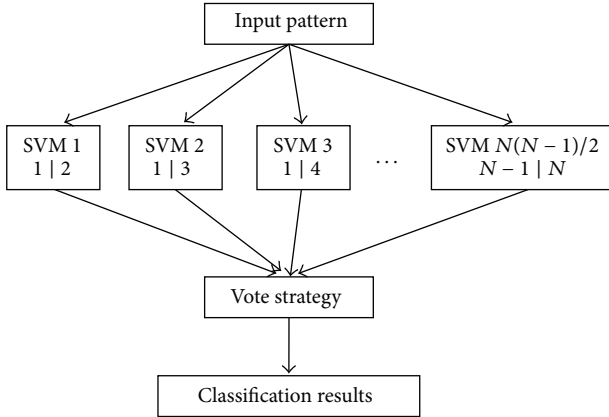


FIGURE 2: Schematic of OAO algorithm.

The procedure of the proposed method, as shown in Figure 3, can be summarized as follows.

$$\mathbf{V}_{\text{CCFA}} = [\max(R_{1,i}^n) \max(R_{2,i}^n) \cdots \max(R_{N,i}^n) \max(R_{1,j}^n) \max(R_{2,j}^n) \cdots \max(R_{N,j}^n)]. \quad (26)$$

(3) Calculate the data features, which are acquired from the difference of  $\mathbf{V}_{\text{CCFA}}$  between the intact and current conditions according to (17). Then, the training data are established with  $N^* \times M$  samples.

(4) The data features serve as the training data for input to the SVM and the classifiers are trained.

(5) Collect the test signals of the structure, and calculate the test samples with the same process from step (1) to step (4) as input data to the trained SVM classifiers. Then the structure status can be identified by the output of the SVM classifiers.

## 5. Numerical Verification

The simulation data of phase I IASC-ASCE benchmark model [32] is used to verify the feasibility of the method proposed in this paper. The sketch of the analytical model and the sensor locations is shown in Figure 4. In this paper, the symmetrical structure is simulated by a 12-DOF model, with each floor represented by 3 DOFs, including two translations and one rotation. The Gaussian white noise acceleration is loaded at all stories which can be represented as ambient excitation. The damage patterns are listed in Table 3, in which pattern 0 is the intact, undamaged one, patterns 1 and 2 represent major damage patterns, and patterns 3 to 5 are minor damage patterns. Table 4 lists the percentage loss in the horizontal story stiffness of the damaged 12-DOF model for each pattern. As can be seen, patterns 1 and 2 represent major damage. The inclusion of patterns 3–5 is to test the ability of the proposed approach in detecting minor damage. In addition, pattern 3 is similar to pattern 4, while pattern 0 is similar to pattern 5.

(1) Assume that there are  $M$  ordinary types of circumstances with the label of  $1, \dots, M$ , respectively, in which 1 represents the intact condition and  $2, \dots, M$ , respectively, stand for different damage patterns. Sample  $N^*$  times of the dynamic response for each circumstance from  $L$  sites of measurement, and take  $N^* \times M \times L$  signals as samples.

(2) Extract the  $n$ th approximate modal response via some signal processing technologies such as WPT and EMD, by which, the dynamic responses can be decomposed, and then, the approximate modal responses can be acquired by reconstructing the decomposed signals containing modal frequencies [29–31]. Then choose a special site, which is a node of mode insensitive to the damage, as the reference point for calculating  $\mathbf{V}_{\text{CCFA}}$  based on (16) with the dimension of  $1 \times L$ . Or two reference points can be selected to ensure that the performance of identification is not affected by the reference point if one reference is sensitive to the damage. Then  $\mathbf{V}_{\text{CCFA}}$  can be expressed as

The acceleration responses are calculated by the MATLAB program for the phase I benchmark model. There are 40 samples for the undamaged pattern and 20 samples for each damage pattern, respectively. Firstly, the first four approximate modal responses are extracted by the WPT technique. Figure 5 shows the original signal and first four modal acceleration responses at point 1, and the FFT spectrum of each signal is shown in Figure 6. From Figure 6, one observes that the amplitudes of the first two frequencies in the original response are, respectively, equal to those in each approximate modal response, which can confirm the validity of the first two modal signals extracted by WPT technique.

Then, point 1 is taken as the reference point, and the value of  $\mathbf{V}_{\text{CCFA}}$  is calculated using (15) from the first approximate modal responses. Twenty values of  $\mathbf{V}_{\text{CCFA}}$  of pattern 0 are taken as the intact condition, and other values of  $\mathbf{V}_{\text{CCFA}}$ , containing twenty samples of pattern 0 and other five damage patterns, are taken as the current condition. Note that the cross correlation is a normalized sequence ranged from 0 to 1 which is calculated by MATLAB software, and the detailed principle can be found in [33]. The data features are defined by the difference of CCFA between the current and intact conditions. So there are 120 samples of data features for six patterns, and each pattern has 20 samples. Half of the samples in each pattern are used as the training data, while the others are used as the test data of the SVM. The training label of 1–6 represents pattern 0, pattern 1, ..., pattern 5, subsequently. The multiclass classification system for the fault diagnostics with the one-against-one SVM is then established.

In this paper, the commonly used kernel functions including polynomial, RBF, and SKF are used to verify the

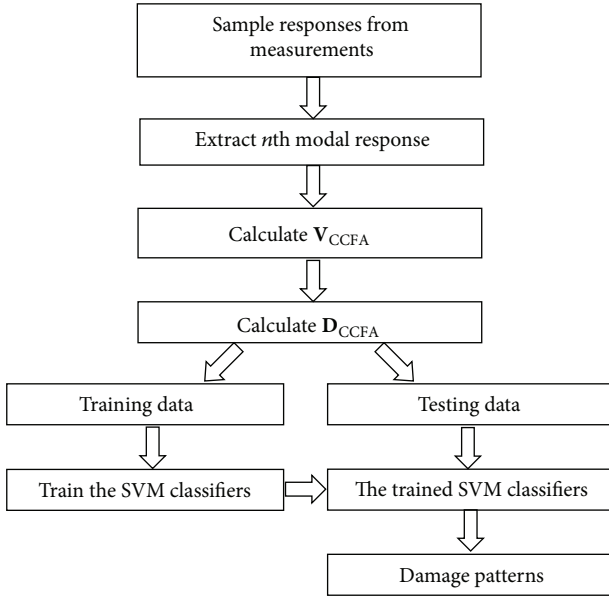


FIGURE 3: Overall procedure of proposed method.

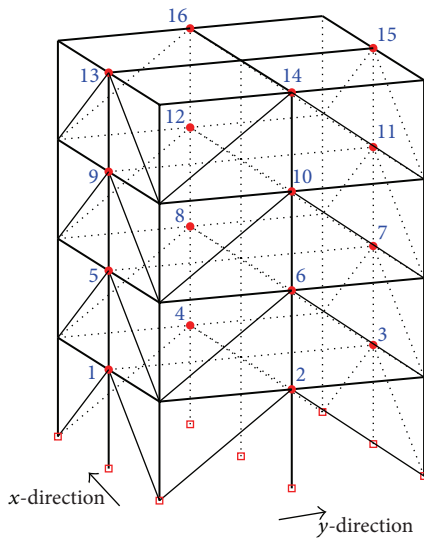


FIGURE 4: The sketch of the analytical model and the sensor locations.

superiority of CCFA based multiclass SVM. The SVM parameters play a crucial role in the performance of classification. There are two parameters for these kernel functions:  $C$  and  $\gamma$ . In addition, the polynomial kernel function also has a parameter  $d$ , which means the degree of the polynomial. An improper choice of the parameters can cause the overfitting or underfitting problem. Therefore, the procedure of searching optimal parameters using training data is indispensable before model training. An exhaustive grid-search with exponentially growing  $C$  and  $\gamma$  is conducted to obtain the optimal choice of  $C$  and  $\gamma$  with the strategy of  $\nu$ -fold cross-validation [34]. In addition, the LIBSVM toolbox [35] is used for the procedure of the SVM.

TABLE 3: Damage patterns.

Damage pattern	Description
Pattern 0	Undamaged case
Pattern 1	All braces of 1st story are broken
Pattern 2	All braces of 1st and 3rd stories are broken
Pattern 3	1 brace on one side of 1st story is broken
Pattern 4	1 brace on one side of 1st and 3rd stories is broken
Pattern 5	Area of 1 brace on one side of 1st story is reduced to 2/3

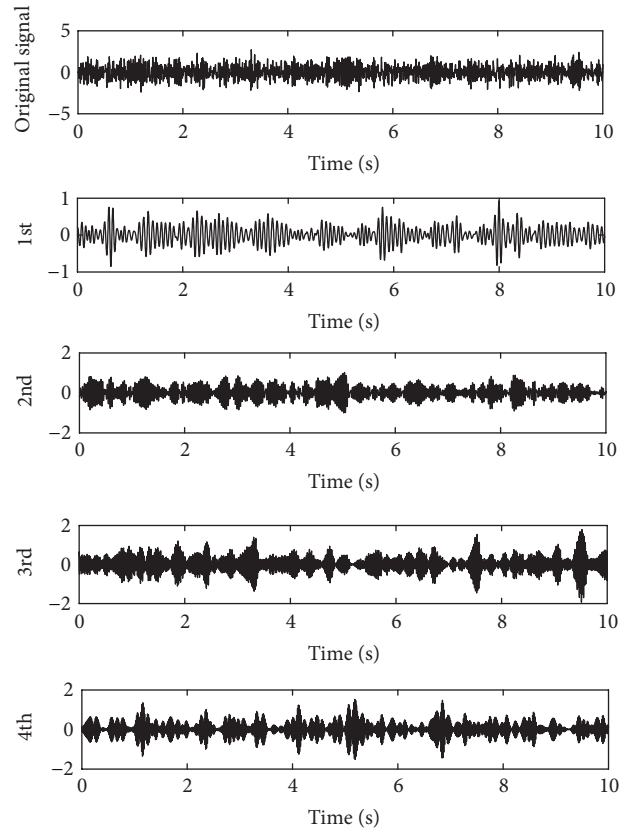


FIGURE 5: Original signal and first four approximate modal responses at point 1.

Figure 7 shows the distribution of the  $\nu$ -fold cross validation (CV) accuracy for different kernel functions.  $C$  and  $\gamma$  are ranged from  $2^{-10}$  to  $2^{10}$  exponentially, and  $\nu$  is equal to 5. From Figure 7 the optimal combinations of  $C$  and  $\gamma$ , which are those with the highest CV accuracy, are acquired.

In Table 5, the classification results of the testing samples are listed, in which  $n/m$  means that there are  $n$  valid identifications from  $m$  samples. It can be seen that the SVM classifiers with the one-against-one algorithm can recognize the fault types effectively, especially with the kernel function of RBF.

TABLE 4: Percentage losses in horizontal and rotational stiffness for each pattern.

Element		Damage pattern				
Story	DOF	1	2	3	4	5
1	$x$	45.24%	45.24%	0	0	0
1	$y$	71.03%	71.03%	17.76%	17.76%	5.92%
1	$\theta$	64.96%	64.96%	9.87%	9.87%	2.88%
2	$x$	0	0	0	0	0
2	$y$	0	0	0	0	0
2	$\theta$	0	0	0	0	0
3	$x$	0	45.24%	0	11.31%	0
3	$y$	0	71.03%	0	0	0
3	$\theta$	0	64.96%	0	9.16%	0
4	$x$	0	0	0	0	0
4	$y$	0	0	0	0	0
4	$\theta$	0	0	0	0	0

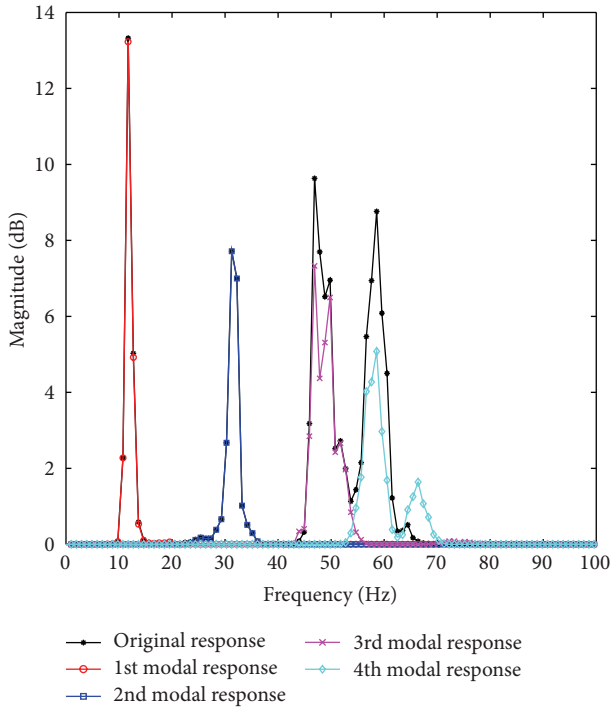


FIGURE 6: FFT spectrum of original signal and first 4 approximate modal responses.

The signals' energy is often used to measure the damage for civil engineering structures. The WPT energy spectrum and EMD energy spectrum are the classical damage features to depict the distributions of signals' energy [24, 36]. Meanwhile, the artificial neural network (ANN) is a classical intelligent algorithm which is used to pattern classification. To show the performance of the SVM classification scheme based on the CCFA features, a comparison is made between the proposed method, SVM classifications with other damage features including WPT energy spectrum and EMD energy

spectrum, and ANN classification with CCFA features. The test accuracy rate of different method is shown in Figure 8, where WPT + SVM, EMD + SVM, and CCFA + SVM mean that the data features are extracted from the WPT spectrum, EMD spectrum, and CCFA, respectively. And CCFA + ANN means the ANN classification with CCFA features.

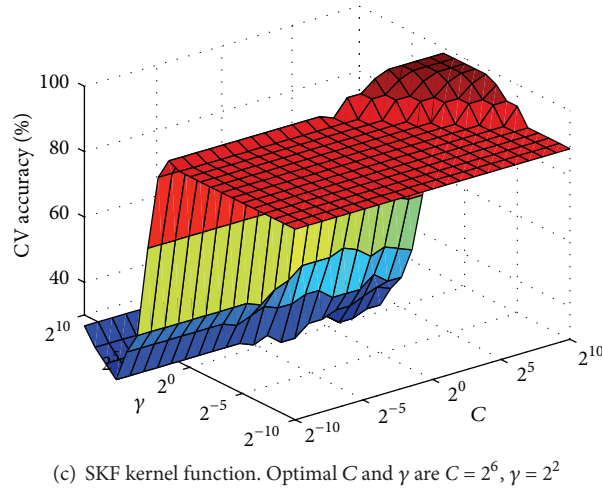
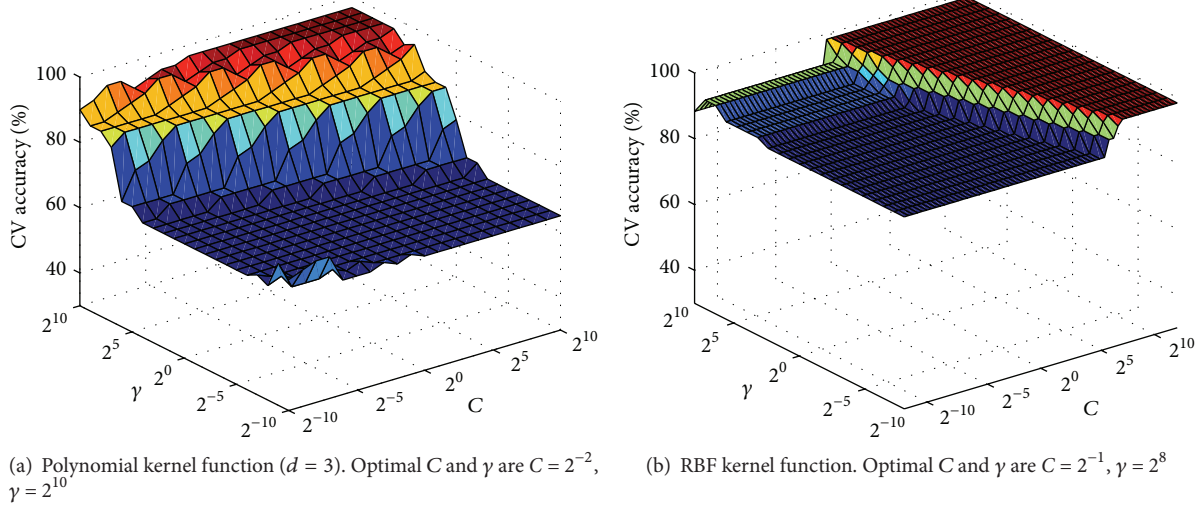
It can be seen that all methods can be used to identify major damage such as pattern 1 and pattern 2. However, the proposed method has the best classification performance for patterns 3, 4, and 5, as a manifestation of minor damage of the benchmark model. Consequently, the superiority of the CCFA features based SVM has been demonstrated especially for the scenarios of minor damage with small stiffness changes.

The modal responses are extracted by signal process technologies. It is necessary to investigate the sensitivity of identification results to the veracity of extracting approximate modal response. To simulate the identification error, the approximate modal responses are modulated by adding noises with different levels. The identification results are shown in Figure 9, from which it can be seen that the average accuracy is still more than 90% when the approximate modal responses are mixed noise with a level of 20%.

To study the effect of sensor noise on classification efficiency, a series of random noises are added to the responses of the structure with a level of 0 to 50% before the data features are extracted. Figure 10 shows the average accuracies of identification for patterns 0 to 3 with different classification method mentioned above for different levels of noises. The results show that a high level of accuracy can still be achieved even for the noise level up to 50% when the data features are extracted based on CCFA. Compared with data features extracted by other data features, the CCFA features based SVM method has been demonstrated to be better in noise robustness and is more appropriate for application to noisy environment.

TABLE 5: The classification result of the testing samples.

Kernel function	Pattern 0	Pattern 1	Pattern 2	Pattern 3	Pattern 4	Pattern 5
Polynomial	10/10	10/10	9/10	10/10	9/10	9/10
KBF	10/10	10/10	10/10	10/10	10/10	10/10
SKF	10/10	10/10	10/10	10/10	8/10	9/10

FIGURE 7: CV accuracy with  $C$  and  $\gamma$  for polynomial, RBF, and SKF kernel functions, in the second loading condition.

## 6. Experimental Verification

A vibration experiment of truss structure is conducted to further verify the feasibility of proposed method with the limited number of sensors. The principal member of the structure is made by Q235 steel with the dimension of  $L 30 \times 4$ . The 300 kg weight stack is loaded on the top of the structure to guarantee the dynamical similarity. All members are connected by the bolts on the gusset plates. The experimental photo is shown in Figure 11. The loading devices are two JZK-20 vibration exciters, the matched signal generator and power amplifier. The dSPACE system is used as data acquisition system with the sample frequency of 500 Hz.

The arbitrary voltage signal is generated by signal generator, then amplified by the power amplifier, and transferred to the vibration exciter to generate excitation forces on the top of truss structures.

The PZT (Pb-Based Lanthanum Doped Zirconate Titanates) sensors are attached on the surface of principal beams to collect the strain response of the structure as shown in Figure 12. All sensors are arrayed on one side of the truss model. The distribution of sensors location is shown in Figure 13, in which b1–b13 are the number of members and s-1 to s-6 are the number of PZT sensors.

The bolt looseness in gusset plate is one of the most common damage kinds for truss structures. In this paper,

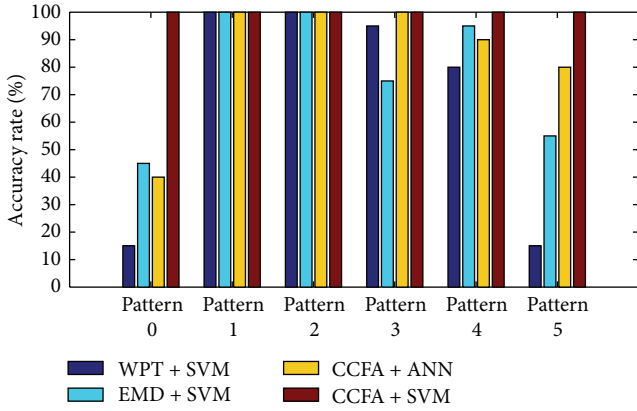


FIGURE 8: Test accuracy rate with different types of methods.

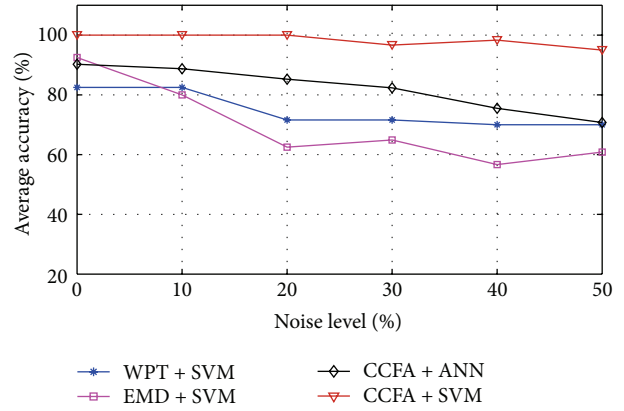


FIGURE 10: The average accuracies of identification with different level of noises.

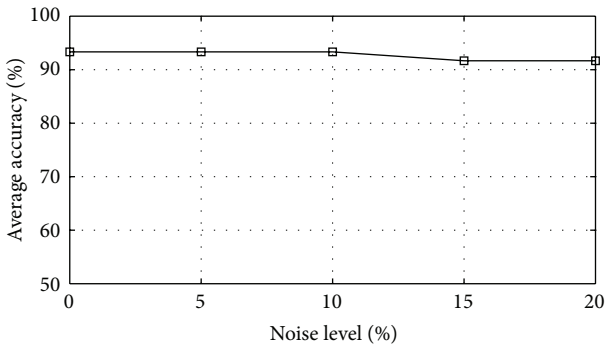


FIGURE 9: The identification results when the approximate modal responses are added with noises with different levels.

the bolts are loosened as the connecting damage in gusset plate. All the damage patterns are listed in Table 6. Note that no sensor is attached in b7, while the damage location in pattern 5 is far away from all sensors, which means that there is inadequate number of sensors distributed in the key locations. In addition, the damage patterns cannot be identified by natural frequencies.

The Gaussian white noise excitation with the frequency from 0 to 30 Hz and duration 20 s is loaded to the structure. 40 samples of PZT sensor responses in pattern 0 condition are acquired. 20 of them are used as initial samples, and the other are used as current undamaged samples. 20 samples in pattern 2-pattern 5 are collected as damaged samples.

The sensor s-6 is taken as reference point, and then  $V_{CCFA}$  and  $D_{CCFA}$  are calculated. Figure 14 shows the distribution of the  $\nu$ -fold cross-validation (CV) accuracy for different kernel functions, in which  $C$  and  $\gamma$  are ranged from  $2^{-10}$  to  $2^{10}$  exponentially, and  $\nu$  is equal to 5. Table 7 lists the classification accuracy of the truss structures for each damage pattern. It can be seen that the proposed method can identify the damage pattern in truss structure effectively with a limited number of sensors.

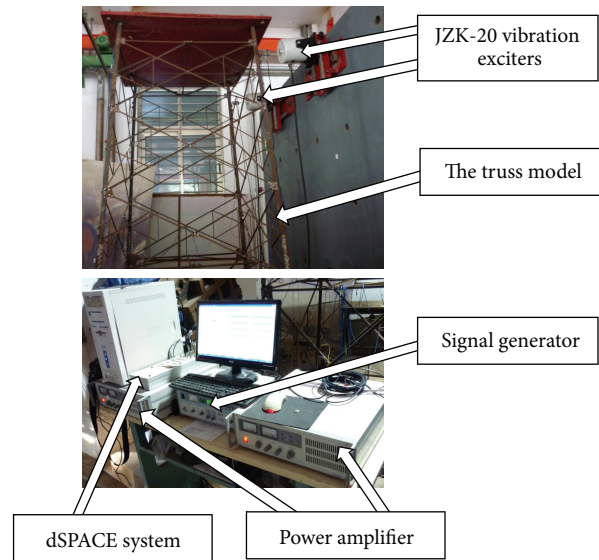


FIGURE 11: The experimental photo.



FIGURE 12: The PZT sensor.

TABLE 6: The damage patterns of truss structure.

Damage pattern	Description	Natural frequency
Pattern 0	Undamaged	20.51 Hz
Pattern 1	The bolts in the b5 connected b1, b3, and b7 are loosened	16.6 Hz
Pattern 2	The bolts in the joint connected b1, b3, and b7 are loosened	16.6 Hz
Pattern 3	The bolts in b1 connected with b3 are loosened	17.58 Hz
Pattern 4	The bolts in b7 connected with b1 and b3 are loosened	20.51 Hz
Pattern 5	A bottom column on the other side of structure is broken	20.51 Hz

TABLE 7: The accuracy of damage pattern classification with different kernel function.

Kernel function	Case 1	Case 2	Case 3	Case 4	Case 5	Case 6
Polynomial	100%	80%	100%	80%	70%	100%
RBF	100%	80%	100%	90%	90%	100%
SKF	100%	80%	100%	80%	80%	100%

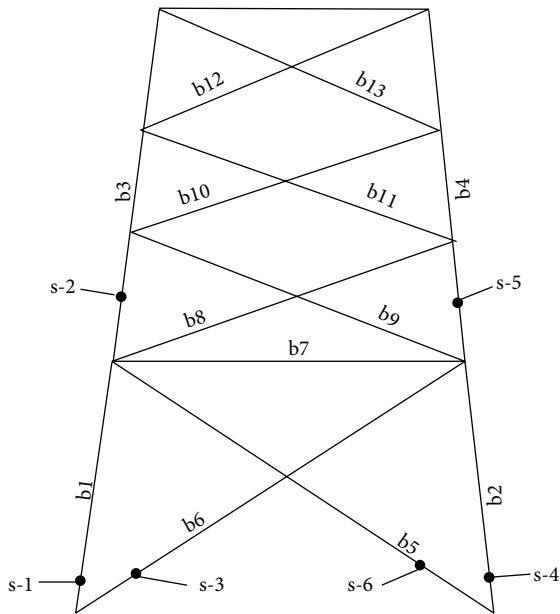


FIGURE 13: The distribution of PZT sensors.

## 7. Concluding Remarks

In this research, a damage detection approach integrating the cross correlation function amplitude (CCFA) with support vector machine (SVM) is proposed. The accuracy and stability of the SVM classification depend largely on the quality of input data features. The CCFA, closely related to the modal property of the structure, varies with the change in structural damage status. Therefore, the input data features can be extracted from the difference in CCFA between the current and intact conditions. This forms the basis for the proposed damage detection method that integrates the CCFA with SVM. The signal process technology such as the wavelet

packet transform (WPT) or empirical mode decomposition (EMD) is used to extract single  $n$ th approximate modal response of the dynamic response, by which the data feature based on the CCFA is extracted. Normally, the 1st and 2nd mode signals are used in the detection. Next, the data features are used as input into the SVM for the classification of structural damage.

The proposed approach has been verified by the simulation data of the IASC-ASCE benchmark model and a vibration experiment of truss model, by which the properties of the proposed method, along with the advantages, can be outlined as follows:

- (1) The CCFA features based SVM fault diagnosis approach shows excellent capability in damage classification and identification for the benchmark model and is suitable for the damage detection of engineering structures subjected to ambient excitation.
- (2) The proposed approach can be used to identify minor damage for the benchmark model. It is concluded that the damage detection approach based on the integrated use of the CCFA and SVM is more reliable for identifying minor damage with small stiffness changes, in comparison with other approaches analyzed herein.
- (3) The proposed method remains quite high in terms of accuracy for the benchmark model even if the noise level has been raised to 50%. This is a demonstration that the proposed method has better noise robustness and is more appropriate for application in noisy environments.
- (4) From the vibration experiment of truss model, it can be concluded that the proposed method is feasible for skeletal structures with a limited number of sensors.

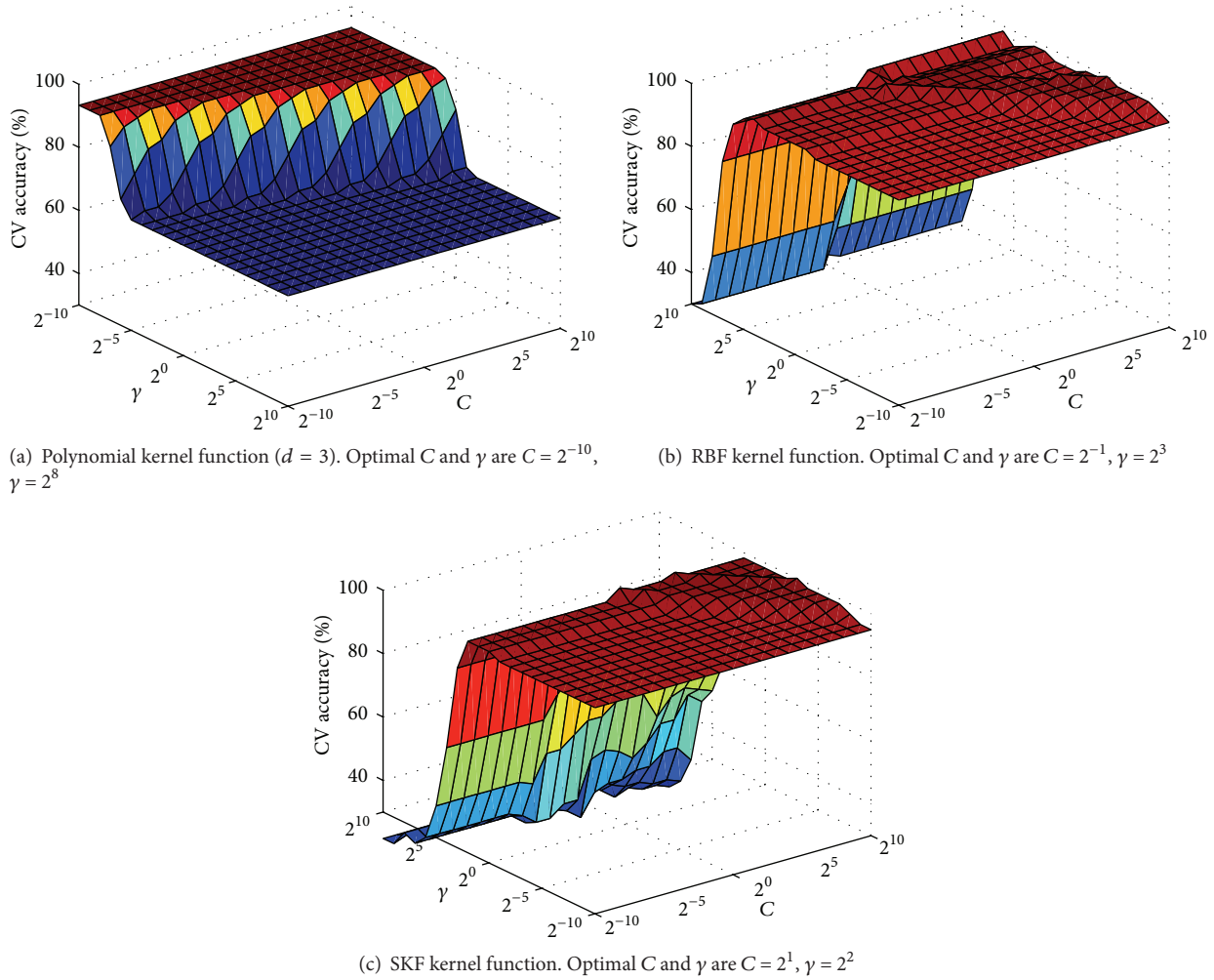


FIGURE 14: The CV accuracy with  $C$  and  $\gamma$  for polynomial, RBF, and SKF kernel functions.

## Competing Interests

The authors declare that they have no competing interests.

## Acknowledgments

The authors would like to appreciate the support from National Natural Science Foundation of China (Grant no. 51421064) and 973 Program of China (no. 2015CB057704).

## References

- [1] Y. J. Yan, L. Cheng, Z. Y. Wu, and L. H. Yam, "Development in vibration-based structural damage detection technique," *Mechanical Systems and Signal Processing*, vol. 21, no. 5, pp. 2198–2211, 2007.
- [2] Z. Yang, L. Wang, H. Wang, Y. Ding, and X. Dang, "Damage detection in composite structures using vibration response under stochastic excitation," *Journal of Sound and Vibration*, vol. 325, no. 4-5, pp. 755–768, 2009.
- [3] J.-T. Kim, Y.-S. Ryu, H.-M. Cho, and N. Stubbs, "Damage identification in beam-type structures: frequency-based method vs mode-shape-based method," *Engineering Structures*, vol. 25, no. 1, pp. 57–67, 2003.
- [4] K. Worden, G. Manson, and N. R. J. Fieller, "Damage detection using outlier analysis," *Journal of Sound and Vibration*, vol. 229, no. 3, pp. 647–667, 2000.
- [5] C. Zang, M. I. Friswell, and M. Imregun, "Structural damage detection using independent component analysis," *Structural Health Monitoring*, vol. 3, no. 1, pp. 69–83, 2004.
- [6] A. Hera and Z. Hou, "Application of wavelet approach for ASCE structural health monitoring benchmark studies," *Journal of Engineering Mechanics*, vol. 130, no. 1, pp. 96–104, 2004.
- [7] D. Cantero and B. Basu, "Railway infrastructure damage detection using wavelet transformed acceleration response of traversing vehicle," *Structural Control and Health Monitoring*, vol. 22, no. 1, pp. 62–70, 2015.
- [8] J.-P. Tang, D.-J. Chiou, C.-W. Chen et al., "RETRACTED: a case study of damage detection in benchmark buildings using a Hilbert-Huang Transform-based method," *Journal of Vibration and Control*, vol. 17, no. 4, pp. 623–636, 2011.
- [9] J. N. Yang, Y. Lei, S. Lin, and N. Huang, "Hilbert-Huang based approach for structural damage detection," *Journal of Engineering Mechanics*, vol. 130, no. 1, pp. 85–95, 2004.

- [10] Z. Yang, Z. Yu, and H. Sun, "On the cross correlation function amplitude vector and its application to structural damage detection," *Mechanical Systems and Signal Processing*, vol. 21, no. 7, pp. 2918–2932, 2007.
- [11] L. Wang, Z. Yang, and T. P. Waters, "Structural damage detection using cross correlation functions of vibration response," *Journal of Sound and Vibration*, vol. 329, no. 24, pp. 5070–5086, 2010.
- [12] L. Wang and Z. Yang, "Effect of response type and excitation frequency range on the structural damage detection method using correlation functions of vibration responses," *Journal of Sound and Vibration*, vol. 332, no. 4, pp. 645–653, 2013.
- [13] W. T. Yeung and J. W. Smith, "Damage detection in bridges using neural networks for pattern recognition of vibration signatures," *Engineering Structures*, vol. 27, no. 5, pp. 685–698, 2005.
- [14] Y. Qian and A. Mita, "Acceleration-based damage indicators for building structures using neural network emulators," *Structural Control and Health Monitoring*, vol. 15, no. 6, pp. 901–920, 2008.
- [15] A. Widodo and B.-S. Yang, "Support vector machine in machine condition monitoring and fault diagnosis," *Mechanical Systems and Signal Processing*, vol. 21, no. 6, pp. 2560–2574, 2007.
- [16] H.-X. He and W.-M. Yan, "Structural damage detection with wavelet support vector machine: introduction and applications," *Structural Control and Health Monitoring*, vol. 14, no. 1, pp. 162–176, 2007.
- [17] A. Widodo and B.-S. Yang, "Wavelet support vector machine for induction machine fault diagnosis based on transient current signal," *Expert Systems with Applications*, vol. 35, no. 1-2, pp. 307–316, 2008.
- [18] Y. Q. Ni, X. G. Hua, K. Q. Fan, and J. M. Ko, "Correlating modal properties with temperature using long-term monitoring data and support vector machine technique," *Engineering Structures*, vol. 27, no. 12, pp. 1762–1773, 2005.
- [19] K. Worden and A. J. Lane, "Damage identification using support vector machines," *Smart Materials and Structures*, vol. 10, no. 3, pp. 540–547, 2001.
- [20] C. K. Oh and H. Sohn, "Damage diagnosis under environmental and operational variations using unsupervised support vector machine," *Journal of Sound and Vibration*, vol. 325, no. 1-2, pp. 224–239, 2009.
- [21] H. Song, L. Zhong, and B. Han, "Structural damage detection by integrating independent component analysis and support vector machine," *International Journal of Systems Science*, vol. 37, no. 13, pp. 961–967, 2006.
- [22] Y. Yang, D. Yu, and J. Cheng, "A fault diagnosis approach for roller bearing based on IMF envelope spectrum and SVM," *Measurement*, vol. 40, no. 9-10, pp. 943–950, 2007.
- [23] W. Sun, G. A. Yang, Q. Chen, A. Palazoglu, and K. Feng, "Fault diagnosis of rolling bearing based on wavelet transform and envelope spectrum correlation," *Journal of Vibration and Control*, vol. 19, no. 6, pp. 924–941, 2013.
- [24] Q. Hu, Z. He, Z. Zhang, and Y. Zi, "Fault diagnosis of rotating machinery based on improved wavelet package transform and SVMs ensemble," *Mechanical Systems and Signal Processing*, vol. 21, no. 2, pp. 688–705, 2007.
- [25] F. He and W. Shi, "WPT-SVMs based approach for fault detection of valves in reciprocating pumps," in *Proceedings of the American Control Conference (ACC '02)*, vol. 6, pp. 4566–4570, IEEE, Anchorage, Alaska, USA, May 2002.
- [26] A. Cury and C. Crémona, "Pattern recognition of structural behaviors based on learning algorithms and symbolic data concepts," *Structural Control and Health Monitoring*, vol. 19, no. 2, pp. 161–186, 2012.
- [27] C. R. Farrar and G. H. James III, "System identification from ambient vibration measurements on a bridge," *Journal of Sound and Vibration*, vol. 205, no. 1, pp. 1–18, 1997.
- [28] C.-W. Hsu and C.-J. Lin, "A comparison of methods for multiclass support vector machines," *IEEE Transactions on Neural Networks*, vol. 13, no. 2, pp. 415–425, 2002.
- [29] R. R. Coifman and M. V. Wickerhauser, "Entropy-based algorithms for best basis selection," *IEEE Transactions on Information Theory*, vol. 38, no. 2, pp. 713–718, 1992.
- [30] Z. Sun and C. C. Chang, "Structural damage assessment based on wavelet packet transform," *Journal of Structural Engineering*, vol. 128, no. 10, pp. 1354–1361, 2002.
- [31] N. E. Huang, Z. Shen, S. R. Long et al., "The empirical mode decomposition and the Hilbert spectrum for nonlinear and non-stationary time series analysis," *Proceedings of the Royal Society of London A: Mathematical, Physical and Engineering Sciences*, vol. 454, no. 1971, pp. 903–995, 1998.
- [32] E. A. Johnson, H. F. Lam, L. S. Katafygiotis, and J. L. Beck, "Phase I IASC-ASCE structural health monitoring benchmark problem using simulated data," *Journal of Engineering Mechanics*, vol. 130, no. 1, pp. 3–15, 2004.
- [33] S. J. Orfanidis, *Optimum Signal Processing. An Introduction*, Prentice-Hall, Englewood Cliffs, NJ, USA, 2nd edition, 1996.
- [34] C. W. Hsu, C. C. Chang, and C. J. Lin, "A practical guide to support vector classification," Tech. Rep., Department of Computer Science and Information Engineering, National Taiwan University, Taipei, Taiwan, 2003, <http://www.csie.ntu.edu.tw/~cjlin/papers/guide/guide.pdf>.
- [35] C.-C. Chang and C.-J. Lin, "LIBSVM: a library for support vector machines," Tech. Rep., Department of Computer Science and Information Engineering, National Taiwan University, 2001, [http://www.cs.cmu.edu/~pakyuan/compbio/references/Chang\\_LIBSVM\\_2001.pdf](http://www.cs.cmu.edu/~pakyuan/compbio/references/Chang_LIBSVM_2001.pdf).
- [36] J.-G. Han, W.-X. Ren, and Z.-S. Sun, "Wavelet packet based damage identification of beam structures," *International Journal of Solids and Structures*, vol. 42, no. 26, pp. 6610–6627, 2005.

## Research Article

# An Experimental Study of Structural Identification of Bridges Using the Kinetic Energy Optimization Technique and the Direct Matrix Updating Method

**Gwanghee Heo and Joonryong Jeon**

*Department of Civil and Environment Engineering, Konyang University, 121 Daehak-ro, Nonsan, Chungnam 320-711, Republic of Korea*

Correspondence should be addressed to Joonryong Jeon; jrjeon@konyang.ac.kr

Received 25 September 2015; Accepted 27 December 2015

Academic Editor: Guillermo Rus

Copyright © 2016 G. Heo and J. Jeon. This is an open access article distributed under the Creative Commons Attribution License, which permits unrestricted use, distribution, and reproduction in any medium, provided the original work is properly cited.

This paper aims to develop an SI (structural identification) technique using the KEOT and the DMUM to decide on optimal location of sensors and to update FE model, respectively, which ultimately contributes to a composition of more effective SHM. Owing to the characteristic structural flexing behavior of cable bridges (e.g., cable-stayed bridges and suspension bridges), which makes them vulnerable to any vibration, systematic and continuous structural health monitoring (SHM) is pivotal for them. Since it is necessary to select optimal measurement locations with the fewest possible measurements and also to accurately assess the structural state of a bridge for the development of an effective SHM, an SI technique is as much important to accurately determine the modal parameters of the current structure based on the data optimally obtained. In this study, the kinetic energy optimization technique (KEOT) was utilized to determine the optimal measurement locations, while the direct matrix updating method (DMUM) was utilized for FE model updating. As a result of experiment, the required number of measurement locations derived from KEOT based on the target mode was reduced by approximately 80% compared to the initial number of measurement locations. Moreover, compared to the eigenvalue of the modal experiment, an improved FE model with a margin of error of less than 1% was derived from DMUM. Thus, the SI technique for cable-stayed bridges proposed in this study, which utilizes both KEOT and DMUM, is proven effective in minimizing the number of sensors while accurately determining the structural dynamic characteristics.

## 1. Introduction

During their service period, structures are exposed not only to gradual aging but also to unspecified harmful environmental effects, such as earthquakes, strong winds, impacts, and structural instability due to external forces that can give rise to various structural defects. These defects can in turn lead to reduced life expectancy and unexpected serious structural damage. Thus, from a long-term perspective, continuous structural health monitoring (SHM), systematic evaluation, and maintenance efforts are pivotal, especially for structures that are vulnerable to vibration occurring during service, such as cable-stayed bridges. For these efforts, a technique for accurate structural identification (SI) is of utmost importance.

SI is defined as the process of defining a mathematical model of a given structure using measured physical

information acquired from the actual target structure. Since Lie and Yao (1978) [1] introduced the concept of SI into structural engineering, many experiments have been conducted to identify a mathematical model that can represent the behavioral characteristics (equations of motion) of a target structure [2–5]. Despite such efforts, the SI technique has been applied in everyday practice in only a few cases and with limited effectiveness. It has not been adapted to convenient everyday application in general structural design and maintenance [6–8]. Appropriate utilization of the SI technique not only allows for thorough SHM of the target structure but also reduces the amount of effort required for evaluation and maintenance of the structure and can contribute to ensuring structural safety.

As explained above, to conduct SI, physical structural information must be obtained from the target structure through experimentation. In such experimentation, if

the number of sensor locations can be selectively reduced such that all measurement locations are optimized to the target mode, both efficiency and economic viability can be improved from an administrative viewpoint. Soundness monitoring, which requires long-term, real-time measurements, involves figure-intensive data processing and requires repetitive operations. Thus, maximizing the quality of the monitored information while minimizing the number of sensors is of particular importance [9–16]. To achieve this, Kammer [13] used estimated error covariance matrix (EECM) to develop a new approach called the effective independence method (EIM). This method incorporates the concept of *spatial independence* and is typically applied to truss structures. EIM guarantees linear independence, and its calculations are very effective with regard to sensor location selection.

On the other hand, Gwanghee [12] proposed the kinetic energy optimization technique (KEOT) based on principles of structural kinetic energy under the premise that optimizing the composition and location of sensors by maximizing the kinetic energy (KE) of a structure would be the most effective way of determining damage in structures that feature low and close interval frequencies and high attenuation [9–11]. This method acquires optimal modal information by maximizing the kinetic energy measured from the structural system, thus ensuring the independence of the measuring mode used in KEOT. These types of advantages became handy when applied to large structures, thus proving the usefulness of KEOT [12].

Moreover, for SI, the mathematical model of the target structure must be defined using physical information measured from the target structure [17, 18]. In this process, an FE model that represents the structural state of the target structure is developed based on the measured data of the target structure. In addition, if the numerical modal parameters can be derived, they can be used to define the state of the baseline structure. At this point, it is typical for a certain margin of error to come into play with respect to the modeling. This is because the method of FE model interpretation can vary depending on factors such as lifespan, economics, expected value of the structural model, and the fact that it is constructed based on initial architectural drawings. FE models developed to particularly resolve dynamic structural problems must effectively predict changes in modal parameters caused by alterations in design parameters. In this regard, FE model improvement not only provides dynamic characteristics that conform to the target structure but also can be utilized in the future as an objective and reasonable standard based on which aging and localized damage to a structure can be measured [19, 20]. In accordance with these needs, a range of FE model improvement methods [21] have been introduced. Namely, Friswell and Mottershead [22] have systematically organized classical theories such as the direct matrix updating method (DMUM) [23, 24] and the error matrix updating method (EMUM) [25, 26] and mathematically verified them to prove their validity. Thus, in this study, experiments were conducted to evaluate SI techniques aimed at accurately determining the modal parameters of a target structure based on optimal measurement locations

(i.e., minimum number of sensors), which are the required parameters for efficient and practical SHM. To this end, the optimal sensor locations were selected based on a model of a cable-stayed bridge and then the responses from the selected measurement locations were used to improve the FE model. Taking into account the structural characteristic of cable-stayed bridges, which feature relatively natural frequency of narrow interval and short cycle, KEOT was applied to select the optimal sensor locations. Moreover, to improve the FE model, DMUM was utilized because it requires fewer calculations, has high accuracy, and is practical for everyday use.

In conclusion, for structures such as cable-stayed bridges where the characteristic flexing behavior creates a natural frequency of narrow interval and short cycle, situations where multiple sensors are required because of structural complexity, and situations where there exist uncertainties in the FE model used for interpreting the data, KEOT and DMUM can facilitate rational and effective SI by enabling identification of the optimal sensor locations and improvement of the FE model. Ultimately, this study proves through experimentation that a combination of KEOT and DMUM is the ideal hybrid method to provide both practical and effective SHM.

## 2. Optimal Sensor Location and Finite Element (FE) Model Update

*2.1. Kinetic Energy Optimization Technique (KEOT).* In this study, the KEOT method was applied and evaluated for its effectiveness in selecting optimal sensor locations. KEOT recommends selecting optimal measurement locations by utilizing the strain-kinetic energy of the structure [9–12]. To do this, Kammer's EIM approach [13] involves optimizing and selecting a set of target modes in order to identify the structure based on FE analysis. An initial candidate set of transducer locations is also selected. These locations are then ranked based on their contribution to the linear independence of the corresponding FE model target mode partitions, and locations that do not contribute are removed from the candidate set. The described energy optimization technique algorithm is a modification of EIM, and it is designed to improve the modal information and maximize the measured kinetic energy of the structural system. The spatial independence of the identified mode shapes is satisfied by the sensing configuration obtained using the KEOT algorithm [11, 12]. The kinetic energy in the system is

$$KE = \Phi^T M \Phi, \quad (1)$$

where  $\Phi$  is the measured mode shape vector. After decomposing the mass matrix  $M$  into upper and lower triangular Cholesky factors, the kinetic energy matrix can be derived as

$$KE = \Psi^T \Psi, \quad (2)$$

where  $\Psi = U\Phi$  and  $M = LU$ . The matrices  $L$  and  $U$  denote the lower and upper triangular Cholesky factors.

The projection of the mode shapes onto the reduced configuration is denoted by

$$\begin{aligned}\bar{\Phi} &= \text{projection}(\Phi), \\ \bar{\Psi} &= \text{projection}(\Psi).\end{aligned}\quad (3)$$

Similarly, the energy measured by the reduced set of transducers is obtained from the initial energy by removing the contribution of all transducers that have been eliminated:

$$\bar{K}\bar{E} = \bar{\Psi}^T \bar{\Psi}. \quad (4)$$

The objective of the transducer placement is to find a reduced configuration that maximizes the measurement of the kinetic energy of the structure. It is desirable to stop eliminating the transducers when doing so results in a rank deficiency of the energy matrix. Assuming that the mass matrix is nonsingular, the column rank  $N$  of the quantity  $\bar{K}\bar{E}$  is equal to the number of linearly independent projected vectors in matrix  $\bar{\Phi}$ . The problem is solved iteratively by the following procedure. First, the eigenvalues  $\Lambda$  and eigenvectors  $\psi$  of the energy matrix are extracted:

$$\bar{K}\bar{E}\psi = \Lambda\psi. \quad (5)$$

Computing the eigenpairs at each iteration of the energy optimizing technique (EOT) procedure does not significantly increase the computational cost because the matrix  $\bar{K}\bar{E}$  is a square, symmetric, and positive-definite matrix of size  $N$ . Then, using an approach similar to Kammer's EIM [13], the fractional contributions of each remaining transducer are assembled into the KEOT vector:

$$\text{KEOT} = \sum_{i=1, \dots, m} [\bar{\Psi}\psi\Lambda^{-1/2}]^2. \quad (6)$$

The transducer location with the minimum contribution in the KEOT vector is then selected for removal. Subsequently, the contribution of the removed transducer to the kinetic energy matrix is deleted, and the new matrix is checked for rank deficiency. If the removal of the transducer produces a rank deficiency, it implies that the transducer location in question cannot be removed. If removing the transducer does not produce a rank deficiency, the transducer location is removed from the candidate set and the process is repeated until the required number of transducers is ascertained. Because it can be verified that the quantity between the brackets in (6) represents a linear combination of the measured mode shapes that is designed to produce orthogonal vectors,

$$[\bar{\Psi}\psi\Lambda^{-1/2}]^T [\bar{\Psi}\psi\Lambda^{-1/2}] = I. \quad (7)$$

Furthermore, each KEOT of the vector is a heuristic measure of the contribution of each transducer to the measured energy. The normalization factor  $\Lambda^{-1/2}$  prevents the contributions of high frequency modes from dominating the low frequency modes. In theory, the number of remaining transducers is equal to the size of the target modal set. However, the apparent rank is often increased due to noise in the experimental data, and more than  $M$  transducers are required to identify  $N$  independent modes.

*2.2. Direct Matrix Updating Method (DMUM).* In general, when a modified structure is added to or removed from the initial structure, changes occur in the dynamic characteristics of the structure. Dynamic characteristics before and after a structural change can be derived as eigenvalue formulas shown below:

$$\begin{aligned}([K] - \Lambda[M])\{\Phi\} &= 0, \\ (([K] + [\Delta K]) - \bar{\Lambda}([M] + [\Delta M]))\{\bar{\Phi}\} &= 0,\end{aligned}\quad (8)$$

where  $[K]$  is the stiffness matrix,  $[M]$  is the mass matrix, and  $[\Delta K]$  and  $[\Delta M]$  are changes in the stiffness and mass of the structure, respectively, due to structural changes. The elements  $\Lambda$  and  $\{\Phi\}$  are eigenvalue and eigenvector, respectively, and  $\bar{\Lambda}$  and  $\{\bar{\Phi}\}$  are changes in eigenvalue and eigenvector due to structural changes, respectively. Regarding the derivation methods available for calculating changes in stiffness  $[\Delta K]$  and mass  $[\Delta M]$  due to structural changes, this study selected and applied DMUM considering its effectiveness in FE model improvement as well as its convenience and practicality for everyday use. Here, using Lagrange multipliers, objective functions, composed to limit the range of change in the stiffness and mass matrices while simultaneously satisfying the eigenvalue, are shown below as (9). DMUM is advantageous from the perspective of usability because it can calculate the changes in stiffness and mass from just a single matrix operation [23, 24]:

$$\begin{aligned}\epsilon_K &= \left\| [K_A]^{-1/2} ([K_U] - [K_A]) [K_A]^{-1/2} \right\|, \\ \epsilon_M &= \left\| [M_A]^{-1/2} ([M_U] - [M_A]) [M_A]^{-1/2} \right\|,\end{aligned}\quad (9)$$

where  $[K_A]$  and  $[M_A]$  are the stiffness and mass matrices before structural change and  $[K_U]$  and  $[M_U]$  are the stiffness and mass matrices after structural change. The correlation between  $[K_A]$  and  $[K_U]$  can be expressed as shown in (10), and the correlation between  $[M_A]$  and  $[M_U]$  can be expressed as shown in (11):

$$[K_U] = [K_A] + [\Delta K], \quad (10)$$

$$[M_U] = [M_A] + [\Delta M]. \quad (11)$$

The element  $[\Delta K]$  in (10) can be defined as (14) using the interaction formulas of (12) and (13) [27]:

$$[K_U] - [K_U]^T = 0, \quad (12)$$

$$[\Phi_X]^T [K_U] [\Phi_X] - [\Lambda_X] = 0, \quad (13)$$

$$\begin{aligned}[\Delta K] &= -[K_A] [\Phi_X] [\Phi_X]^T [M_A] \\ &\quad - [M_A] [\Phi_X] [\Phi_X]^T [K_A] \\ &\quad + [M_A] [\Phi_X] [\Phi_X]^T [K_A] [K_A] [\Phi_X] [\Phi_X]^T [M_A] \\ &\quad + [M_A] [\Phi_X] [\Lambda_X] [\Phi_X]^T [M_A].\end{aligned}\quad (14)$$

The element  $[\Delta M]$  in (11) can be defined as (17) using the interaction formulas of (15) and (16) [28]:

$$[M_U] - [M_U]^T = 0, \quad (15)$$

$$[\Phi_X]^T [M_U] [\Phi_X] - [I] = 0, \quad (16)$$

$$\begin{aligned} [\Delta M] = & - [M_A] [\Phi_X] \left( [\Phi_X]^T [M_A] [\Phi_X] \right) \\ & + [\Phi_X]^T [K_A] \\ & + \left( [I] - [\Phi_X]^T [M_A] [\Phi_X] \right) \left( [\Phi_X]^T [M_A] [\Phi_X] \right). \end{aligned} \quad (17)$$

In this study, the objective of FE model improvement is FE interpretation and modal experiment results, so the subscript  $A$  in each equation is the result value based on analysis and subscript  $X$  is the result value based on experimentation.

### 3. FE Analysis and Modal Test of Model Structure

*3.1. Setup of the Model Structure (Cable-Stayed Bridge).* The second moment of inertia of the cable-stayed bridge model used in this study was reduced as much as possible so that the bridge slab would be sensitive to vibrations caused by external forces. Moreover, to make FE model configuration more convenient, the cross-sectional shape and the materials used for the members were simplified and unified. Further, to reduce the possibility of a production error, cross section dimensions were equalized and initial changes were minimized. The model used in this study is a three-span continuous beam structure with a total length of 4220 mm, a width of 170 mm, and a pylon height of 1000 mm. The cables are 0.8 mm steel wires, with ten wires connected to corresponding points on the crossbeam from each side of the pylon. The anchors located at each end of the model were composed of rollers, and the anchors of the pylons were composed of rollers and hinges. Finally, 1 kg of additional mass was added to the top of the bridge slab at each of the 39 points where the wires join the cross beam to maximize the flexibility of the bridge without creating any initial deflections. The model built using the components explained above is shown in Figure 1, and detailed design data is shown in Table 1.

During the assembly of the model, the cables were tensioned taking into consideration the effect of gravity on the superstructure across all sections. Thus, the self-weight of the superstructure was assumed to be a uniformly distributed load distributed at equal intervals across the cross beams and was utilized as the tensile force of the cables. To quantify the tensile force, a force gauge was utilized when tensioning the cables. After the completion of cable tensioning, a level was used to inspect the horizontality of the superstructure. In addition, the cables were tensioned progressively outward from the pylons and symmetrically left and right in accordance with the cable tensioning order of an actual cable-stayed bridge structure, as shown in Figure 2.

*3.2. FE Analysis of Model Structure (Cable-Stayed Bridge).* In order to analyze the structural dynamic properties of

TABLE 1: Design data of the cable-stayed bridge model.

Category	Data
Total length	4.22 m
Length of the center span	2.22 m
Length of each side span	1.0 m
Width of the superstructure	0.17 m
Pylon height	1.00 m
Pylon anchor type	Roller and hinge (Pin)
Bridge end anchor type	Roller
Diameter of cable	0.8 mm

the produced model bridge, in this paper, FE modeling-based numerical analysis was conducted. For this purpose, IDEAS from UGS, a commercial structural analysis program, was used, and a three-dimensional detailed FE model was organized as in Figure 3 by applying the physical properties of Table 2. Here, 1D beam element was considered for the bridge deck and the tower of the structure, rigid element was considered for the bridge deck boundary conditions, and 1D rod element was considered for cable; as for the floor beam and lumped mass, 1 kg size of lumped mass was considered for each of the 39 nodes, which are the positions of the floor beams on the area of the central bridge deck excluding the pylon and both sides. Next, as for the boundary condition, clamp was considered for the substructure of the pylon, roller was considered for the both sides of superstructure and the right-side pylon connection, and Pin was considered for the left-side pylon connection. Lastly, as for the freedom degree condition of the structure, DOF was given in the direction of  $y$ -axis with the 39 nodes on the central bridge deck as the base to complete the three-dimensional detailed FE model. In this context, the FE analysis of the model bridge considered a total of two lowest flecion modes for the purpose of vertical vibration control, and the natural frequency and mode shape of the model bridge that has been analyzed with Guyan reduction method applied are as in Figure 4.

In this paper, the DOFs of FE model were reduced into thirty-nine, with application of Guyan reduction method [29] by which a structural analysis of eigenvalues is made by reducing removed DOFs into unremoved ones and in turn composing a matrix of reduced strength and mass as in (18). Therefore, it has become possible to reduce the DOFs by selecting a desired point of measurement and to effectively perform structural FE analysis. Here, each  $r$  refers to a retained set and  $o$  to an omitted set. Equation (18) is applied for an analysis of eigenvalues, based on an optimal location of measurement determined in Section 4.1:

$$\begin{aligned} K_r &= K_{rr} - K_{ro} K_{oo}^{-1} K_{ro}^T, \\ M_r &= M_{rr} - M_{ro} K_{oo}^{-1} K_{ro}^T - K_{ro} K_{oo}^{-1} M_{ro}^T \\ &\quad + K_{ro} K_{oo}^{-1} M_{oo} K_{oo}^{-1} K_{ro}^T. \end{aligned} \quad (18)$$

As shown in Figure 4, based on the total of 39 DOF, Guyan reduction method was applied to interpret the frequency of

TABLE 2: Material properties of the cable-stayed bridge model.

Material property	Modulus of elasticity (kgf/mm <sup>2</sup> )	Shear modulus of elasticity (kgf/mm <sup>2</sup> )	Poisson's ratio	Unit weight (kgf/mm <sup>3</sup> )	Yield strength (kgf/mm <sup>2</sup> )
Steel	$2.10 \times 10^4$	$8.10 \times 10^3$	0.30	$7.85 \times 10^{-6}$	40

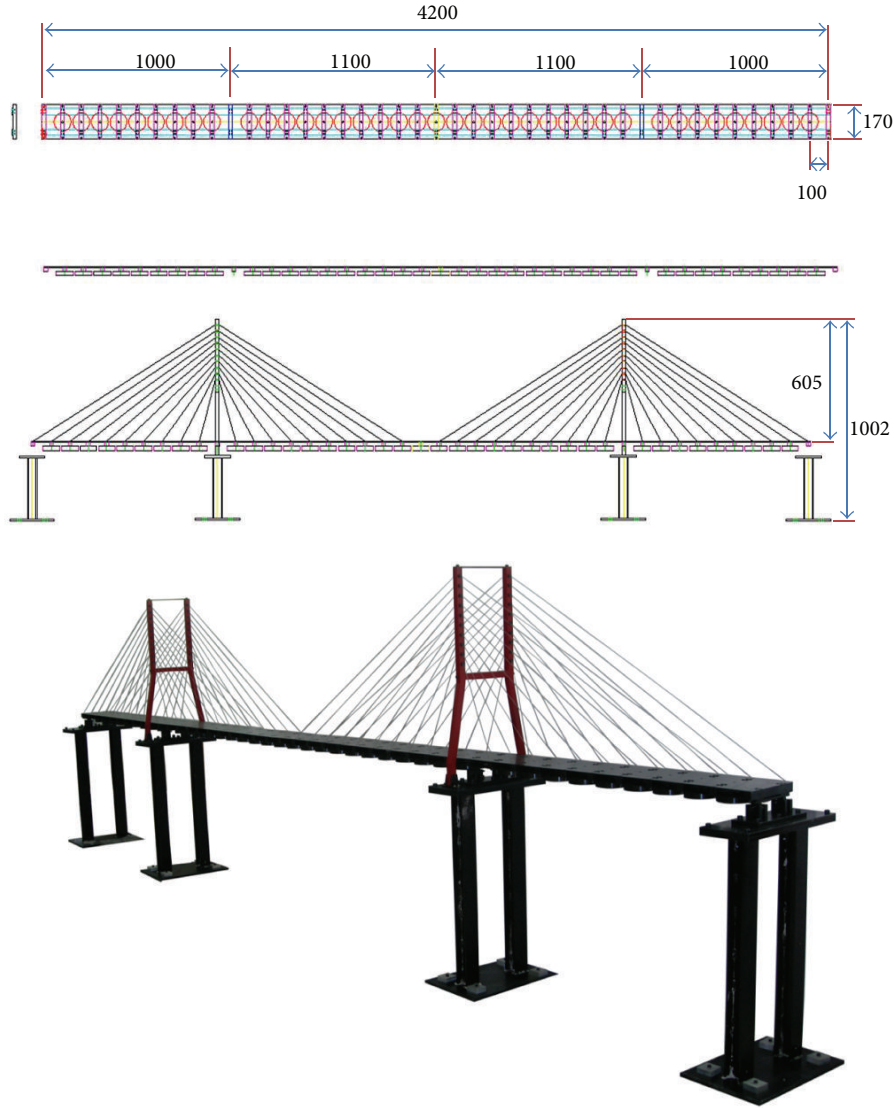


FIGURE 1: View of the cable-stayed bridge model.

vibration and the mode shape, with the results shown in Table 3.

3.3. *Modal Test of the Model Structure (Cable-Stayed Bridge).* To confirm the validity of the composed FE model and to analyze the fundamental kinetic characteristics of the model bridge, this study employed a modal test conducted using an impact hammer. An HP-VXI 1432 was used to measure the response signals from the structure, and data was obtained and analyzed by utilizing T-DAS by MTS. In order to obtain acceleration responses of the structure, Dytran model 3134D

was used for a total of 39 points on the bridge deck that had been selected in equal intervals. To connect the accelerometer to the experimental bridge model and the measurement system, 10 ft cables were used for each channel. The impact hammer used to create vibratory forces in the structure was a 5850A model produced by Dytran, and the center of the slab was selected as the location of the impact.

The size of each frame of the measured frequency response function (FRF) was set to 2048, and the maximum frequency range was set to 35 Hz. Data was collected by averaging the results of 30 tests. Finally, the acquired time and

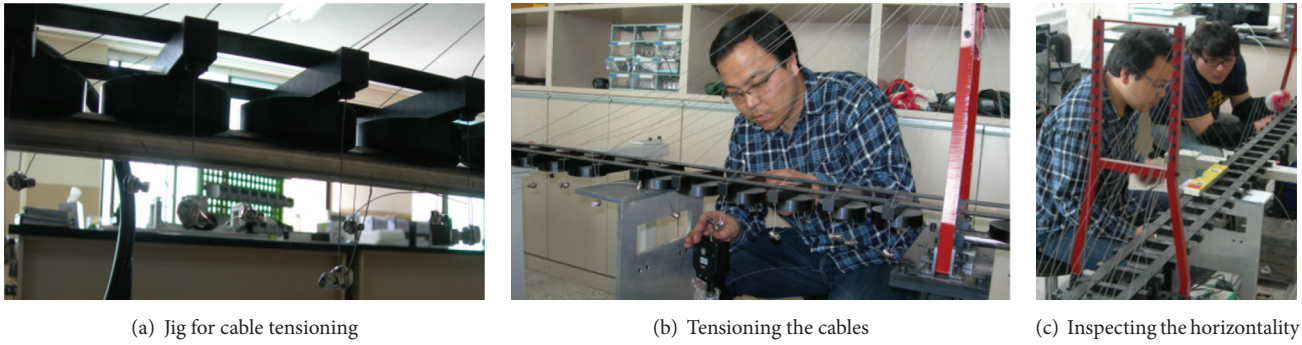
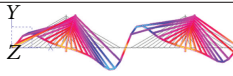
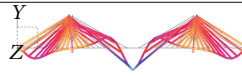


FIGURE 2: Steps for tensioning the cables of the cable-stayed bridge model.

TABLE 3: FE analysis results of the cable-stayed bridge model.

	1st bending	2nd bending	3rd bending
Analysis results	 9.1719 Hz	 11.2544 Hz	 16.8643 Hz

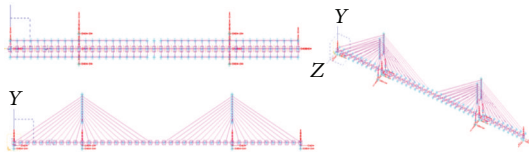


FIGURE 3: Initial FE modeling of the model bridge using I-DEAS.

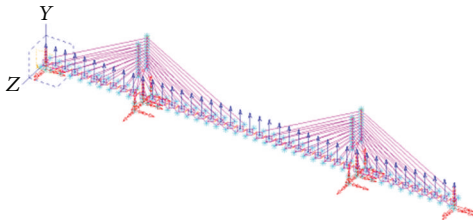


FIGURE 4: Initial FE modeling of the model bridge using I-DEAS (39 DOF).

frequency responses are as shown in Figure 5, and the results of the modal test analysis are as shown in Table 4.

To confirm the validity of using the FE model to understand the dynamic behavior characteristics of the model bridge and for use in deriving the modal parameters for future SHM and maintenance, this study compares and contrasts the frequency results of the FE model analysis and the modal experiment as shown in Table 5. As observed from the data in the table, reliable results were achieved, with an error ratio of around 1% between the FE analysis and the modal experiment. These results prove that the detailed FE model constructed in this study reliably mimicked the behavioral characteristics of the actual structural model, thereby confirming its validity.

The analysis and experimental results above were acquired using a total of 39 DOF and sensors. From the standpoint of long-term continuous SHM and from the practical standpoint of everyday evaluation and maintenance, using the whole structure to acquire signals as done in this study may be inefficient and impractical. Doing so would require a great number of sensors as well as a great deal of labor to install them. Moreover, interpreting and sorting through the resulting massive amount of data would be a laborious task. To resolve this problem, an alternative approach is required. This study therefore considers an approach whereby optimal sensor locations are selectively chosen in order to acquire the maximum information about the behavioral characteristics of the structure from a minimum number of sensors. By selecting the optimal locations, the sensors can thus be positioned at the most rational and efficient points to acquire the target information. Moreover, the sensor locations selected through this approach can later be utilized as real-time sensor locations for actual structures.

#### 4. Optimal Sensor Location and FE Model Updating of the Model Bridge

*4.1. Optimal Sensor Location Using the KEOT.* The aim of this study is to conduct SI with a limited number of sensors by selecting the optimal sensor locations. To select the optimal sensor locations, we utilized KEOT, which maximizes the structure's strain-kinetic energy to enable consideration of the optimal measurement conditions. The KEOT method has proven to be effective for ascertaining the kinetic parameters of structures that feature low and short-interval frequencies, such as the cable-stayed bridge used in this study [9–12]. In this study, we set out to use KEOT to select the optimal sensor locations to represent the three lowest bending modes

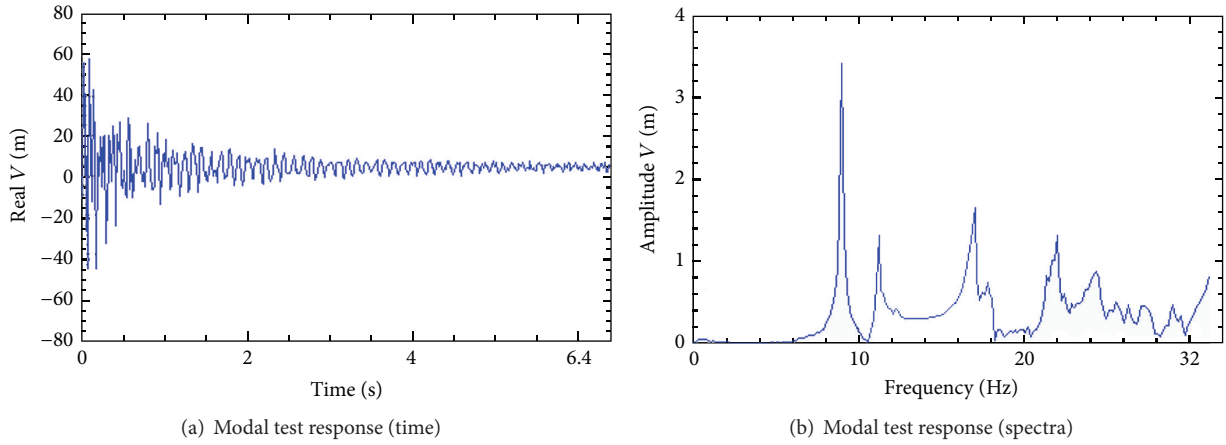


FIGURE 5: Modal test results.

TABLE 4: Results of the modal test of the cable-stayed bridge model.

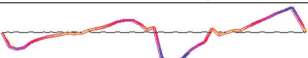
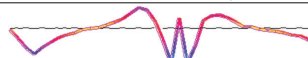
	1st bending	2nd bending	3rd bending
Modal test results			
	9.0890 Hz	11.2557 Hz	17.1442 Hz

TABLE 5: Comparison of analysis and experimental frequency.

	Analysis and experimental results		
	FE analysis results (Hz)	Modal experiment results (Hz)	Error ratio (%)
1st bending mode	9.1719	9.0890	0.9120
2nd bending mode	11.2544	11.2557	0.0115
3rd bending mode	16.8643	17.1442	1.0326

TABLE 6: FE analysis results per DOF of cable-stayed bridge model using EOT.

DOF	Target mode	1st bending		2nd bending		3rd bending	
	Reduction (%)	Freq. (Hz)	Error (%)	Freq. (Hz)	Error (%)	Freq. (Hz)	Error (%)
39 (full)	—	9.1719	—	11.2544	—	16.8643	—
30	23.07	9.1728	0.0009	11.2567	0.0204	16.8691	0.0284
25	35.89	9.1757	0.0414	11.2651	0.0950	16.8856	0.1263
20	48.71	9.1890	0.1864	11.3049	0.4487	16.9834	0.7062
15	61.53	9.2219	0.5451	11.7537	4.4364	17.2843	2.4904
10	74.35	9.3253	1.6724	11.7537	4.4364	18.1914	7.8692
5	87.17	9.5531	4.1561	12.3951	10.1355	18.8781	11.9412

among the 39 DOF nodes. The three lowest bending modes are important and interesting modes that can occur during vertical vibration and thus should be the target modes for SI. Also, the optimal sensor locations were selected with a low error rate based on these target modes. Figure 6 and Table 5 show the optimal sensor locations selected and the results of interpretation using the KEOT method compared to the rate of error in frequency evaluated per DOF node. Rank deficiency in the energy matrix did not occur until the 39 sensor locations had been reduced to 2. This study therefore limited the final reduced DOF count to 5 and selected

the optimal sensor locations based on analysis of changes in eigenvalue.

By observing the trends in optimal sensor locations selected through gradual removal of DOF nodes (as shown in Table 6), it can be observed that when the total of 39 locations had been reduced to 10 (at the 75% reduction point), all of the left- and right-side span sensor locations had been removed. Thus, it was concluded that the strain-kinetic energy due to the 1st, 2nd, and 3rd bending mode behaviors was smaller in the side spans than in the center span. On the other hand, within the center span, the remaining sensor

S/L \ DOF	Number of sensor locations (total 39 nodes)																																																				
	2	3	4	5	6	7	8	9	10	12	13	14	15	16	17	18	19	20	21	22	23	24	25	26	27	28	29	30	31	32	33	34	35	36	37	38	39	40	41	42													
30	.	.	.	.	.	.	.					.	.	.	.	.	.	.	.	.	.	.	.	.	.	.	.	.	.	.	.	.	.	.	.	.	.	.	.	.	.	.	.	.									
25		.	.	.	.	.							.	.	.	.	.	.	.	.	.	.	.	.	.	.	.	.	.	.	.	.	.	.	.	.	.	.	.	.	.	.	.	.									
20		.	.	.	.									.	.	.	.	.	.	.	.	.	.	.	.	.	.	.	.	.	.	.	.	.	.	.	.	.	.	.	.	.	.	.	.								
15			.	.											.	.	.	.	.	.	.	.	.	.	.	.	.	.	.	.	.	.	.	.	.	.	.	.	.	.	.	.	.	.	.								
10			.													.	.	.	.	.	.	.	.	.	.	.	.	.	.	.	.	.	.	.	.	.	.	.	.	.	.	.	.	.	.	.							
9			.													.	.	.	.	.	.	.	.	.	.	.	.	.	.	.	.	.	.	.	.	.	.	.	.	.	.	.	.	.	.	.							
8			.													.	.	.	.	.	.	.	.	.	.	.	.	.	.	.	.	.	.	.	.	.	.	.	.	.	.	.	.	.	.	.	.						
7																.	.	.	.	.	.	.	.	.	.	.	.	.	.	.	.	.	.	.	.	.	.	.	.	.	.	.	.	.	.	.	.	.					
6																.	.	.	.	.	.	.	.	.	.	.	.	.	.	.	.	.	.	.	.	.	.	.	.	.	.	.	.	.	.	.	.	.	.				
5																.	.	.	.	.	.	.	.	.	.	.	.	.	.	.	.	.	.	.	.	.	.	.	.	.	.	.	.	.	.	.	.	.	.	.			
4																.	.	.	.	.	.	.	.	.	.	.	.	.	.	.	.	.	.	.	.	.	.	.	.	.	.	.	.	.	.	.	.	.	.	.	.		
3																.	.	.	.	.	.	.	.	.	.	.	.	.	.	.	.	.	.	.	.	.	.	.	.	.	.	.	.	.	.	.	.	.	.	.	.		
2																.	.	.	.	.	.	.	.	.	.	.	.	.	.	.	.	.	.	.	.	.	.	.	.	.	.	.	.	.	.	.	.	.	.	.	.	.	
1																.	.	.	.	.	.	.	.	.	.	.	.	.	.	.	.	.	.	.	.	.	.	.	.	.	.	.	.	.	.	.	.	.	.	.	.	.	.

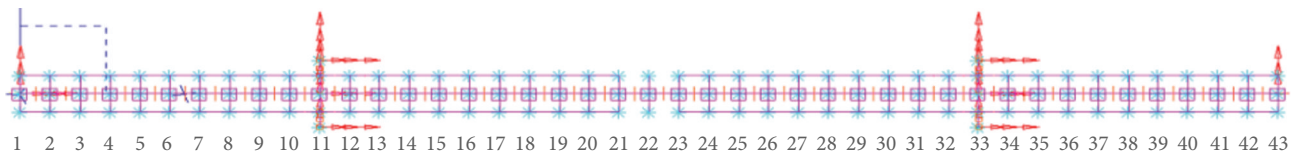


FIGURE 6: Study of optimal sensor locations selected using the EOT method.

locations grouped around nodes 19, 22, and 25 accounted for all the 1st, 2nd, and 3rd bending modes. These three nodes remained until only three sensor locations were left (at the 92.5% reduction point). Thus, it was concluded that nodes 19, 22, and 25 were the essential sensor locations that can most optimally represent the 1st, 2nd, and 3rd bending modes simultaneously. In conclusion, for comprehensive representation of the 1st, 2nd, and 3rd resonance modes, which have the greatest impact on bending, it is essential that these three sensor locations are included.

On the other hand, when sensor locations or DOF nodes are removed using the KEOT method explained above, changes in eigenvalue can be impacted due to the reduction in DOF. This study evaluated changes in eigenvalue when DOF nodes are removed using KEOT. Table 6 shows the results of eigenvalue analysis when the 39 DOF nodes are reduced to 30, 25, 20, 15, 10, and finally 5.

As shown in Table 6, changes in eigenvalue were clearly observed as the total of 39 DOF nodes was reduced to 25, 20, 15, 10, and 5. Looking closely at the changes in frequency, it was also observed that, with the reduction in the number of DOF nodes, the frequency steadily increased. In the case of the 1st bending mode, the frequency error ratio significantly increased when DOF nodes were reduced to 10 (reduction rate of about 75%) and the error ratio exceeded 4% when they were reduced to 5 (reduction rate of about 87%). In the case of the 2nd bending mode, the frequency error ratio

increased significantly when the DOF nodes were reduced to 15 (reduction rate of about 60%). It was close to 4.5% when the nodes were reduced to 10 (reduction rate of about 75%) and exceeded 10% when the nodes were reduced to 5 (reduction rate of about 87%). Moreover, in the case of the 3rd bending mode, the frequency error ratio significantly increased when the DOF nodes were reduced to 15 (reduction rate of about 60%). It was close to 8% when the nodes were reduced to 10 (reduction rate of about 75%) and reached about 12% when the nodes were reduced to 5 (reduction rate of about 87%).

These tendencies are due to the fact that stiffness is the most considered factor in the process of condensing the behavioral characteristics of an entire structure to a limited number of DOF nodes. In conclusion, to derive FE analysis results using Guyan reduction [29], it is important to select the range of allowable error ratio and the corresponding reduction of DOF nodes. Otherwise, excessive reduction in the number of DOF nodes will increase the frequency error ratio and lead to discrepancies in the initial FE analysis and modal test results, ultimately producing distorted frequency results.

Using the above results, a total of seven sensor locations were selected to include the three optimal sensor locations 19, 22, and 25, to limit the frequency error ratio to less than 10% and to clearly observe the shape of the modes. Using the KEOT method, the optimal sensor locations selected were 18, 19, 21, 22, 23, 25, and 26.

TABLE 7: Frequency and mode shape of 7 DOF using KEOT.

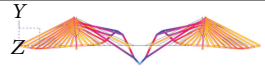
DOF	FE model	1st mode shape	2nd mode shape	3rd mode shape
7		 9.4244 Hz	 12.0453 Hz	 18.8065 Hz

TABLE 8: Comparison of 7 DOF analysis results and full DOF cases.

	Analysis (7 DOF) versus analysis (39 DOF)			Analysis (7 DOF) versus experimental (39 DOF)		
	Analysis (7 DOF)	Analysis (39 DOF)	Error (%)	Analysis (7 DOF)	Experimental (39 DOF)	Error (%)
1st mode	9.4244 Hz	9.1719 Hz	2.7529	9.4244 Hz	9.0890 Hz	3.6900
2nd mode	12.0453 Hz	11.2544 Hz	7.9160	12.0453 Hz	11.2557 Hz	7.0151
3rd mode	18.8065 Hz	16.8643 Hz	11.5166	18.8065 Hz	17.1442 Hz	9.6959

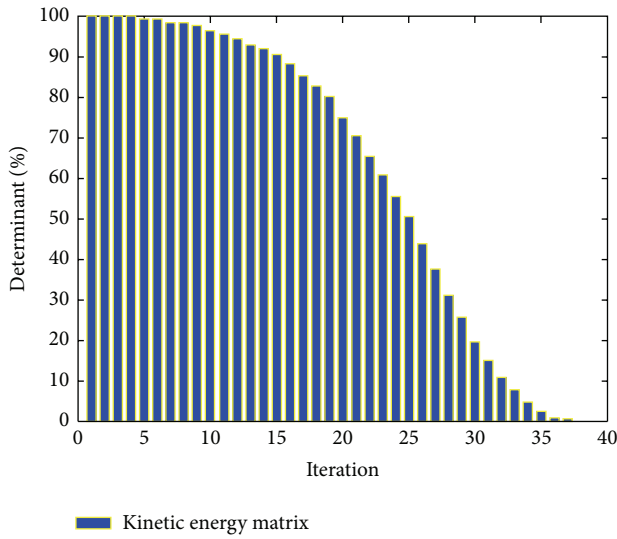


FIGURE 7: Kinetic energy matrix values to DOF modification.

Figure 7 illustrates the distribution of kinetic energy for each DOF condition as calculated and derived in this experiment using the KEOT. It can be observed from Figure 7 that as the number of DOF nodes (sensor locations) was gradually reduced, the total kinetic energy contribution of the remaining nodes was also reduced. In the case of the model bridge used in this study, when the number of DOF nodes was reduced to 15, the kinetic energy contribution was 90%. The contribution of kinetic energy decreased significantly with subsequent removals of DOF nodes. Moreover, when the number of DOF nodes was reduced to the seven optimal sensor locations selected in this study, the kinetic energy contribution was about 10%.

In this study, we conducted SI on a model of a cable-stayed bridge using seven sensors. As described above, the locations of the seven sensors, selected using the KEOT method, were nodes 18, 19, 21, 22, 23, 25, and 26. The total contribution of kinetic energy from these nodes was about 10%. The selection of the seven sensor locations used in this study was verified

by the inclusion of the three DOF nodes (19, 22, and 25) that were considered to be the essential sensor locations for most effectively and simultaneously representing the 1st, 2nd, and 3rd bending modes even at a 92.5% reduction in the number of DOF nodes. The results derived from the FE model and frequency analysis based on the seven selected sensor locations are shown in Table 7.

Table 7 shows that reducing the number of DOF nodes results in changes in frequency. For quantitative analysis of the changes in frequency, the frequency results and error ratio derived from the initial study with all 39 DOF nodes along with those derived from the modal test are shown in Table 8.

As observed in Table 8, using seven DOF nodes (approximately 82% reduction of DOF nodes) resulted in an error ratio of approximately 2.7–11.5% compared to that in the results of FE analysis using all 39 DOF nodes. In addition, using seven DOF nodes resulted in an error ratio of about 3.6–9.6% compared to the modal test results. The correlation between the mode shape acquired from the FE analysis using seven DOF nodes and the mode shape acquired from the modal test was further evaluated using the modal assurance criterion (MAC) shown in (19) [30]:

$$\text{MAC}(A, X) = \frac{\left| \sum_{j=1}^n (\Phi_X)_j (\Phi_A)_j^* \right|^2}{\left( \sum_{j=1}^n (\Phi_X)_j (\Phi_X)_j^* \right) \left( \sum_{j=1}^n (\Phi_A)_j (\Phi_A)_j^* \right)}. \quad (19)$$

Here,  $\Phi_A$  and  $\Phi_X$  are the mode shapes as calculated and acquired from the analysis and test, respectively. When the two modes are the same, the MAC value equals 1, and when the two modes have no correlation, the MAC value equals 0 [31]. Similarly, Ewins [30] points out in his study that the most highly correlated modes will have a MAC value of around 0.9, with MAC values as low as 0.7 considered fair in some cases. He also asserts that modes with no correlation will have MAC values of around 0.005. Figure 8 and Table 9 illustrate that the mode shapes studied in this research showed satisfactory correlations, but the 3rd bending mode had a relatively lower correlation than those of the 1st and 2nd modes.

TABLE 9: MAC values (7 DOF anal. and exp.).

	FE analysis modes		
	1st	2nd	3rd
Experimental modes			
1st	<b>0.9886</b>	0.0000	0.4304
2nd	0.0055	<b>0.9953</b>	0.0017
3rd	0.0259	0.0000	<b>0.7663</b>

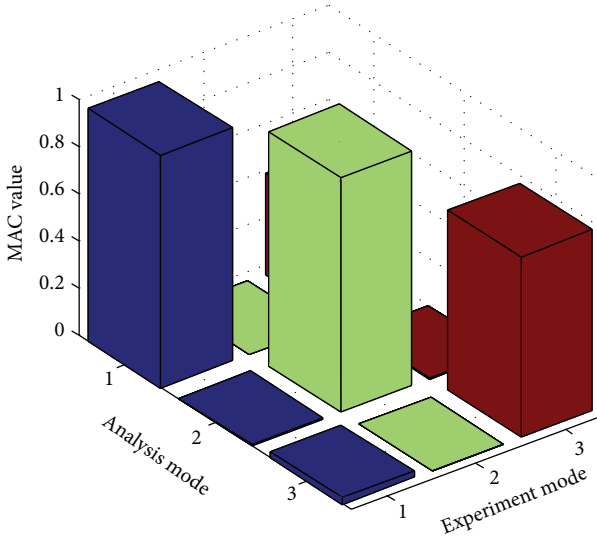


FIGURE 8: MAC plot (7 DOF anal. and exp.).

The changes in frequency shown in Table 8 and the changes in mode shape shown in Figure 8 and Table 9 are interpretation errors (FE modeling errors) created as a result of reduction of the DOF nodes. To accomplish a thorough SI of a structure as targeted in this study, more accurate modal information needs to be provided regarding the model bridge, and the discrepancies between the analysis results using the seven DOF nodes and the modal test results need to be overcome. Therefore, DMUM was utilized in this study in order to overcome FE modeling errors based on modal test values and to derive a baseline structure that can provide valid modal information.

**4.2. FE Model Updating Using DMUM.** FE model updating is a technique designed to overcome modeling errors in FE analysis and to secure an accurate model for numerical analysis of the current state of the structure taking into account potential construction errors. In FE model updating, the modal test results derived from the actual structure are applied to the FE analysis results to ultimately create an ideal FE model that contains the modal information of the current structure. This updated FE model can reliably reflect the dynamic behavioral characteristics of the actual structure. The updated model also plays a very important role in acquiring numerical analysis results, which is necessary for accurate assessment of structural states. To achieve FE model updating using DMUM, this study utilized frequency,

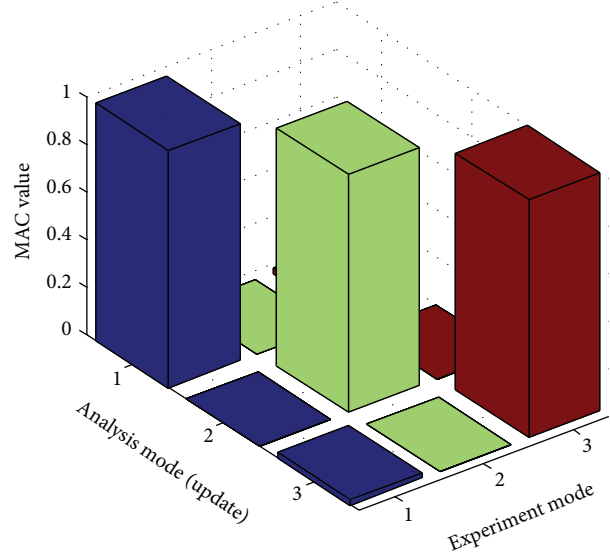


FIGURE 9: MAC plot (update and exp.).

mode shape, and mass and stiffness matrix results derived from the FE analysis along with frequency and mode shape results acquired from the modal test. Table 10 reflects the error ratio between the frequency results derived from the FE model updated using DMUM and the frequency results acquired from the modal test. As shown in Table 10, it was confirmed that the results derived from FE model updating had a significantly lower error rate (close to 0).

Next, to verify the effectiveness of DMUM in FE model updating, MAC tests were conducted on the mode shapes. The results of the correlation analysis between the mode shapes derived from the updated FE model and those derived from the modal test are as shown in Figure 9 and Table 11. The results show that using DMUM to update the FE model results in a MAC value of “1,” thus demonstrating an outstanding correlation with the modal test results.

In addition, in order to visualize the mode correlation evaluated using MAC and to evaluate the correlation between mode shapes before and after FE model updating, the mode shapes derived from analysis using seven DOF nodes or sensor locations and the mode shapes derived from the updated FE model were graphed as shown in Figure 10. As the graphs illustrate, the mode shape from the updated FE model follows the mode shape of the modal test, and not the mode shape of the FE analysis. This verifies the fact that by incorporating the modal information of the structure, FE model updating not only provides more accurate frequency values but also provides more accurate mode shape patterns. Ultimately, this proves that FE model updating using DMUM can overcome modeling errors and it is an effective way to create an accurate model for numerical analysis that can take into account the actual state of the structure.

**5. Conclusion**

The aim of this study was to research the formulation of a baseline structure through optimal sensor location selection

TABLE 10: Comparison of experimental results and updating results.

	Analysis and experimental results using EOT		Error ratio %
	FE model update	Experimental	
1st mode	9.0880 Hz	9.0890 Hz	0.0110
2nd mode	11.2543 Hz	11.2557 Hz	0.0124
3rd mode	17.1418 Hz	17.1442 Hz	0.0139

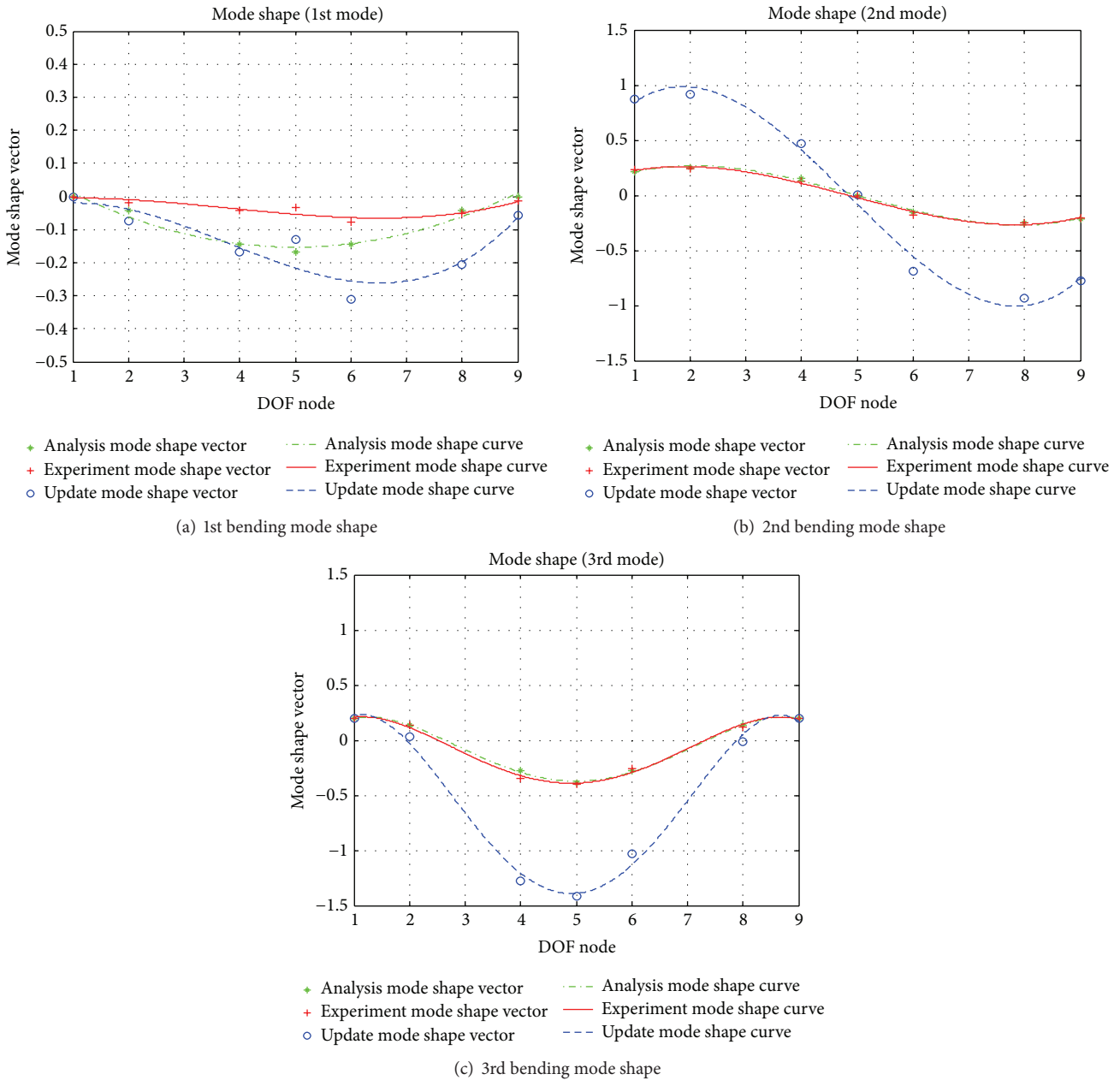


FIGURE 10: Comparison of 7 DOF analysis, updating, and experimental mode shapes.

and FE model updating for conducting SI on cable-stayed bridges. The conclusions are as follows:

- (1) By comparing the contribution of each DOF node to the total kinetic energy and progressively removing

those that do not contribute based on the target modes, the KEOT method was proven to be an effective approach for selecting the optimal number and location of sensors among the multiple sensor locations (DOF) in order to acquire the desired

TABLE II: MAC values (updating and exp.).

Experiment modes	FE analysis modes (update)		
	1st	2nd	3rd
1st	<b>1.0000</b>	0.0003	0.0225
2nd	0.0002	<b>1.0000</b>	0.0005
3rd	0.0226	0.0005	<b>1.0000</b>

responses. In this study, using seven sensors out of a total of 39 sensor locations to consider the three lowest bending modes (about 20% of the total) was sufficient to effectively acquire relevant structural information on the cable-stayed bridge.

- (2) In addition, by applying structural information measured from the actual structure and constructing a corresponding FE model to overcome initial errors in FE modeling, the DMUM method was proven to be an effective method for defining a baseline structure that incorporates the behavioral characteristics of the actual structure. DMUM has particularly strong potential for practical use from temporal and economical standpoints because it calculates stiffness and mass values from just a single matrix operation as opposed to other methods that require repetitive operations such as EMUM.
- (3) In conclusion, for structures such as cable-stayed bridges where the characteristic flexing behavior creates low and short-interval frequencies, situations where multiple sensor locations (DOF) are required because of structural complexity, and situations where SHM and evaluation and maintenance needs to be performed on structures with low and short-interval frequencies, the use of both KEOT and DMUM can be the most effective approach for conducting SI from the standpoints of both economy and usability because they provide accurate results with minimum number of measurement locations.

## Conflict of Interests

The authors declare that there is no conflict of interests regarding the publication of this paper.

## Acknowledgments

This research was supported by the Basic Science Research Program through the National Research Foundation of Korea (NRF) funded by the Ministry of Education, Science and Technology (Grant no. NRF-2013R1A2A1A01016192) and funded by the Ministry of Science, ICT and Future Planning (Grant no. NRF-2013R1A1A1063540).

## References

- [1] S. C. Lie and J. T. P. Yao, "Structural identification concept," *Journal of the Structural Division*, vol. 104, no. 12, pp. 1845–1858, 1978.
- [2] G. F. Sirca Jr. and H. Adeli, "System identification in structural engineering," *Scientia Iranica A*, vol. 19, no. 6, pp. 1355–1364, 2012.
- [3] V. Arora, "Structural damping identification method using normal FRFs," *International Journal of Solids and Structures*, vol. 51, no. 1, pp. 133–143, 2014.
- [4] Z. D. Zheng, Z. R. Lu, W. H. Chen, and J. K. Liu, "Structural damage identification based on power spectral density sensitivity analysis of dynamic responses," *Computers & Structures*, vol. 146, pp. 176–184, 2015.
- [5] D. Dessi and G. Camerlengo, "Damage identification techniques via modal curvature analysis: overview and comparison," *Mechanical Systems and Signal Processing*, vol. 52–53, pp. 181–205, 2015.
- [6] C. Farrar and P. J. Cornwell, "Structural health monitoring studies of the alamosa canyon and I-40 bridges," Tech. Rep. LA-13635-MS, Los Alamos National Laboratory, Los Alamos, NM, USA, 1998.
- [7] F. Benedettini, M. Dilena, and A. Morassi, "Vibration analysis and structural identification of a curved multi-span viaduct," *Mechanical Systems and Signal Processing*, vol. 54–55, pp. 84–107, 2015.
- [8] H. Chen, M. Kurt, Y. S. Lee, D. M. McFarland, L. A. Bergman, and A. F. Vakakis, "Experimental system identification of the dynamics of a vibro-impact beam with a view towards structural health monitoring and damage detection," *Mechanical Systems and Signal Processing*, vol. 46, no. 1, pp. 91–113, 2014.
- [9] M. L. Wang, G. Heo, and D. Satpathi, "Dynamic characterization of a long span bridge: a finite element based approach," *Soil Dynamics and Earthquake Engineering*, vol. 16, no. 7–8, pp. 503–512, 1997.
- [10] M. L. Wang, G. Heo, and D. Satpathi, "A health monitoring system for large structural systems," *Smart Materials and Structures*, vol. 7, no. 5, pp. 606–616, 1998.
- [11] G. Heo, M. L. Wang, and D. Satpathi, "Optimal transducer placement for health monitoring of long span bridge," *Soil Dynamics and Earthquake Engineering*, vol. 16, no. 7–8, pp. 495–502, 1997.
- [12] H. Gwanghee, *An automated health monitoring system for large civil structural system [Ph.D. thesis]*, University of New Mexico, Albuquerque, NM, USA, 1997.
- [13] D. C. Kammer, "Effect of model error on sensor placement for on-orbit modal identification of large space structures," *Journal of Guidance, Control, and Dynamics*, vol. 15, no. 2, pp. 334–341, 1992.
- [14] F. E. Udawadia, "Methodology for optimum sensor locations for parameter identification in dynamic systems," *Journal of Engineering Mechanics*, vol. 120, no. 2, pp. 368–387, 1994.
- [15] A. R. M. Rao, K. Lakshmi, and S. Krishnakumar, "A generalized optimal sensor placement technique for structural health monitoring and system identification," *Procedia Engineering*, vol. 86, pp. 529–538, 2014.
- [16] Z. Y. Shi, S. S. Law, and L. M. Zhang, "Optimum sensor placement of structural damage detection," *Journal of Engineering Mechanics*, vol. 126, no. 11, pp. 1173–1179, 2000.

- [17] T. Pothisiri and K. D. Hjelmstad, "Structural damage detection and assessment from modal response," *Journal of Engineering Mechanics*, vol. 129, no. 2, pp. 135–145, 2003.
- [18] M. Ge and E. M. Lui, "Structural damage identification using system dynamic properties," *Computers and Structures*, vol. 83, no. 27, pp. 2185–2196, 2005.
- [19] T. P. Waters, *Finite element model updating using measured frequency response functions [Ph.D. thesis]*, Department of Aerospace Engineering, University of Bristol, Bristol, UK, 1995.
- [20] Q. W. Zhang, C. C. Chang, and T. Y. P. Chang, "Finite element model updating for structures with parametric constraints," *Earthquake Engineering and Structural Dynamics*, vol. 29, no. 7, pp. 927–944, 2000.
- [21] J. E. Mottershead and M. I. Friswell, "Model updating in structural dynamics: a survey," *Journal of Sound and Vibration*, vol. 167, no. 2, pp. 347–375, 1993.
- [22] M. I. Friswell and J. E. Mottershead, *Finite Element Model Updating in Structural Dynamics*, vol. 38 of *Solid Mechanics and its Applications*, Kluwer Academic Publishers, Dordrecht, The Netherlands, 1995.
- [23] M. Baruch, "Optimization procedure to correct stiffness and flexibility matrices using vibration tests," *AIAA Journal*, vol. 16, no. 11, pp. 1208–1210, 1978.
- [24] A. Berman and E. J. Nagy, "Improvement of a large analytical model using test data," *AIAA Journal*, vol. 21, no. 8, pp. 1168–1173, 1983.
- [25] J. Sidhu and D. J. Ewins, "Correlation of finite element and modal test studies of a practical structure," in *Proceedings of the 2nd International Modal Analysis Conference*, pp. 156–162, Orlando, Fla, USA, February 1984.
- [26] D. J. Ewins, J. He, and N. A. J. Lieven, "A review of the error matrix method (EMM) for structural dynamic model comparison," in *Proceedings of the ESA Symposium on the Applications of Advanced Structural Materials*, Noordwijk, The Netherlands, 1988.
- [27] J.-S. Fuh and A. Berman, "Comment on 'Stiffness matrix adjustment using mode data,'" *AIAA Journal*, vol. 24, no. 8, pp. 1405–1406, 1986.
- [28] A. Berman, "Mass matrix correction using an incomplete set of measured modes," *AIAA Journal*, vol. 17, no. 10, pp. 1147–1148, 1979.
- [29] R. J. Guyan, "Reduction of stiffness and mass matrices," *AIAA Journal*, vol. 3, no. 2, p. 380, 1965.
- [30] D. J. Ewins, *Modal Testing: Theory, Practice and Application*, Research Studies Pre, 2000.
- [31] G. Heo, J. Jeon, C. O. Lee, G. Lee, and W. Lee, "FE model updating for health monitoring of structures and its experimental verification by damage detection," *Key Engineering Materials*, vol. 321–323, pp. 268–272, 2006.

## Research Article

# Vibration Effects of Nonclassically Damped Building-Piping Systems Subjected to Extreme Loads

YongHee Ryu,<sup>1</sup> WooYoung Jung,<sup>2</sup> and BuSeog Ju<sup>1</sup>

<sup>1</sup>Department of Civil Engineering, North Carolina State University, Raleigh, NC 27695, USA

<sup>2</sup>Department of Civil Engineering, Gangneung-Wonju National University, Gangneung 210-702, Republic of Korea

Correspondence should be addressed to BuSeog Ju; [bju2@ncsu.edu](mailto:bju2@ncsu.edu)

Received 22 September 2015; Accepted 30 December 2015

Academic Editor: Salvatore Russo

Copyright © 2016 YongHee Ryu et al. This is an open access article distributed under the Creative Commons Attribution License, which permits unrestricted use, distribution, and reproduction in any medium, provided the original work is properly cited.

Piping leakage can occur at T-joint, elbows, valves, or nozzles in nuclear power plants and nonnuclear power plants such as petrochemical plants when subjected to extreme loads and such leakage of piping systems can also lead to fire or explosion. For example, leakage of sodium, toxic gases, or nitrogen in hospitals can cause man-made hazards. The primary objective of this research is to understand the vibration effects due to classical/nonclassical damping with building-piping systems under extreme loads. The current evaluation employed finite-element analysis to calculate the effects of the responses of classically and nonclassically damped building-piping systems. Classical and nonclassical damping matrices for a coupled primary-secondary system were developed based on the Rayleigh equation. A total of 10 selected ground motions were applied to single degree of freedom (SDOF) primary-SDOF secondary (2-DOF coupled) systems in which the ratios of the natural frequencies between the primary and secondary systems ranged between 0.9 and 1.1. It revealed that the vibration effect of nonclassical damping was significant where the natural frequencies of the two systems were nearly tuned. For piping-material nonlinearity, the effects of nonclassical damping on the result forces of piping systems were not significantly different from those of classical damping.

## 1. Introduction

The vibration of a piping system is significantly influenced by the building in which it is installed, owing to the fact that, typically for such systems, the secondary structure is coupled with the primary structure. The individual components of piping systems and their overall structural integrity are critical to risk management and the continued safe operation of critical facilities such as hospitals and nuclear power plants during extreme loads such as blasts or earthquakes, most especially so as to avoid potential shutdowns. As seen in the recent sequence of events at the Fukushima Daiichi Nuclear power plant in 2011, keeping the core of the reactor cool by long-duration circulation of coolants is a necessity, even after a plant has been shut down due to an earthquake. A piping-system or individual-component failure can result in the loss of the capacity to circulate coolant, which, in turn, can increase the risk of the release of radioactivity. Furthermore, leakage of liquid coolant such as sodium in

fast breeder reactor can trigger the internal fires and leakage of oxygen or other gases initiated from piping systems in a hospital can result in fire hazards or explosions [1]. For a typical medium-sized hospital, nonstructural components account for fully 85% of the total construction cost (structural components: 15%), of which portion mechanical, electrical, and piping systems make up 35%, as illustrated in Figure 1 [2]. It has been reported that nonstructural damage, and its results, is the cause of approximately \$6.3 billion worth of economic loss [3]. Consequently, many engineers have recognized the significance of nonstructural components and the importance of ensuring that they remain operational, functional, and safe after an earthquake.

In the past, calculating the structural response of nonclassically damped systems using uncoupled primary and secondary modal properties was more convenient than calculating the response using completely coupled primary-secondary systems, for example, the studies of the uncoupled primary and secondary systems conducted to evaluate the

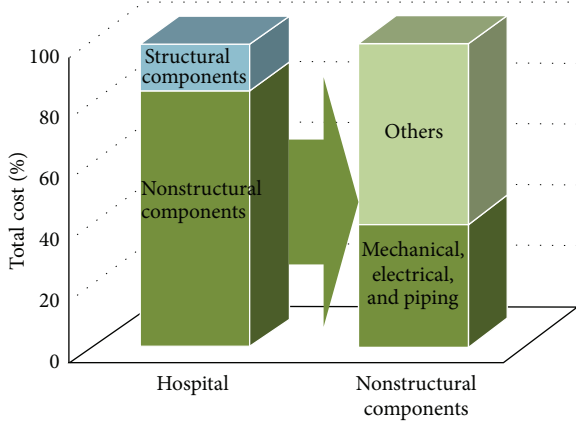


FIGURE 1: Construction costs of medium-sized hospital building.

response of nonclassically damped systems using response spectrum at the base of a primary structure [4, 5]. The assumptions made (e.g., representation of ground motion using Gaussian process models) in developing their formulations, however, led to inaccurate outputs in the low- or high-frequency range. Gupta [6] pointed out that the calculated vibrations of a coupled primary-secondary system were more comprehensive and accurate than those obtained from uncoupled systems. Moreover, Gupta [7] demonstrated that the effect of nonclassical damping is significant when uncoupled systems are (nearly) tuned and when the modal mass ratios are sufficiently small. Furthermore, in recent years, many researchers have recognized the need to control the excessive behavior under seismic ground motions, in order to reduce the seismic damage or system drift of structural and nonstructural components [8–13].

Consequently, this paper reports the results of an evaluation of the vibrations of classical and nonclassical damping for coupled primary-secondary systems including material nonlinearity. Finite-element building-piping models derived from the Open System for Earthquake Engineering Simulation (OpenSees) [14] were used to carry out the Rayleigh equation to develop classical and nonclassical damping matrices for a 2-DOF coupled primary-secondary system. A total of 10 ground motions originally proposed by the ATC-63 project (publication: *FEMA P695* [15]) as extreme loading conditions were selected for this study. A numerical model was developed for direct-integration time-history analyses of each ground motion case. The piping models included the effects of piping nonlinearity due to piping components' nonlinear behaviors. The effect of the mass ratio between building and piping systems also was studied.

## 2. Analysis of Primary and Secondary Systems

Piping systems installed in typical hospitals or office buildings are comprised of main-pipe lines, piping branches, and supports. An equivalent 2-degree of freedom (DOF) coupled (SDOF primary-SDOF secondary) system is shown in Figure 2. The diagram represents the piping subsystem in a building in which the mass of the frame is assumed to

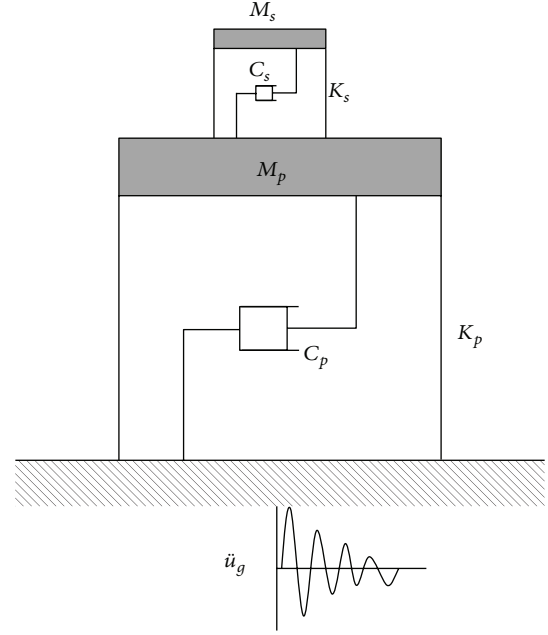


FIGURE 2: SDOF building-SDOF piping system.

be concentrated at the floor levels or main piping lines, and the floor beams or branches are assumed to be rigid, with the story stiffness provided by the flexure of the columns or piping supports. The typical values of the modal mass ratios in actual building-piping systems are on the order of 0.0001 or lower [16].

**2.1. Equation of Motion for Coupled System.** The equation of motion for an N-DOF coupled primary-secondary system can be written as follows:

$$M\ddot{U} + C\dot{U} + KU = -M\ddot{u}_g(t), \quad (1)$$

where  $M$  is the mass matrix,  $C$  is the damping matrix,  $K$  is the stiffness matrix,  $U$  is the displacement vector with respect to the fixed base, and  $u_g$  is the ground acceleration.

These matrices and vectors can be expressed in terms of the matrices and vectors of the primary and secondary systems:

$$\begin{aligned} M &= \begin{bmatrix} M_p & 0 \\ 0 & M_s \end{bmatrix}, \\ C &= \begin{bmatrix} C_p + C_p^s & C_{ps} \\ C_{sp} & C_s \end{bmatrix}, \\ K &= \begin{bmatrix} K_p + K_p^s & K_{ps} \\ K_{sp} & K_s \end{bmatrix}, \\ U &= \begin{Bmatrix} U_p \\ U_s \end{Bmatrix}, \end{aligned} \quad (2)$$

where those matrices and vectors are denoted by subscripts  $p$  and  $s$ , respectively, and the matrices  $K_p^s$  and  $C_p^s$  are the

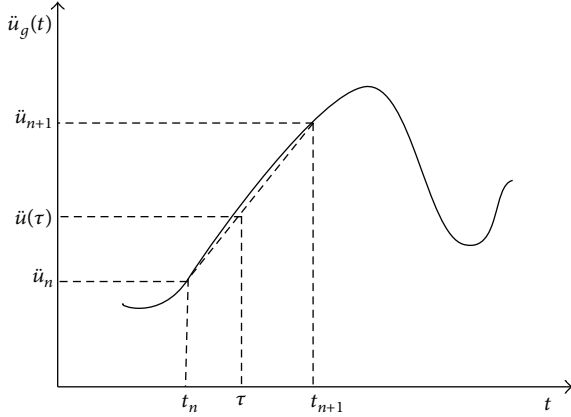


FIGURE 3: Linear representation of acceleration  $\ddot{u}(\tau)$ .

stiffness and damping contributions of the secondary system to the connected degrees of freedom in the primary system.

Direct integration of the equation of motion into the time-history analysis enables calculation of the system responses at discrete, usually equally apportioned intervals of time. As seen in (1), displacement, velocity, and acceleration are the basic computation parameters for determination of structural response. The integration algorithms are based on appropriate expressions selected for their relation of the response parameters at the given intervals of time to their historic values.

If the acceleration function in terms of force is represented by a series of straight lines, precise formulations for integration of the equation of motion can be developed in a linear system. With due consideration of the time-dependent acceleration  $\ddot{u}(\tau)$ , the variation of acceleration with time can reasonably be assumed to be linear (shown by the dashed line in Figure 3) when a sufficiently small interval of time  $\Delta t$  is used. With the origin location at time  $\tau$ ,  $\ddot{u}(\tau)$  can be written as follows:

$$\ddot{u}(\tau) = \ddot{u}_n + \frac{\ddot{u}_{n+1} - \ddot{u}_n}{t_{n+1} - t_n} \tau. \quad (3)$$

Using this equation's acceleration function in terms of force, the equation of motion for an N-DOF coupled primary-secondary system can be solved.

**2.2. Classical and Nonclassical Damping Matrices.** The response of the primary system is dominated by the first-mode frequency of the 2-DOF coupled system, and the response of the secondary system is dominated by the second-mode frequency. Therefore, a classical damping matrix for a 2-DOF coupled system can be evaluated using the Rayleigh equation:

$$[C_{cl}] = \alpha \begin{bmatrix} M_p & 0 \\ 0 & M_s \end{bmatrix} + \beta \begin{bmatrix} K_p + K_s & -K_s \\ -K_s & K_s \end{bmatrix}, \quad (4)$$

where

$$\alpha = \frac{2\omega_i\omega_j}{\omega_j^2 - \omega_i^2} (\omega_j\xi_p - \omega_i\xi_s), \quad (5)$$

$$\beta = \frac{2}{\omega_j^2 - \omega_i^2} (\omega_j\xi_s - \omega_i\xi_p).$$

The transformed damping matrix  $\bar{C}$  for the coupled system is

$$\bar{C} = \phi^T C \phi. \quad (6)$$

Using (4) to (6), the transformed damping matrix  $\bar{C}_{cl}$  for a 2-DOF coupled system is always classical, which is to say, the off-diagonal terms are zeros. The nonclassical damping matrix for a 2-DOF coupled system also can be evaluated using the Rayleigh equation

$$[C_p] = \alpha_p \begin{bmatrix} M_p & 0 \\ 0 & 0 \end{bmatrix} + \beta_p \begin{bmatrix} K_p & 0 \\ 0 & 0 \end{bmatrix},$$

$$[C_s] = \alpha_s \begin{bmatrix} 0 & 0 \\ 0 & M_s \end{bmatrix} + \beta_s \begin{bmatrix} K_s & -K_s \\ -K_s & K_s \end{bmatrix}, \quad (7)$$

$$[C_{nc}] = [C_p] + [C_s],$$

where  $\alpha_p$  and  $\beta_s$  are calculated as

$$\alpha_p = \frac{2\omega_i\omega_j}{\omega_j^2 - \omega_i^2} (\omega_j\xi_p - \omega_i\xi_p),$$

$$\beta_p = \frac{2}{\omega_j^2 - \omega_i^2} (\omega_j\xi_p - \omega_i\xi_p),$$

$$\alpha_s = \frac{2\omega_i\omega_j}{\omega_j^2 - \omega_i^2} (\omega_j\xi_s - \omega_i\xi_s),$$

$$\beta_s = \frac{2}{\omega_j^2 - \omega_i^2} (\omega_j\xi_s - \omega_i\xi_s). \quad (8)$$

Since the damping ratio between the primary system and the secondary system is not the same, the transformed damping matrix  $\bar{C}_{nc}$  is nonclassical, or, in other words, the off-diagonal terms are nonzero.

### 3. Ground Motion and Response Spectra

In order to evaluate classically and nonclassically damped coupled primary-secondary systems, a total of 10 ground motions originally proposed by the ATC-63 project, published as *FEMA P695* [15], were selected in this study. The records correspond to earthquakes resulting from a variety of fault mechanisms including normal, reverse, and strike-slip fault. The local condition for each record was considered to be either site class C or D, and no more than two records were selected for a single earthquake. Table 1 lists the detailed characteristics of the ground motion records. As is indicated, the data were recorded in the US, Turkey, Iran,

TABLE 1: Details of selected ground motions.

Number	Date	Event	Location	Magnitude ( $M_w$ )	Dt (s)
1	08/17 1999	Kocaeli	Arcelik, Turkey	7.5	0.01
2	10/16 1999	Hector Mine	Hector, USA	7.1	0.01
3	10/15 1979	Imperial Valley	Delta, USA	6.5	0.005
4	08/17 1999	Kocaeli	Duzce, Turkey	7.5	0.01
5	09/20 1999	Chi-Chi	Tcu045, Taiwan	7.6	0.02
6	06/20 1990	Manjil	Manjil, Iran	7.4	0.005
7	01/17 1994	Northridge	Beverly Hills, USA	6.7	0.01
8	04/25 1992	Cape Mendocino	Rio Dell Overpass Pf, USA	7.0	0.005
9	10/18 1989	Loma Prieta	Gilroy Array, USA	6.9	0.005
10	11/12 1999	Duzce	Bolu, Turkey	7.1	0.01

and Taiwan. The earthquake magnitude was greater than 6.0  $M_w$  in every case, and the range of peak ground accelerations (PGA) was 0.210 g–0.822 g. To investigate the effect of the frequency tunings between two systems, linear and nonlinear time-history analyses were conducted using building-piping models subjected to the 10 different ground motions. For that purpose, the ground motions were first normalized to a given value of PGA (see Figure 4), so that the effect of the tuning for the different ground motions could be indicated more clearly. Figure 5 plots the response spectra of the total ground motions.

#### 4. Classical and Nonclassical Damping in Coupled System

Linear and nonlinear direct-integration time-history analyses were performed using SDOF primary-SDOF secondary (2-DOF coupled) finite-element models subjected to each normalized ground motion. The different ratios of the natural frequencies or masses between the primary and secondary systems were considered.

##### 4.1. Response Using Classical or Nonclassical Damping Matrix.

For the uncoupled primary and secondary systems, the masses  $M_p = 90.7$  kg and  $M_s = 0.00907$  kg, respectively, were considered. The damping ratios for the primary and secondary systems were  $\xi_p = 5\%$  and  $\xi_s = 2\%$ , respectively. In general, the 5% damping ratio represents concrete material, and the 2% damping ratio, steel material. To represent the

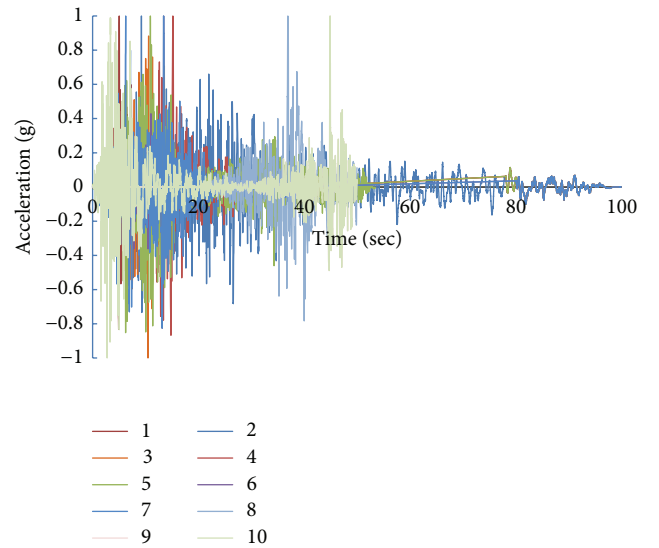


FIGURE 4: Normalized ground motions.

respective stiffness of the primary and secondary systems,  $K_p = 10,205$  N/mm and  $K_s = 0.827$ – $1.235$  N/mm were applied, and the frequencies were nearly tuned with  $f_p = 2.717$  Hz and  $f_s = 2.978$ – $2.988$  Hz. To further illustrate the significance of nonclassical damping, a parametric study was conducted using SDOF primary-SDOF secondary (2-DOF coupled) systems and varying the tuning between their frequencies within the 0.9–1.1 range. Figure 6 shows the differences in the

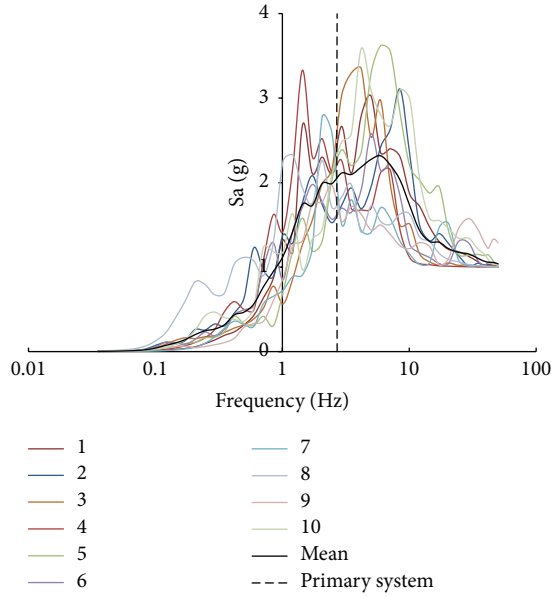


FIGURE 5: Response spectra.

TABLE 2: Result forces for secondary system in case of  $f_s/f_p = 1.0$ .

Number	Force (N)
1	552.92
2	448.71
3	1117.07
4	424.80
5	758.64
6	341.06
7	520.78
8	350.02
9	470.27
10	926.48

secondary-system result forces obtained from the nonclassical and classical damping matrices for different frequency-ratio values: specifically, the ratios of secondary to primary system frequency for each ground motion. As seen in the figure, the effect of nonclassical damping was significant only in the systems that had nearly tuned modes. Table 2 lists the result forces for the secondary systems subjected to ground motions.

#### 4.2. Responses of Two Systems Including Material Nonlinearity.

A nonlinear finite-element model for a piping system was developed using OpenSees [17] and a hysteretic material model. The hysteretic behavior of the piping component was characterized by the basic parameters: yield strength  $F_y$ , initial stiffness  $k_1$ , and hardening stiffness  $k_2$ , as shown in Figure 7, and *elasticbeamcolumn* element given in Table 3 was also used in OpenSees. Typically, the material property of the piping systems derived from the yield strength was defined by its initial stiffness  $k_1$ , listed in Table 4. Figure 8 plots the result forces of the vibrations for classically or

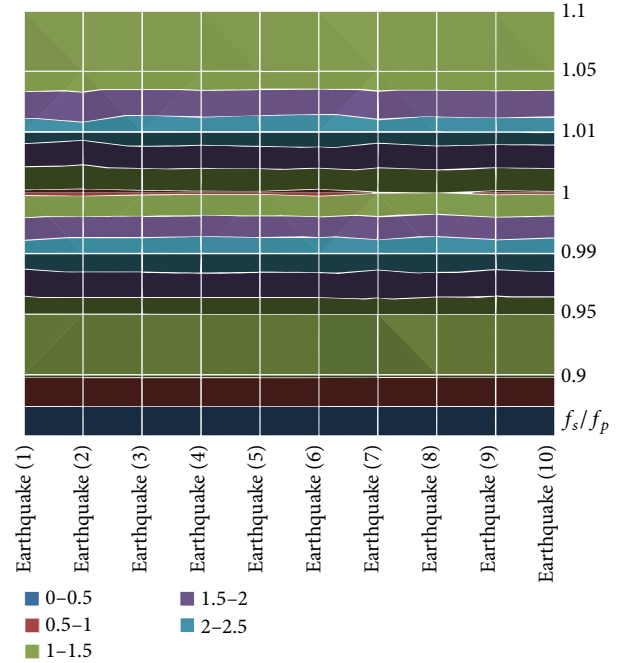


FIGURE 6: Differences in scale of 2-DOF coupled system.

nonclassically damped coupled primary-secondary systems including piping-material nonlinearity. The PGA for the first ground motion, as multiplied by 0.1, was selected for this study. As indicated in the figure, the result forces in the range of  $f_s/f_p < 1.05$ , between the classically and nonclassically damped systems, did not show significant differences using the nonlinear piping system. Even if the  $f_s/f_p$  was greater than 1.00, the result forces between the classically and nonclassically damped systems again showed no significant differences. This was due to the fact that the piping system still remained in the elastic range (see Figure 7). It should be noted that the displacements of the piping system in the nonlinear range showed differences due to the nature of the nonlinear material behavior, even when the result forces with respect to the piping nonlinearity were very close.

#### 4.3. Effect of Mass Ratios for Nonlinear Piping Systems.

Gupta (1999) earlier found that the effect of nonclassical damping was significant when the modal mass ratios of coupled primary-secondary systems were sufficiently small and those systems remained in the linear elastic range. Figure 9 shows the differences between nonclassical damped systems and classically damped systems for a linear building-piping system as well as a linear building system and a nonlinear piping system. The effect of nonclassical damping was significant when the mass ratios between the primary-secondary systems were on the order of 0.0001 or lower. However, if the piping system was in the nonlinear range, the differences in the result forces were significantly reduced. Next, the vibration effect of between classically/nonclassically damped coupled primary-secondary systems subjected to ground motions will be discussed.

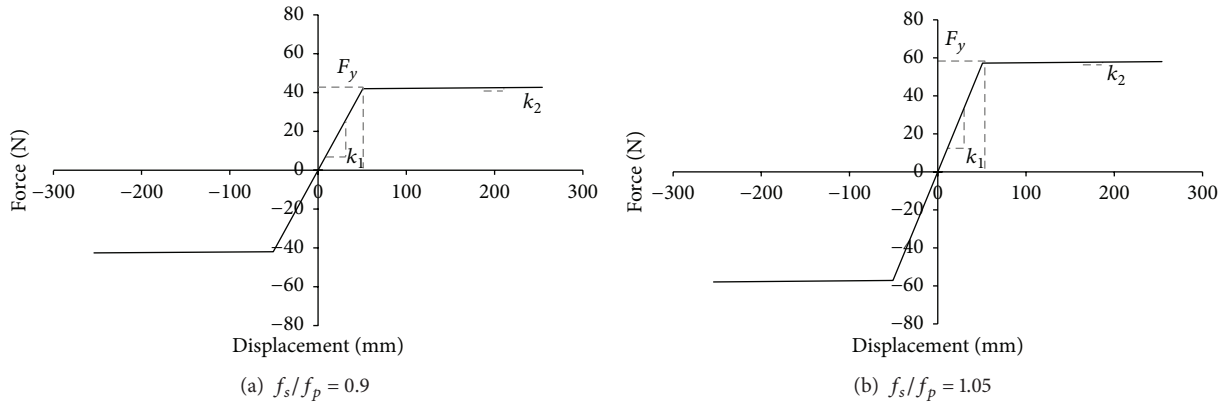


FIGURE 7: Nonlinear material behavior for piping system.

TABLE 3: Definition of the *elasticbeamcolumn* element parameters in OpenSees (after Mazzoni et al., 2006 [17]).

Parameters	Definitions
\$eleTag	Unique element object tag
\$iNode \$jNode	End nodes
\$A	Cross-sectional area of element
\$E	Young's modulus
\$G	Shear modulus
\$J	Torsional moment of inertia of cross section
\$Iz	Second moment of area about the local z-axis
\$Iy	Second moment of area about the local y-axis
\$transfTag	Identifier for previously defined coordinate-transformation object

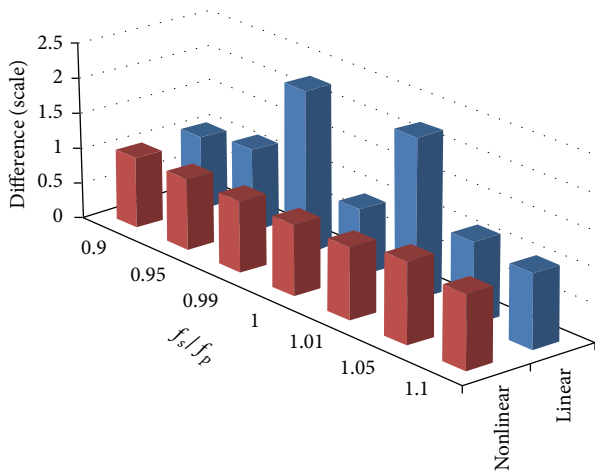


FIGURE 8: Linear versus nonlinear responses of piping system.

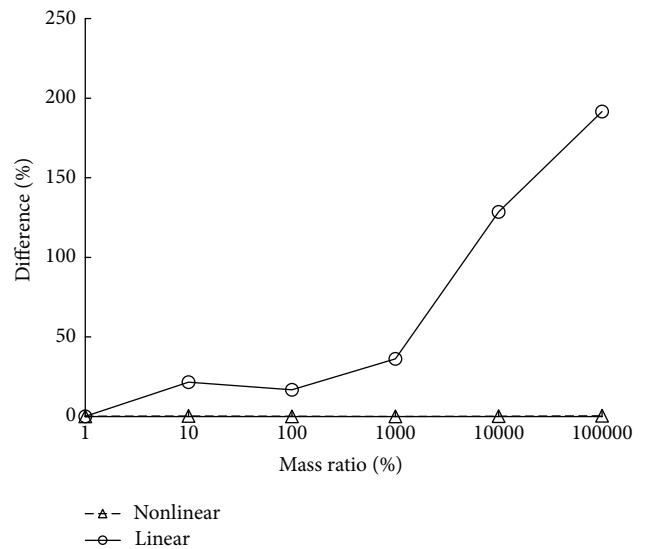


FIGURE 9: Difference between linear and nonlinear models with respect to mass ratio.

### 5. Vibration Attenuation of Building-Piping System under Seismic Ground Motions

For vibration control of the building-piping system, the relative effectiveness of the classical and nonclassical damping system was considered in this study. In particular, five simulations corresponding to the different frequency ratio between the systems were carried out to measure the

acceleration time histories at the top floor of the system. A vibration comparison between classical and nonclassical damped systems conducted in OpenSees was described in Figure 10. Also, it showed the quantitative comparison of the acceleration capacities of the systems. It can be seen

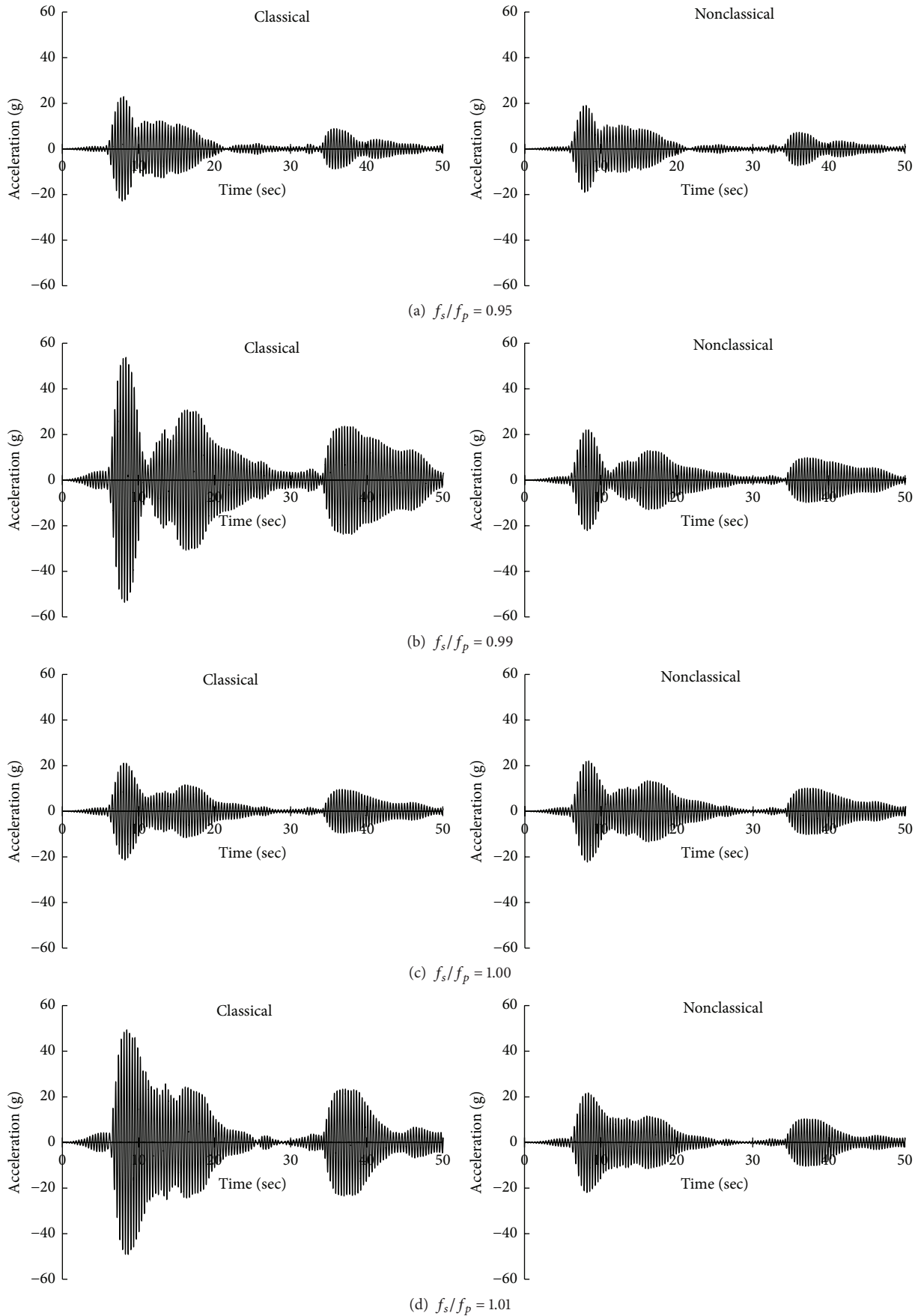


FIGURE 10: Continued.

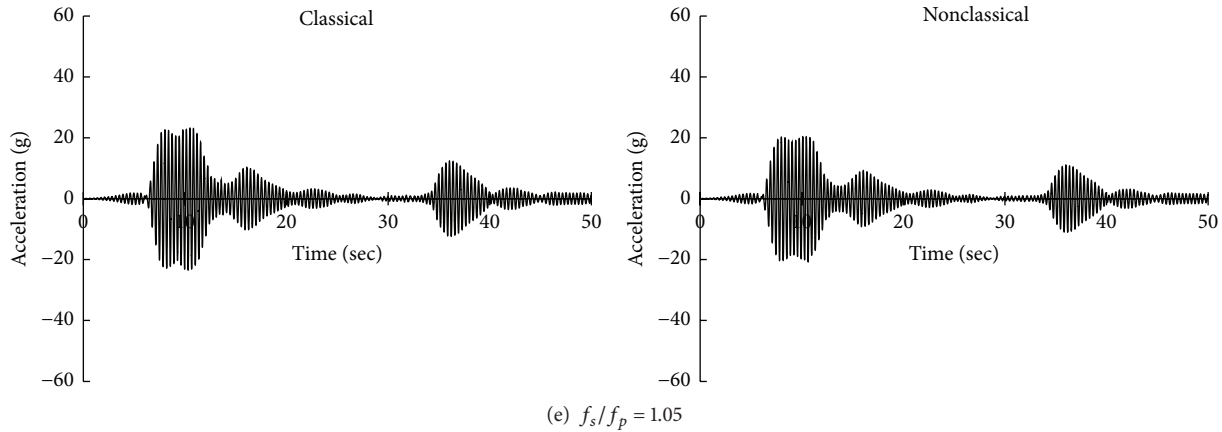


FIGURE 10: Acceleration time histories with different frequencies in classically and nonclassically damped coupled building-piping systems.

TABLE 4: The parameters of coupled building-piping systems.

Parameter	$f_s/f_p = 0.9$	$f_s/f_p = 1.05$
$F_y$	42 N	57 N
$k_1$	826.61 N/m	1125.11 N/m
$k_2$	8.26 N/m	11.25 N/m

that there was a similar manner in all of the acceleration time histories: nonclassical damped building-piping system was more conservative than classical coupled building-piping system, in terms of reducing the floor accelerations through the ground acceleration using the 1999 Chi-Chi earthquake. Furthermore, the nonclassical damped system showed the vibration attenuation about 20% with 0.95, 0.99, and 1.05 frequency ratios. In terms of frequency ratios—0.99 and 1.01, however, the vibration attenuation was significantly influenced by nonzero off-diagonal term, resulting in a decrease of more than 50%. Consequently, the vibration of the coupled building-piping system was sensitive to the mechanical properties such as mass and stiffness ratio of the primary and secondary system.

## 6. Conclusions

The present study evaluated the effects of the seismic responses of classically and nonclassically damped coupled primary-secondary piping systems, including nonlinearity behavior. A finite-element building-piping model using OpenSees was employed to develop, using the Rayleigh equation, classical and nonclassical damping matrices for a 2-DOF coupled primary-secondary system. A total of 10 selected ground motions were applied to SDOF primary-SDOF secondary (2-DOF coupled) systems in which the ratios of the natural frequencies between the primary and secondary systems ranged between 0.9 and 1.1. Linear and nonlinear direct-integration time-history analyses were performed for each ground motion case. It was shown that the effect of nonclassical damping was significant in systems that have nearly tuned modes. For piping-material nonlinearity,

the effects of nonclassical damping on the result forces of the piping system were not significantly different from those of classical damping. In fact, they were insignificant, even though the modal mass ratios were sufficiently small. However, it should be noted that, even when the result forces are very close, piping-system displacements in the nonlinear range can show differences due to the nature of nonlinear material behavior. Additionally, in the simulations using classically and nonclassically damped systems, it was interesting to find that nonzero off-diagonal term in nonclassical damping matrices was very effective to the vibration attenuation, especially, coupled building-piping system with frequency range of 0.95 to 1.05. Also, the probabilistic risk assessment of coupled building-piping systems as the analysis of the vibration attenuation must be achieved, in order to evaluate the probability of failure with respect to material uncertainty and ground motion uncertainty using classical and nonclassical damping matrices.

## Conflict of Interests

The authors declare that there is no conflict of interests regarding the publication of this paper.

## Acknowledgment

This work was supported by a National Research Foundation of Korea (NRF) grant funded by the Korean government (MEST) (no. 2012-0008762).

## References

- [1] Y. H. Ryu, A. Gupta, B. S. Ju, and W. Y. Jung, "A framework for evaluating the probability of fire hazard due to leakage of liquid coolant in fast breeder reactor," in *Proceedings of the 23rd International Conference on Structural Mechanics in Reactor Technology Conference (SMiRT '15)*, Manchester, UK, August 2015.
- [2] FEMA 577, *Risk Management Series Design Guide for Improving Hospital Safety in Earthquakes, Floods, and High Winds*, Federal Emergency Management Agency, Washington, DC, USA, 2007.

- [3] C. A. Kircher, "It makes dollars and sense to improve nonstructural system performance," in *Proceedings of the Seminar on Seismic Design, Performance, and Retrofit of Nonstructural Components in Critical Facilities*, ATC-29-2, pp. 109–120, Newport Beach, Calif, USA, October 2003.
- [4] M. P. Singh and S. L. Chu, "Stochastic considerations in seismic analysis of structures," *Earthquake Engineering and Structural Dynamics*, vol. 4, no. 3, pp. 295–307, 1976.
- [5] R. Villavarde and N. M. Newmark, "Seismic response of light attachments to buildings," Structural Research Series no. 469, University of Illinois, Urbana, Ill, USA, 1980.
- [6] A. K. Gupta, *Response Spectrum Method in Seismic Analysis and Design of Structures*, CRC Press, Boca Raton, Fla, USA, 1992.
- [7] A. Gupta, "Significance of nonclassical damping in coupled system analysis," in *Proceedings of the 15th Structural Mechanics in Reactor Technology Conference (SMiRT '99)*, Seoul, Republic of Korea, August 1999.
- [8] K. Park, D. Kim, D. Yang, J. Daeki, I. Ha, and S. Kim, "A comparison study of conventional construction methods and outrigger damper system for the compensation of differential column shortening in high-rise buildings," *International Journal of Steel Structures*, vol. 10, no. 4, pp. 317–324, 2010.
- [9] S. Aghajanian, H. Baghi, F. Amini, and M. Z. Samani, "Optimal control of steel structures by improved particle swarm," *International Journal of Steel Structures*, vol. 14, no. 2, pp. 223–230, 2014.
- [10] S.-H. Oh, S.-H. Song, S.-H. Lee, and H.-J. Kim, "Seismic response of base isolating systems with U-shaped hysteretic dampers," *International Journal of Steel Structures*, vol. 12, no. 2, pp. 285–298, 2012.
- [11] D.-H. Shin and H.-J. Kim, "Probabilistic assessment of structural seismic performance influenced by the characteristics of hysteretic energy dissipating devices," *International Journal of Steel Structures*, vol. 14, no. 4, pp. 697–710, 2015.
- [12] C. F. Ma, Y. H. Zhang, P. Tan, and F. L. Zhou, "Seismic response of base-isolated high-rise buildings under fully nonstationary excitation," *Shock and Vibration*, vol. 2014, Article ID 401469, 11 pages, 2014.
- [13] D. Foti, "On the seismic response of protected and unprotected middle-rise steel frames in far-field and near-field areas," *Shock and Vibration*, vol. 2014, Article ID 393870, 11 pages, 2014.
- [14] OpenSees, "Open System for Earthquake Engineering Simulation," 2006, <http://opensees.berkeley.edu/>.
- [15] FEMA P695, *Quantification of Building Seismic Performance Factors*, Federal Emergency Management Agency, Washington, DC, USA, 2009.
- [16] M. K. Bose, *Non-classical damping properties and modal correlation coefficient for dynamic analysis of structures [Ph.D. thesis]*, North Carolina State University, Raleigh, NC, USA, 2001.
- [17] S. Mazzoni, F. McKenna, M. H. Scott, and G. L. Fenves, "OpenSees command language manual," 2006, <http://opensees.berkeley.edu/>.

## Research Article

# Structural Performance Assessment Based on Statistical and Wavelet Analysis of Acceleration Measurements of a Building during an Earthquake

Mosbeh R. Kaloop,<sup>1,2</sup> Jong Wan Hu,<sup>1,3</sup> Mohamed A. Sayed,<sup>4</sup> and Jiyoung Seong<sup>5</sup>

<sup>1</sup>Department of Civil and Environmental Engineering, Incheon National University, Incheon 406-840, Republic of Korea

<sup>2</sup>Department of Public Works and Civil Engineering, Mansoura University, Mansoura 35516, Egypt

<sup>3</sup>Incheon Disaster Prevention Research Center, Incheon National University, Incheon 406-840, Republic of Korea

<sup>4</sup>National Research Institute of Astronomy and Geophysics, Cairo 11421, Egypt

<sup>5</sup>National Disaster Management Institute, Ministry of Security and Public Administration, Seoul 121-719, Republic of Korea

Correspondence should be addressed to Jong Wan Hu; [jongp24@incheon.ac.kr](mailto:jongp24@incheon.ac.kr)

Received 3 September 2015; Accepted 21 October 2015

Academic Editor: Guillermo Rus

Copyright © 2016 Mosbeh R. Kaloop et al. This is an open access article distributed under the Creative Commons Attribution License, which permits unrestricted use, distribution, and reproduction in any medium, provided the original work is properly cited.

This study introduces the analysis of structural health monitoring (SHM) system based on acceleration measurements during an earthquake. The SHM system is applied to assess the performance investigation of the administration building in Seoul National University of Education, South Korea. The statistical and wavelet analysis methods are applied to investigate and assess the performance of the building during an earthquake shaking which took place on March 31, 2014. The results indicate that (1) the acceleration, displacement, and torsional responses of the roof recording point on the top floor of the building are more dominant in the  $X$  direction; (2) the rotation of the building has occurred at the base recording point; (3) 95% of the energy content of the building response is shown in the dominant frequency range (6.25–25 Hz); (4) the wavelet spectrum illustrates that the roof vibration is more obvious and dominant during the shaking; and (5) the wavelet spectrum reveals the elasticity responses of the structure during the earthquake shaking.

## 1. Introduction

Investigating the adequate and accurate performance of the structure at each stage of its life cycle is essential for elongating the life time of the structure. Based on analyses results, appropriate structural repairs and antiseismic retrofit methods can be planned. Moreover, applying various instrumental measurements in the structural health monitoring system is useful to decision makers [1].

Monitoring the performance of different types of structures is not widely employed in South Korea. Thus, the National Disaster Management Institute (NDMI) in South Korea targets to widely spread using the various structural performance tools in investigating and assessing the deformations of structures to mitigate the potential risk of conventional and inconvenient structures all around Korea.

Furthermore, NDMI intends to obtain and develop a low cost monitoring system that will be able to improve the SHM of structures and to adequately increase the spread of the structural performance all around Korea. The improvement of monitoring tools aims also to develop data acquisition system and software that allow recording the structure responses to accurately and precisely obtain the structure deformations in near real-time [2].

The statistical analysis of the structural performance monitoring of structures is commonly used to test and assess the statistical modeling of buildings and statistical decision making for inferring the structure health state [3, 4]. Statistical time series methods for SHM are fundamentally of the inverse type [3, 5] and the structural decision making with specified performance characteristics. Kopsaftopoulos and Fassois [3] have introduced a study on the parametric

and nonparametric time series statistical methods which can be applied in SHM, where parametric time series statistical methods employ statistics based on parametric time series representation, while the nonparametric statistical methods employ statistics based on nonparametric representation [3, 5]. Fassois and Sakellariou [5] have summarized the time series statistical methods for the vibration of structures. Ding et al. [6] have applied the cross-correlation of SHM system to assess and predict the performance of bridge performance under different loads effects. Furthermore, they have found that the statistical analysis can detect the bridge abnormal performance under the varying environmental conditions. Kaloop et al. [7] and Kaloop and Hu [8] have applied a parametric model based on neural network to assess the performance of structures and for damage detection. They have found that the statistical analysis can be used in efficiently detecting the damage of structures.

Signal processing tools are used in amplitude and frequency analysis of the seismic waves velocities and of waves traveling paths within different soil layers with different properties [9]. The responses of structure under seismic loading are usually random and nonstationary. Therefore, they shall be preferably stochastically displayed using statistical time-varying techniques such as spectral density functions. The revolutionary wavelet analysis was shown to be a powerful signal processing tool [10].

Tibaduiza et al. [11] have illustrated and applied the principal component analysis and the wavelet analysis applications, related to statistical theory, in measuring the structural dynamic response signals and damage detection. Based on wavelet analysis, the statistical analysis of wavelet coefficients which are extracted from monitoring signals gave a representation that illustrates the energy distribution of the dynamic responses in time and frequency domains [11]. Dinh et al. [9] have demonstrated the seismic responses of a multispan structure based on wavelet analysis. They have found that the proposed wavelet analysis is a precise seismic tool for long span multisupport structures, since it accounts for the nonstationary in both amplitude and frequency of the excitations. In addition, it offers a realistic illustration of the energy content of the earthquake acceleration. Ali and Kim [12] have used wavelet analysis to analyze the seismic load effects of soil-structure-interaction on the base-isolated nuclear power plant. They have found that the wavelet analysis proves to be an efficient tool in investigating the effect of soil-structure-interaction on the frequency content of the acceleration response of base-isolated nuclear structure. Mollaioli and Bosi [13] have proposed the application of wavelet analysis on the seismic signals. They have found the construction of simplified signals containing the prominent features of the data distribution recorded from pulse-like earthquakes. Furthermore, many previous studies have applied the statistical and wavelet analysis in structural performance analysis and damage detection [14–17].

The proposed study aims to assess the structural performance of the administration building in Seoul National University of Education during an earthquake shaking. Moreover, investigating the structural performance is proposed based on a novel and simple application of nonparametric

TABLE 1: Acceleration sensor performance.

Parameter	Description
Amplitude	4 g pk
Sensitivity	2.5 to 20 V/g
Dynamic range	165 dB
Bandwidth	DC to 200 Hz
Amplitude linearity	<0.1%

TABLE 2: Data-logger performance.

Parameter	Description
Sampling rate	1~1000 Hz
Synchronized accuracy	4 ms
Resolution	24 bit
Size	29.6 × 17.5 × 14.0 (mm)

and parametric statistical methods and wavelet analysis. In addition, the assessment of the acceleration responses of the building is presented based on analyzing the wavelet energy content. Finally, checking the safety of the building and the low cost acceleration monitoring system efficiency are considered.

## 2. Building and SHM Description

The case study structure is the 7-storey main administrative building at Seoul National University of Education. It is a reinforced concrete building that consists of seven storeys with total height of 26.5 as shown in Figure 1. The structural system of the building consists of reinforced concrete frames and core. The building has extensions in all directions as shown in Figure 1(c). The components of the SHM system are illustrated in Figure 2. The recorded data are digitized in a 24-bit analog-to-digital converter and then sent through a Bluetooth module and access point. All measured data are collected and then stored in a secure digital memory. One-channel acquisition devices are used in this study, whereas each acquisition device is synchronized by a signal sender from a computer at each time. The accelerometer properties are demonstrated in Table 1, while the data-logger performance is illustrated in Table 2. The acceleration sensors are used with maximum amplitude of 4 g. All devices are put inside boxes to protect them from different weather conditions such as rain, snow, or wind, as shown in Figure 3.

The arrangements of the acceleration measurement points are shown in Figures 1 and 4. Three monitoring points are located to monitor the responses of the building. The free-field (ground) point is located on the landscape, which surrounds the building to measure the free-field seismic shaking. The ground sensor point is 13.26 m from the building, as shown in Figure 4(a). Two measurement points are located on the building, which are the base point and the roof point. The base point is fixed in the building basement floor, while the roof point is fixed in the building roof as illustrated in Figure 4.

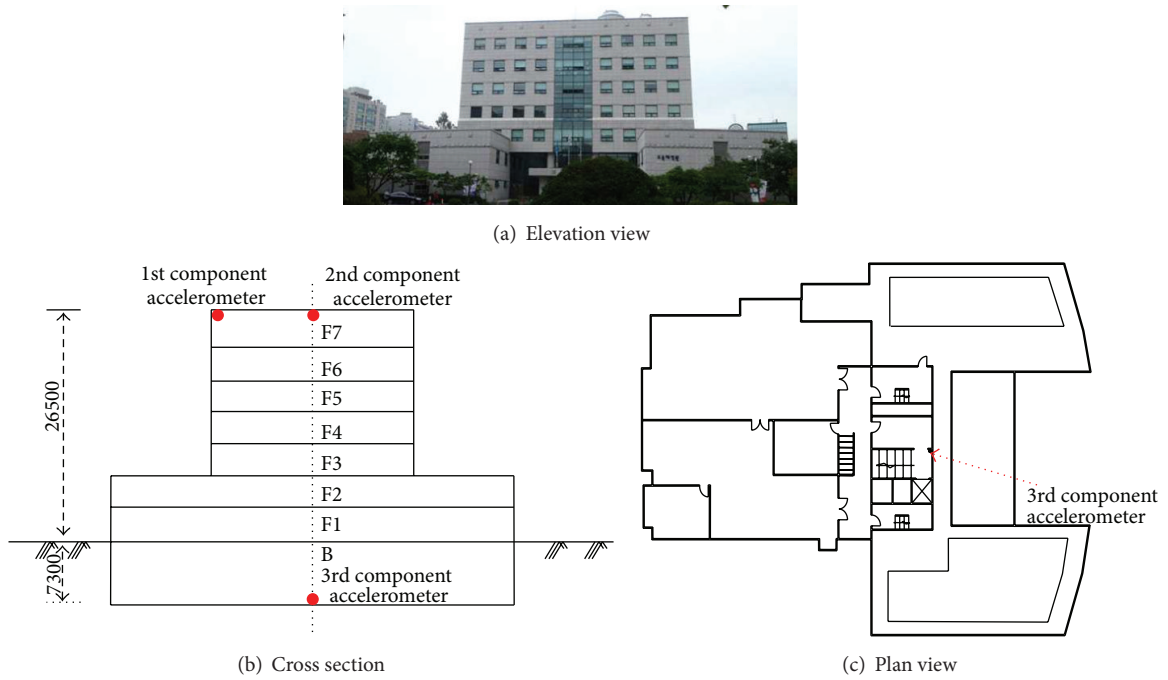


FIGURE 1: Administration building.

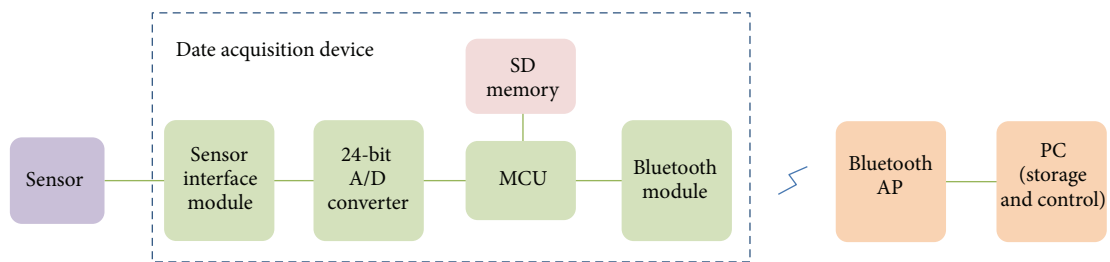


FIGURE 2: Structural monitoring system components.

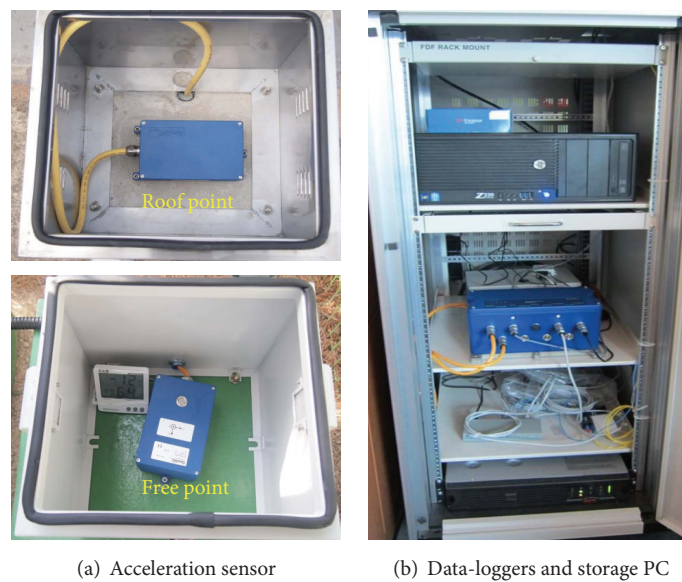


FIGURE 3: Experimental setting of acceleration sensors at measuring points and SHM components.

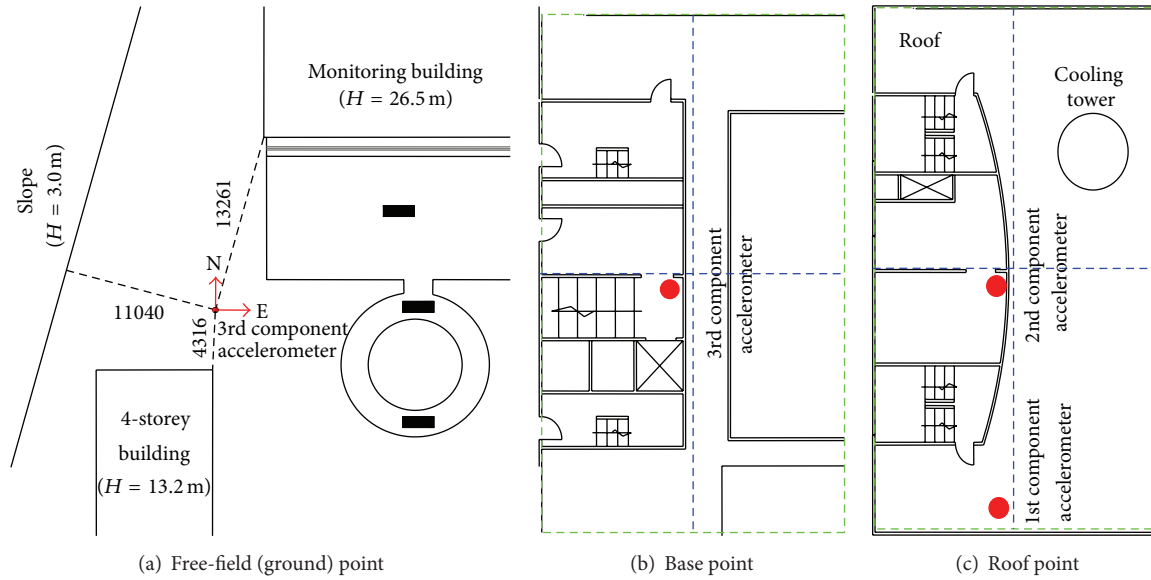


FIGURE 4: Monitoring points on the building.

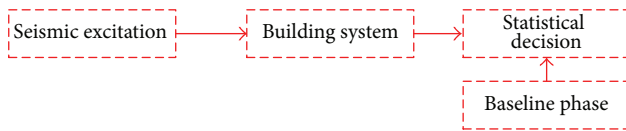


FIGURE 5: Scheme of the statistical decision of building.

### 3. Methodology and Results Analysis

**3.1. Statistical Analysis.** The statistical structural performance studies are summarized and presented in [3, 4, 16–18]. In civil engineering, structures properties may suffer slight deterioration with time or complete damage during severe events. Figure 5 is sketched based on the statistical structural performance conclusions drawn from Fassois and Sakellariou [5] and Arangio and Bontempi [18]. Statistical analysis provides boundary limits for the structural performance changes, and it is applied as warning for possible damages [16]. The majority of previous studies have used the parametric statistical analysis to assess the performance of structures [1–3, 7, 19, 20]. Therefore, the novel application of nonparametric (ellipse errors and covariance) and parametric (linear fitting) statistical analyses are utilized in this study to investigate the structural performance of the case study structure.

The acceleration measurements in  $Y$  direction at the ground point before and during the earthquake event are shown in Figure 6. The acceleration measurements are considered noises before the earthquake event, which implies no effective or peak values during the observations before the earthquake. However, the peak acceleration exceeded 3 Gal ( $\text{cm}/\text{sec}^2$ ) during the earthquake as shown in Figure 6(b).

Figure 7 summarizes the peak acceleration of ground and roof points before and during the earthquake shaking. The maximum acceleration for the ground point was

0.64 Gal ( $\text{cm}/\text{sec}^2$ ) and 3.42 Gal before and during the earthquake, respectively, in  $Y$  direction, while it was 0.50 Gal and 2.83 Gal before and during the earthquake, respectively, along  $X$  direction. In addition, the maximum acceleration of the base point was 0.03 Gal and 1.18 Gal before and during the earthquake, respectively, in the  $X$  direction, while it was 0.03 Gal and 0.70 Gal before and during the earthquake, respectively, in  $Y$  direction. Furthermore, the maximum acceleration at the roof point was 0.04 Gal and 4.84 Gal in  $X$  direction and 0.05 Gal and 2.50 Gal in  $Y$  direction, before and during the earthquake, respectively.

Figure 7 illustrates the linear fitting between the peak acceleration responses of base and roof points, with the ground point in  $X$  and  $Y$  directions. In addition, Figure 7 demonstrates that the roof response linear fitting (TX and TY) with ground response (GX and GY) is shown to be greater than that for the base response (BX and BY) for the two directions. Moreover, it can be seen that the  $X$  direction responses have the lowest peak values and the highest linear slope. From the results, it can be presented that the slopes are smaller than one in  $X$  and  $Y$  direction for the base point and in  $Y$  direction for the roof point. Furthermore, the slope is shown to be greater than one for the roof point in the  $X$  direction. It indicates that the effective direction of the structural responses occurred in  $X$  direction during the earthquake shaking.

Figure 8 depicts the ellipse errors with confidence 95% for the relation between the ground and building responses. It can be noticed from Figure 8 that the ellipse errors for the roof responses are higher than for the base responses. Moreover, it can be shown that the angles between the  $x$ -axis and the largest eigenvector for the building base and roof responses are 3.1416 rad and 3.1412 rad before the earthquake, while they are 3.1414 rad and 1.5706 rad during the earthquake, in  $X$  and  $Y$  direction, respectively. It indicates that

TABLE 3: Maximum eigenvalues and eigenvectors for covariance shaking point response matrix.

Parameters	Base point		Roof point	
	X	Y	X	Y
Eigenvalue	0.0072	0.0084	0.0229	0.0119
Eigenvector	$[-1; 1.45e - 4]$	$[-1; 7.33e - 5]$	$[1.55e - 4; 1]$	$[7.24e - 4; 1]$

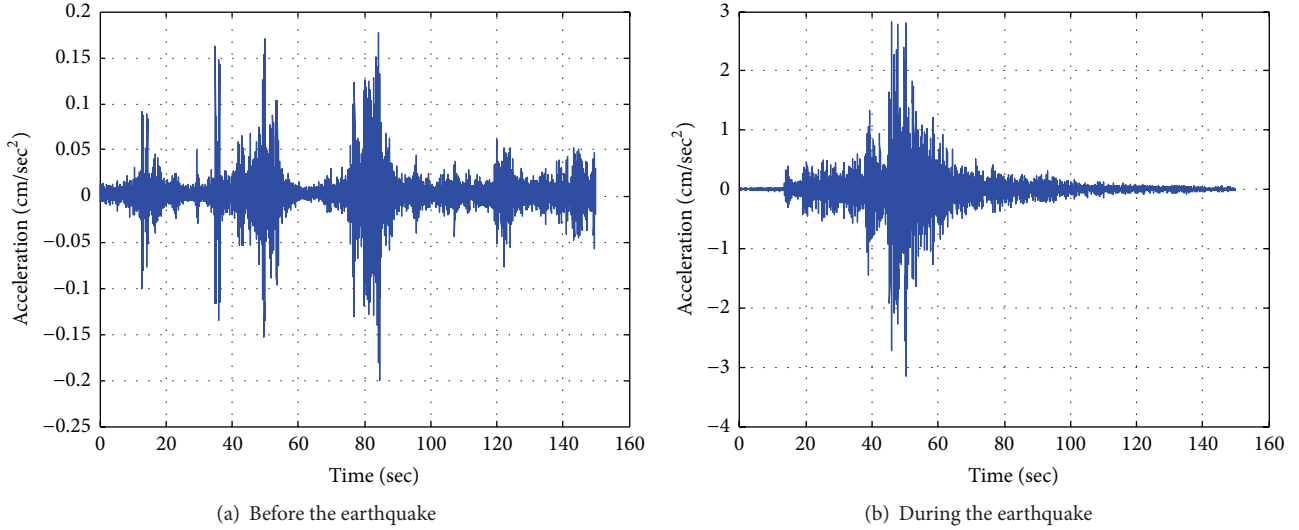


FIGURE 6: Acceleration response measurements at the ground point.

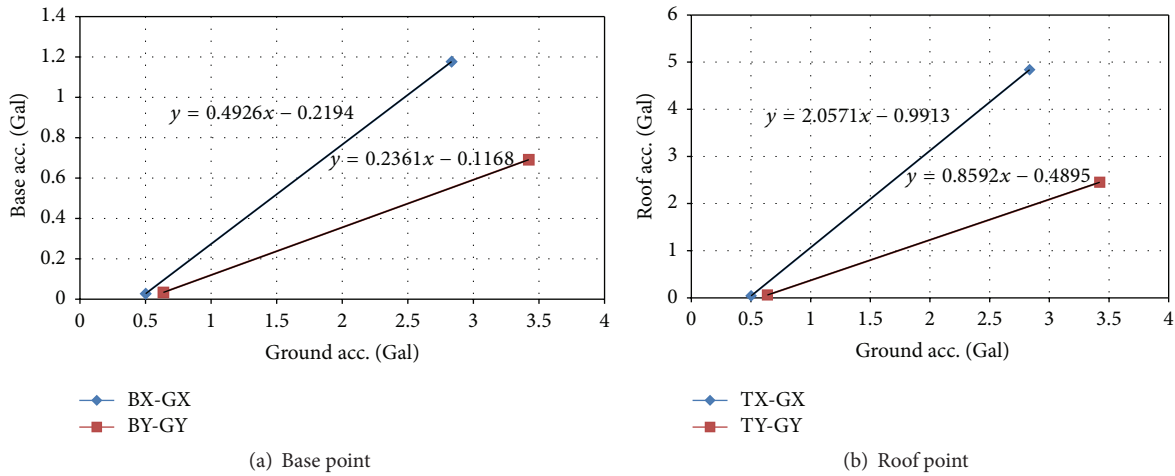


FIGURE 7: Linear fitting between the free-field response and the building different sensors responses.

the roof responses increased by 50% during the earthquake shaking for the two directions, while the base responses can be neglected during the shaking.

The covariance matrix of the base and roof acceleration responses is calculated with ground responses in X and Y directions. The results from the calculated covariance matrices show that the rotation occurred for the base point, while the hyperbolic rotation occurred for the roof point in the two directions. In addition, Table 3 illustrates the maximum eigenvalues and eigenvectors for the base and roof responses covariance matrices. From this table, it is shown that the roof

eigenvalues and eigenvector are greater than for the base in the two directions, which assure the higher responses for the roof point under the earthquake shaking. From the previous statistical analysis, it is concluded that acceleration responses of the roof are higher and more effective in the X direction. In addition, the building rotation occurred at the base, while the hyperbolic rotation occurred at the roof. Finally, the previous statistical analysis results including ellipse errors, covariance, and linear fitting are sufficiently capable of investigating the performance of structures under earthquake loading, combined or separately.

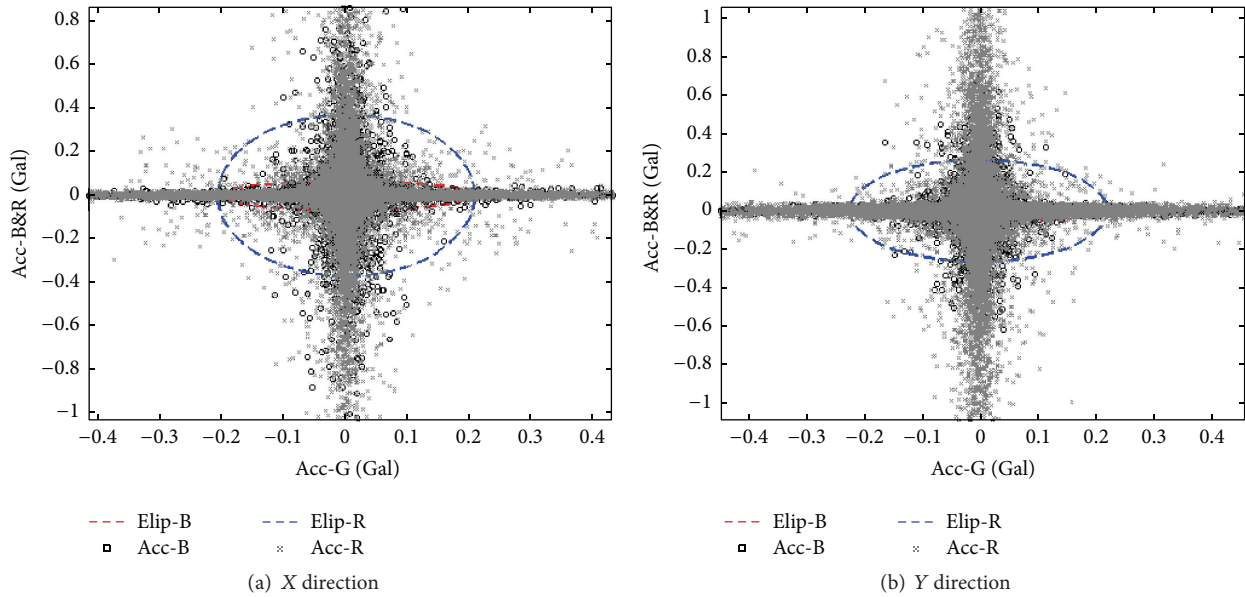


FIGURE 8: Ellipse error for the base and roof responses during the earthquake shaking.

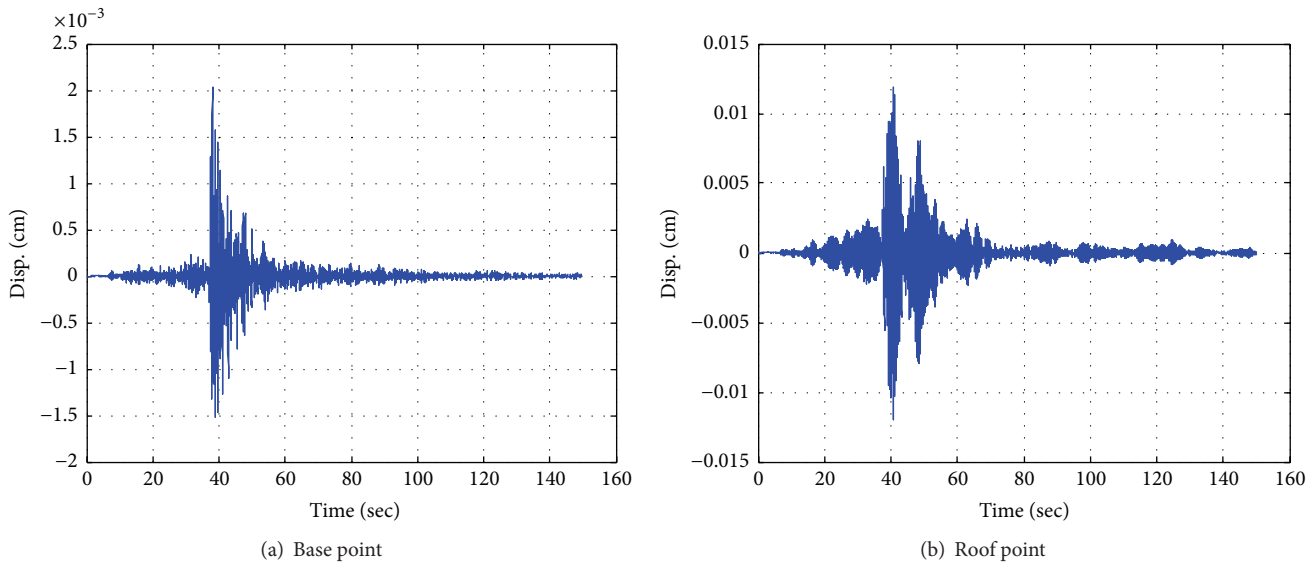


FIGURE 9: Dynamic displacement in X direction during the earthquake shaking.

**3.2. Displacement and Torsion Analysis.** Accelerometer sensors are used in monitoring static, semistatic, and dynamic structural performance [7]. The relations between acceleration, velocity, and displacement are governed by simple kinematics. The displacement is the integration of velocity, which in turn is the integration of acceleration. The high-pass filter is applied to the acceleration time histories, followed by double integration to extract the dynamic displacement. Sayed et al. [21] have applied 4th order Butterworth high-pass filter to efficiently extract the displacement from acceleration time history. Therefore, the 4th-order Butterworth high-pass filter is applied in this study with corner frequency 2 Hz, which exceeds the fundamental frequency of the building as will be described later.

The extracted dynamic (high frequency) displacements from the acceleration responses for the base and roof points in X direction are shown in Figure 9. The statistical values of the dynamic displacement are described in Table 4. From Figure 9 and Table 4, it can be seen that the maximum displacement occurred in roof in X direction; in addition, the standard deviation (STD) calculations illustrate that the displacements for the different recording points are within the acceptable range. In reality, all three-dimensional structures have both planned and elevation irregularity; thus, they are prepared for coupled translational and torsional responses. Moreover, there is only limited information at present on how to surpass the coupled horizontal and torsional vibration of structures, simultaneously.

TABLE 4: Dynamic displacement for the base and roof points (cm).

Parameters	Base point		Roof point	
	X	Y	X	Y
Max.	0.002	$7.65e-4$	0.012	0.006
Min.	-0.0015	$-8.43e-4$	-0.012	-0.006
Mean	$8.4e-10$	$5.74e-10$	$1.7e-10$	$1.32e-9$
STD	$4.3e-5$	$2.84e-5$	$4.22e-4$	$3.5e-4$

In fact, torsional response of structures subjected to dynamic earthquake or wind loading is applied for the real and experimental studies. Torsional motion is studied for the deck of long-span bridges such as Tacoma Narrows Bridges [19] and Zhujiang Huangpu Bridge [20]. Buildings are significantly vulnerable when subjected to torsional dynamic loads, especially those including asymmetric plan, which have been demonstrated from many destructive earthquake experiences. Therefore, it is important to consider this situation in the assessment of structures during earthquake shaking. However, the torsional displacement is measured to completely define the buildings movement under shaking loads. In this study, the torsional displacement of the building has been calculated with (1). Figure 10 demonstrates the diagram for the torsion displacement in X and Y directions for the building:

$$\theta = \arcsin\left(\frac{D}{L}\right) \times \frac{180}{\pi}, \quad (1)$$

where  $\theta$  is a torsion angle ( $\alpha$ ) for X and ( $\beta$ ) for Y directions as shown in Figure 10;  $D$  is the interstorey displacement for two symmetrical points in X or Y direction, as shown in Figure 10;  $D$  value equals  $(X_1 - X_2)$  for elevation and  $(Y_3 - Y_1)$  for plan.  $L$  is the distance between the two monitoring points, which is 33.8 m for X direction and 17.2 m for Y direction.

Figure 11 presents the torsional deformation of the roof point in the vertical plan (elevation direction or X direction) and horizontal plan (roof plan or Y direction) during the earthquake shaking. It can be seen that the significant torsional direction of building is the elevation direction with X direction. In addition, the maximum torsional deformation for the roof floor is 0.02 rad in X direction, while it is a negligible value (0.005 rad) in Y direction. The results prove that the vibration of the building in the X direction is higher and more dominant on the rotation of building in the longitudinal direction.

**3.3. Wavelet and Frequency Analysis.** Wavelet analysis is suitable for analyzing variations of power within signals [22]. The wavelet transform is not completely different from Fourier transform [22–24]. However, it is well-suited for analyzing signals with sharp discontinuities [23]. Windowed Fourier Transform or Short Time Fourier Transform (STFT) is more suitable for nonstationary signals. STFT basically maps a time series into a two-dimensional time series in both time and frequency domains. However, fixed frequency resolution for all frequencies is considered the main shortcoming of STFT [22–24]. The power spectrum method is considered a type

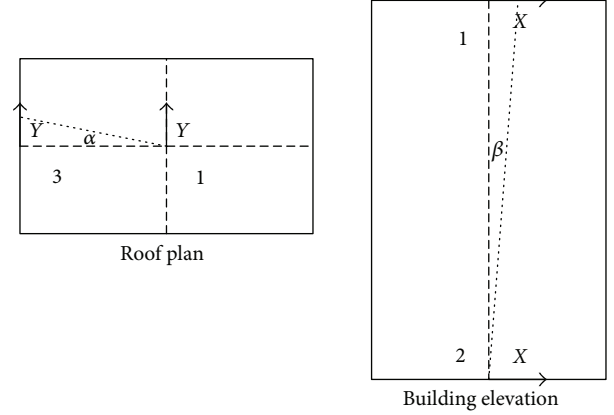


FIGURE 10: Torsional angle diagram view for the building.

of STFT for mapping frequencies changing in cyclist through time.

In the power spectrum, the signal is divided into segments, while the Fourier transform is calculated for these segments. The segments are multiplied by positive smooth bell-shape curves windows to avoid spectral leakage. The original signal can be reformed from the details only without any loss of information [23]. The reconstructed signal is illustrated as follows:

$$S_0(t) = \sum_{j=1}^n d_j(t), \quad (2)$$

where  $n$  is the total number of decomposition levels; and the detail components ( $d$ ) of the original signal ( $S$ ) can be expressed by the linear combination of the wavelet basis function (mother wavelet) as follows:

$$d_j(t) = \sum_{-\infty}^{\infty} C_{j,k} \psi_{j,k}, \quad (3)$$

where  $k$  represents an index of time scale,  $C_{j,k}$  are the corresponding wavelet coefficients, and  $\psi_{j,k}$  are the basis wavelet functions, which are expressed as

$$\psi_{j,k} = 2^{j/k} \psi(2^j t - k). \quad (4)$$

Finally, the original signal which has a time interval  $[0 \ t]$  can be expressed:

$$S_0(t) = \sum_{j=1}^n \sum_{k=0}^t C_{j,k} \psi_{j,k}. \quad (5)$$

There are many types of mother wavelets that can be defined. For discrete wavelet analysis, orthogonal wavelets (Daubechies and least-asymmetric wavelets) and B-spline biorthogonal wavelets have been commonly used [25]. In this study, the 10th-order Daubechies has been chosen. The choice to use Daubechies wavelets is motivated by their resemblance to the original signals [13]. Furthermore, the previous studies found that the Daubechies mother wavelet is

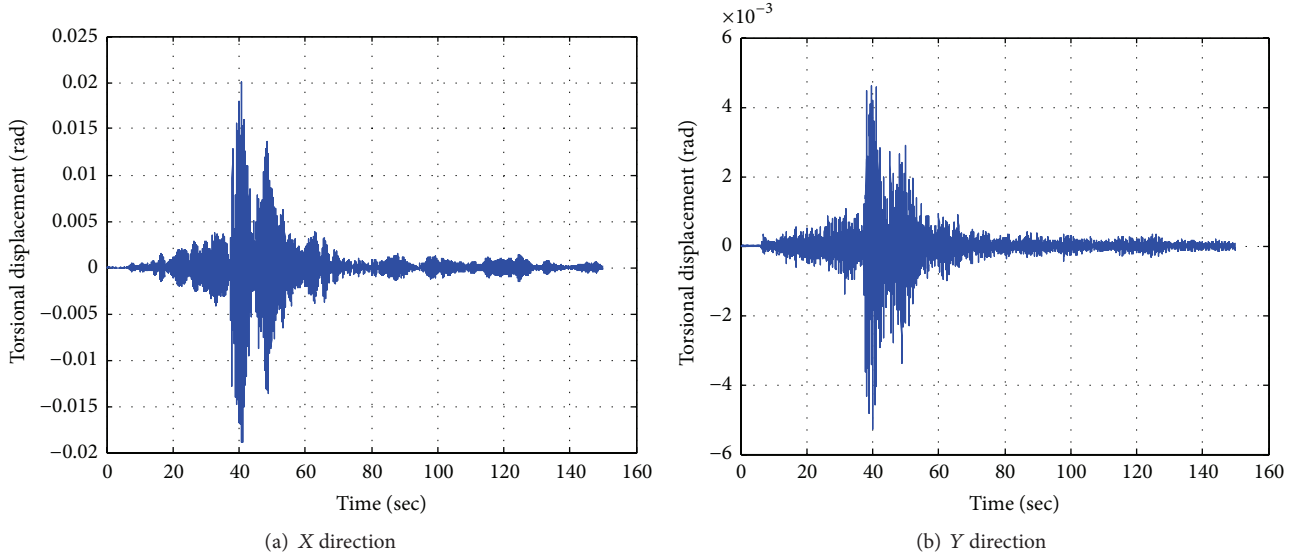


FIGURE 11: Torsional deformation of the building during shaking.

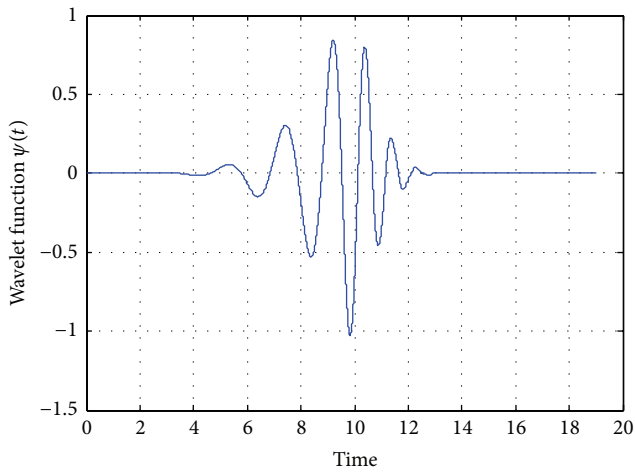


FIGURE 12: Daubechies basis function (db10).

suitable for the seismic performance analyses [12, 13]. Explicit form of the selected wavelet is shown in Figure 12, while the decomposition level calculations can be found in [25, 26]. In addition, the order of wavelet is used for its orthogonality and satisfactory resolution in both time and frequency domains [24, 27]. A high level of decomposition is selected in this study to present the full power performance of signal as shown in [26]. Therefore, the 9th decomposition level is selected to investigate the effectiveness of wavelet levels on the responses of the case study building due to earthquake shaking.

The recorded acceleration responses of the base and roof points in X direction are illustrated in Figure 13. From this Figure, it is shown that the peak recorded acceleration at the base point is 1.40 Gal, while it is 4.84 Gal for the roof point. In addition, the detail functions of the selected nine decomposition levels of the reconstructed details of the original recorded acceleration responses for the base and roof

points during the earthquake in X direction from level 1 to level 9 are presented from top to bottom in Figure 14.

The total energy of a discrete signal is the sum of the squares of its absolute values and, therefore, the total energy of the original signal can be expressed as follows [28]:

$$E = \Delta t \sum_{t=0}^t S_0^2(t). \quad (6)$$

In addition, the total energy can be represented in the form of details only at each decomposition level:

$$E = \sum_{j=1}^n \sum_{t=0}^t d_j^2(t). \quad (7)$$

The energy content of the decomposition levels of the acceleration response measurements at the different monitoring points during the earthquake shaking are demonstrated in Figure 15. From this Figure, it can be noticed that the energy distribution of the acceleration responses suffer slight changes between X and Y direction for the three monitoring points. Furthermore, Figure 15(a) illustrates that level 3, which represents the frequency content (12.5–25 Hz), contains 65% of the whole energy of the acceleration response of the ground point in both directions during the earthquake shaking. Moreover, levels 3 and 4, which represent (6.25–25 Hz), contain more than 95% of the energy. Furthermore, the energy distribution of the base point in Figure 15(b) demonstrates that level 4 (6.25–12.5 Hz) contains about 50% of the acceleration response energy.

Similarly, the energy distribution of the roof point in Figure 15(c) illustrates that level 5 (3.125–6.25 Hz) contains about 60% of the whole energy of the acceleration response measurements in both directions. Therefore, during the earthquake shaking, it can be concluded that the higher the monitoring point elevation, the lower the dominant

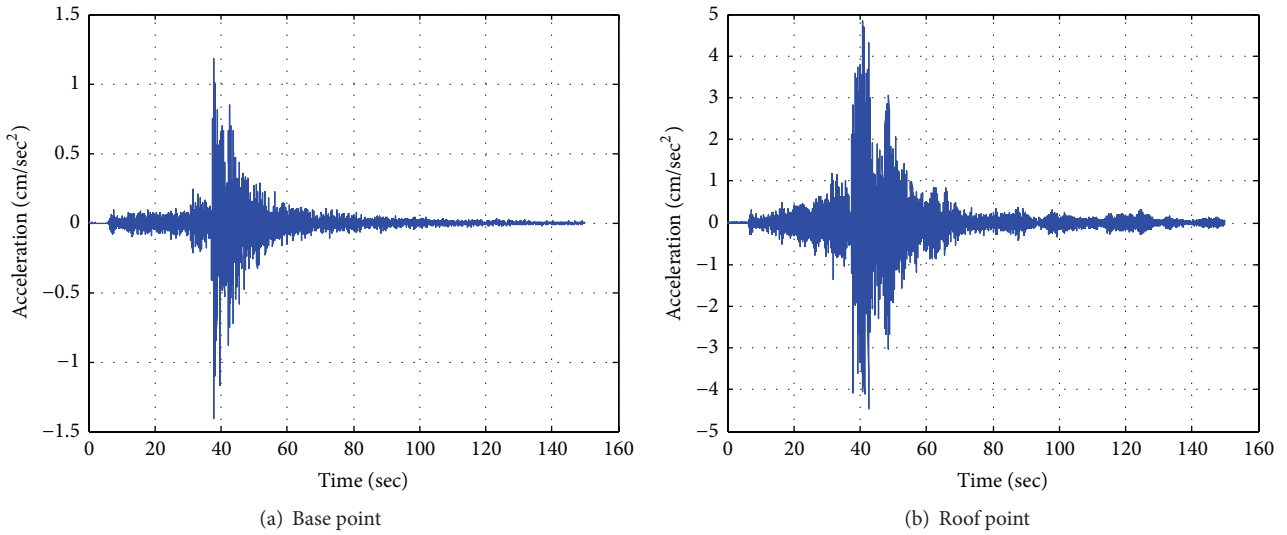


FIGURE 13: Acceleration response measurements in X direction during the earthquake shaking.

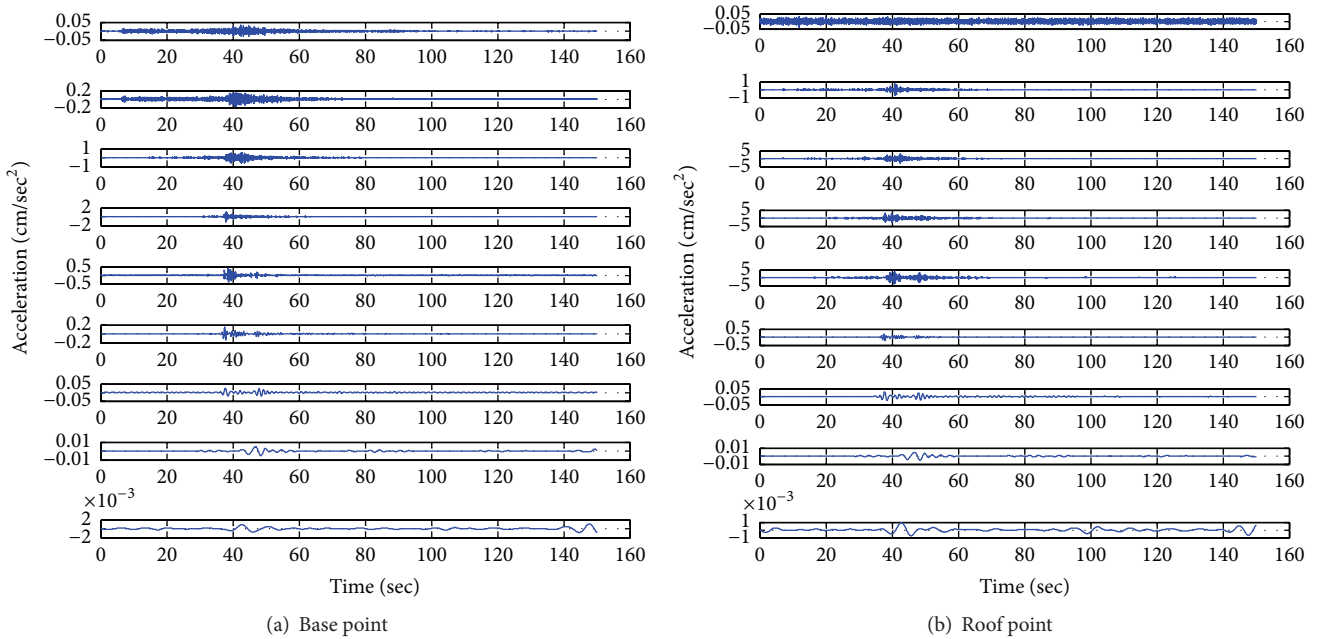


FIGURE 14: Decomposition levels of the reconstructed details for the base and roof points in X direction during earthquake shaking.

frequency range. Furthermore, the performance of various monitoring points can be compared based on the wavelet energy contents analysis.

Convenient methods such as FFT [25, 29] and wavelet spectrum [29, 30] are considered to estimate the frequency modes for the building. In wavelet spectrum analysis, scales numbers are first defined. These numbers outline the amount of stretch or compression that the wavelet achieves to map the variability of the signal in time domain at various wavelengths, where higher frequencies correspond to lower scales and vice versa. In this study, the wavelet analysis for more than 120 various scales is assumed. Consequently, the real or complex continuous components of wavelet coefficients are

computed. Finally, the converts scale to pseudo-frequencies, using the sampling period of the recorded acceleration and the computed wavelet coefficients.

Figure 16 illustrates the frequency models and wavelet spectrum for the acceleration measurements at the roof point. The fundamental frequency of the measurements is 2.54 Hz. In addition, the first and fourth mode frequencies are clearly visible at the measurements in X direction; while, modes one, four, and six are visible in Y direction.

The roof vibration is more noticeable compared to the base point vibration which is based on the power spectrum density comparison between the modes of the base and roof measurements. Moreover, the wavelet spectrum results

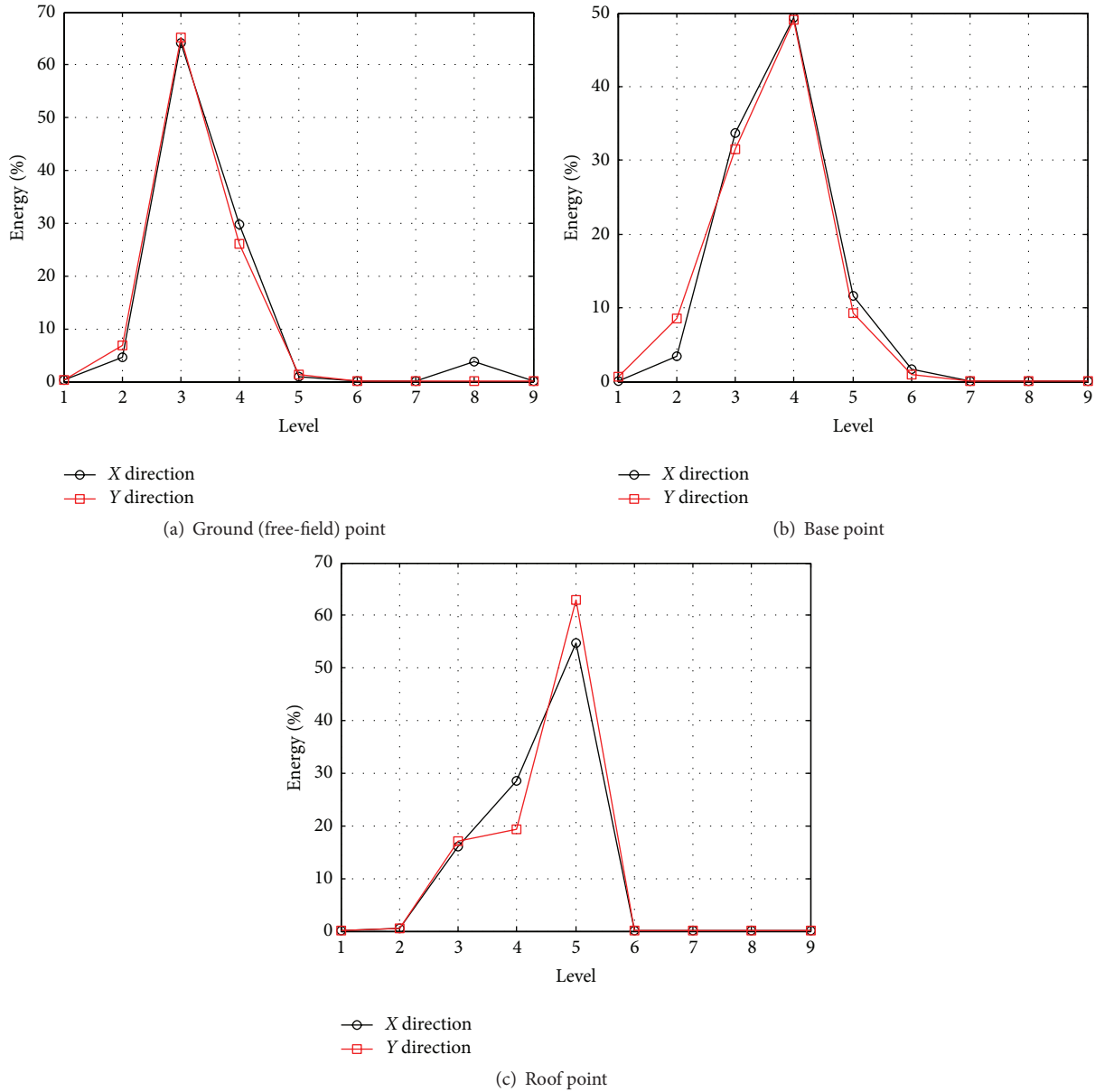


FIGURE 15: Energy distribution of the decomposition levels of the measurements points during the earthquake.

show that the dominant frequency of both base and roof points is the fundamental (first mode) frequency. This result implies the elasticity of the deformation responses of the building during the earthquake event. Finally, the wavelet and frequency methods results verify the energy contents of wavelet analysis to be an efficient tool in investigating the effect of earthquake events on the frequency content of structural responses and hence it is a powerful tool in structural performance assessment.

**4. Conclusions**

This study proposes a low cost acceleration SHM system to assess the structural performance of the administration building in Seoul National University of Education, South

Korea. The statistical (ellipse errors and covariance and linear fitting analyses) and wavelet analysis (power content and frequency analyses) methods are applied to investigate and assess the performance of the building during an earthquake shaking. The conclusions drawn from this study are as follows.

The statistical analysis results illustrated that the roof acceleration responses are higher than for the base point. Moreover, the roof torsional deformations are increased by 50% during the earthquake shaking in the two directions, while the base torsional deformations are small during the earthquake shaking. The rotation occurred for the base point, while the hyperbolic rotation occurred for the roof point in

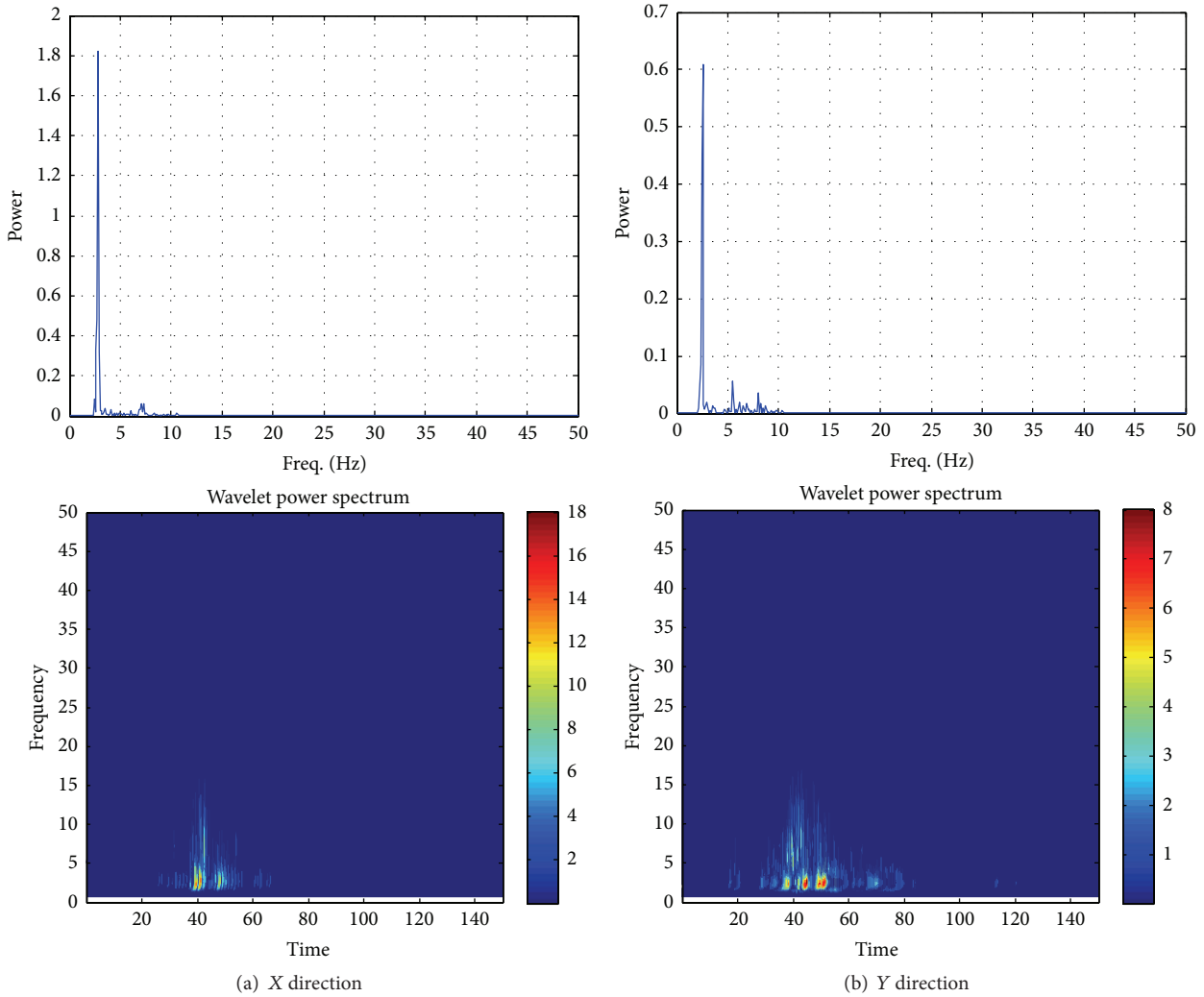


FIGURE 16: Frequency models and wavelet spectrum of roof point for X and Y direction.

the two directions. In addition, the roof eigenvalues and eigenvector are greater than for the base in the two directions, which assure the higher responses for the roof under the earthquake shaking. Finally, the statistical calculations and analysis illustrated that the displacements of the different recording points are within the acceptable range, which indicate building safety during the earthquake event.

The wavelet analysis results showed that the monitoring points frequency contents suffer slight changes between X and Y directions. In addition, it can be seen that the dominant frequency ranges are shown as 12.5–25 Hz, 6.25–25 Hz, and 3.125–6.25 Hz in both directions for ground, base, and roof points, respectively. Furthermore, it can be observed that the dominant frequency range (6.25–25 Hz) contains more than 95% of the energy. In addition, it can be concluded that the higher the monitoring point elevation, the lower the dominant frequency range that occurred during the earthquake shaking.

Therefore, during earthquake shaking, it is understood that higher the elevation reveals lower dominant frequency range.

The roof vibration is more noticeable compared to the base point vibration which is based on the power spectrum density comparison between the modes of the base and roof measurements. Moreover, the wavelet spectrum results show that the dominant frequency of both base and roof points is the fundamental (first mode) frequency. This result implies the elasticity of the deformation responses of the building during the earthquake event. Furthermore, the wavelet and frequency methods results verify the energy contents of wavelet analysis to be an efficient tool in investigating the effect of earthquake events on the frequency content of structural responses and hence it is a powerful tool in structural performance assessment.

Finally, the aforementioned results indicated that the proposed low cost acceleration monitoring system

which consists of three acceleration sensors, data-loggers, and a storage PC has proven its efficiency in investigating and assessing the structural performance of the building during the earthquake shaking.

### Conflict of Interests

The authors declare that there is no conflict of interests regarding the publication of this paper.

### Acknowledgment

This research was supported by a grant (14CTAP-C078944-01) from Technology Advancement Research Program funded by Ministry of Land, Infrastructure and Transport of Korean government.

### References

- [1] M. Gul and F. N. Catbas, "Statistical pattern recognition for Structural Health Monitoring using time series modeling: theory and experimental verifications," *Mechanical Systems and Signal Processing*, vol. 23, no. 7, pp. 2192–2204, 2009.
- [2] M. Çelebi, "Seismic monitoring of structures and new developments," in *Earthquakes and Health Monitoring of Civil Structures*, Springer Environmental Science and Engineering, chapter 2, pp. 37–84, Springer, Dordrecht, The Netherlands, 2013.
- [3] F. P. Kopsaftopoulos and S. D. Fassois, "Vibration based health monitoring for a lightweight truss structure: experimental assessment of several statistical time series methods," *Mechanical Systems and Signal Processing*, vol. 24, no. 7, pp. 1977–1997, 2010.
- [4] C. W. Follen, M. Sanayei, B. R. Brenner, and R. M. Vogel, "Statistical bridge signatures," *Journal of Bridge Engineering*, vol. 19, no. 7, Article ID 04014022, 2014.
- [5] S. D. Fassois and J. S. Sakellariou, "Time-series methods for fault detection and identification in vibrating structures," *Philosophical Transactions of the Royal Society A: Mathematical, Physical and Engineering Sciences*, vol. 365, no. 1851, pp. 411–448, 2007.
- [6] Y.-L. Ding, G.-X. Wang, P. Sun, L.-Y. Wu, and Q. Yue, "Long-term structural health monitoring system for a high-speed railway bridge structure," *The Scientific World Journal*, vol. 2015, Article ID 250562, 17 pages, 2015.
- [7] M. R. Kaloop, M. A. Sayed, D. Kim, and E. Kim, "Movement identification model of port container crane based on structural health monitoring system," *Structural Engineering and Mechanics*, vol. 50, no. 1, pp. 105–119, 2014.
- [8] M. R. Kaloop and J. W. Hu, "Stayed-cable bridge damage detection and localization based on accelerometer health monitoring measurements," *Shock and Vibration*, vol. 2015, Article ID 102680, 11 pages, 2015.
- [9] V.-N. Dinh, B. Basu, and R. B. J. Brinkgreve, "Wavelet-based evolutionary response of multispan structures including wave-passage and site-response effects," *Journal of Engineering Mechanics*, vol. 140, no. 8, Article ID 04014056, 2014.
- [10] V. Kumar, S. K. Gawre, and T. Kumar, "Power quality analysis using wavelet transform: a review," *International Journal of Innovative Research in Science, Engineering and Technology*, vol. 3, no. 3, pp. 130–136, 2014.
- [11] D.-A. Tibaduiza, M.-A. Torres-Arredondo, L. E. Mujica, J. Rodellar, and C.-P. Fritzen, "A study of two unsupervised data driven statistical methodologies for detecting and classifying damages in structural health monitoring," *Mechanical Systems and Signal Processing*, vol. 41, no. 1-2, pp. 467–484, 2013.
- [12] S. B. Ali and D. Kim, "Wavelet analysis of the seismic response of a base-isolated nuclear power plant structure considering soil-structure interaction," SMiRT-23 Division V, Paper 270, Manchester, UK, 2015.
- [13] F. Mollaioli and A. Bosi, "Wavelet analysis for the characterization of forward-directivity pulse-like ground motions on energy basis," *Meccanica*, vol. 47, no. 1, pp. 203–219, 2012.
- [14] V. Besharat, M. Davoodi, and M. K. Jafari, "Variations in ground surface responses under different seismic input motions due the presence of a tunnel," *Arabian Journal for Science and Engineering*, vol. 39, no. 10, pp. 6927–6941, 2014.
- [15] H. Li, T. Yi, M. Gu, and L. Huo, "Evaluation of earthquake-induced structural damages by wavelet transform," *Progress in Natural Science*, vol. 19, no. 4, pp. 461–470, 2009.
- [16] M. B. Nigro, S. N. Pakzad, and S. Dorvash, "Localized structural damage detection: a change point analysis," *Computer-Aided Civil and Infrastructure Engineering*, vol. 29, no. 6, pp. 416–432, 2014.
- [17] R. Yao and S. N. Pakzad, "Autoregressive statistical pattern recognition algorithms for damage detection in civil structures," *Mechanical Systems and Signal Processing*, vol. 31, pp. 355–368, 2012.
- [18] S. Arangio and F. Bontempi, "Structural health monitoring of a cable-stayed bridge with Bayesian neural networks," *Structure and Infrastructure Engineering*, vol. 11, no. 4, pp. 575–587, 2015.
- [19] H. S. Park, H. G. Sohn, I. S. Kim, and J. H. Park, "Application of GPS to monitoring of wind-induced responses of high-rise buildings," *Structural Design of Tall and Special Buildings*, vol. 17, no. 1, pp. 117–132, 2008.
- [20] M. R. Kaloop, "Bridge safety monitoring based-GPS technique: case study Zhujiang Huangpu Bridge," *Smart Structures and Systems*, vol. 9, no. 6, pp. 473–487, 2012.
- [21] M. A. Sayed, S. Go, S. G. Cho, and D. Kim, "Seismic responses of base-isolated nuclear power plant structures considering spatially varying ground motions," *Structural Engineering and Mechanics*, vol. 54, no. 1, pp. 169–188, 2015.
- [22] C. Torrence and G. P. Compo, "A practical guide to wavelet analysis," *Bulletin of the American Meteorological Society*, vol. 79, no. 1, pp. 61–78, 1998.
- [23] R. Z. Sarica and M. S. Rahman, "A wavelet analysis of ground motion characteristics," in *Proceedings of the U.S.-Taiwan Workshop on Soil Liquefaction, Taiwan*, 2003.
- [24] C. Sunde, *Wavelet and spectral analysis of some selected problems in reactor diagnostics [Licentiate Degree Thesis]*, Department of Reactor Physics, Chalmers University of Technology, Gothenburg, Sweden, 2004.
- [25] Y. Seo, S. Kim, O. Kisi, and V. P. Singh, "Daily water level forecasting using wavelet decomposition and artificial intelligence techniques," *Journal of Hydrology*, vol. 520, pp. 224–243, 2015.
- [26] Y.-F. Sang, D. Wang, and J.-C. Wu, "Entropy-based method of choosing the decomposition level in wavelet threshold denoising," *Entropy*, vol. 12, no. 6, pp. 1499–1513, 2010.
- [27] J. Iyama and H. Kuwamura, "Application of wavelets to analysis and simulation of earthquake motions," *Earthquake Engineering and Structural Dynamics*, vol. 28, no. 2-3, pp. 255–272, 1999.

- [28] J. S. Walker, *A Primer on Wavelets and Their Scientific Applications*, Chapman & Hall/CRC, New York, NY, USA, 2nd edition, 1999.
- [29] MathWorks, *MATLAB, The Language of Technical Computing*, MathWorks, Natick, Mass, USA, 2009.
- [30] M. H. Trauth, *MATLAB Recipes for Earth Sciences*, Springer, 3rd edition, 2010.